Refinement of nuclear models and experimental tools for neutrino cross sections at the GeV scale

Alejandro Nicolás Gaciño Olmedo

Supervised by:
Prof. Guillermo D. Megías (USE)
Dr. Stephen Dolan (CERN)
Dr. Laura Monteanu (CERN)
Prof. Andrea Longhin (UNIPD)
Dr. Fabio Pupilli (INFN-Padova)

Master Thesis
February 2024 - September 2024

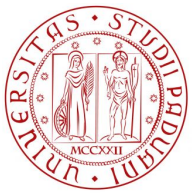

UNIVERSITÀ DEGLI STUDI DI PADOVA

Erasmus Mundus JMD on Nuclear Physics

Abstract

Current neutrino-nucleus experiments are fundamental in setting the groundwork for future long-baseline neutrino experiments, such as Hyper-Kamiokande and DUNE, which require a deeper understanding of GeV-scale neutrino interaction models and cross sections. Consequently, efforts are concentrated on achieving more cross-section measurements and reducing systematic uncertainties. To contribute to these objectives, this Master thesis comprises two main parts: a theoretical investigation on nuclear models in collaboration with the University of Seville and the CERN Experimental Physics Neutrino (EP-NU) group, and an experimental beam optimisation at the University of Padova.

The first part focuses on describing nuclear models to better reproduce final lepton states at T2K neutrino energies ($\sim$600 MeV). Beginning with a theoretical description of elastic neutrino-nucleon scattering cross-section, it establishes a mathematical foundation for incorporating nuclear effects in neutrino-nucleus interaction using different approaches: LFG (a Fermi gas-based description of the nucleus), SF (an empirical model) and SuSAv2 (an approach based on the superscaling phenomenon). Monte Carlo generators implementing these models, NEUT and GENIE, will be tested against cross-section measurements from the T2K near detector ND280, primarily to discern differences in Quasielastic events while assessing the agreement of the predictions.

The second part, conducted at the University of Padova, centers on optimising the ENUBET beam through GEANT4 simulations of the experimental setup. ENUBET aims to produce intense beams of muon and electron neutrinos or antineutrinos with reduced uncertainties compared to current neutrino beams like those employed in T2K or NOvA. The current work of the ENUBET collaboration is focused on increasing the flux intensity and reducing the beam related background in the tagger.

In summary, this Master thesis provides a comprehensive overview of two major neutrino research collaborations, T2K and ENUBET, contributing to different aspects within neutrino-nucleus experiments: evaluating the performance of Monte Carlo generators and enhancing experimental setups, respectively. The synergy between these efforts underscores the final steps that these collaborations are taking toward achieving precise measurements of neutrino oscillation parameters, potentially culminating in a complete and consistent framework for neutrino physics.

Contents

Part I

History of the neutrino and research status

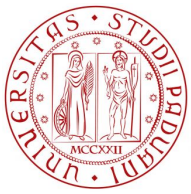

UNIVERSITÀ DEGLI STUDI DI PADOVA

1 History and current status of neutrino physics

Neutrino physics has significantly impacted modern physics, offering experimental evidence beyond the description provided by Standard Model. To understand the importance behind these particles and their interactions, this Thesis starts with a complete overview of the past, present and future in the theoretical framework and experimental status.

Firstly, this chapter delves into the historical journey of neutrino discovery, from Pauli's hypothetical postulation to the experimental evidence presented in the Reines and Cowan experiment of 1956. Subsequently, the current neutrino framework within the Standard Model is outlined, highlighting experimental observations that may contradict its postulates.

Neutrino oscillation emerged as the phenomena which contradicts the Standard Model description. Its importance relies on the experimental evidence that neutrino has a non-zero mass, therefore a brief history is presented starting from the solar neutrino problem to understand the relevance of the detection of atmospheric neutrino oscillations. It will be offered as well a theoretical overview of the current formalism employed to describe the neutrino oscillation.

Finally, the current and future landscape of long-baseline experiments is explored, with a particular focus on T2K, NOvA, T2HK, and DUNE. Understanding the significance and trajectory of neutrino physics research is pivotal in contextualizing this Master's Thesis, hence its structure and objectives are elucidated to underscore the importance of the results achieved.

1.1 Discovery of the neutrino

Neutrinos emerged as a concept to justify the disparities observed between theoretical predictions and experimental findings in nuclear beta decay during the first half of the 20th century. In 1956, neutrinos were finally detected in the Reines and Cowan experiment, marking a significant discovery in particle physics. This subsection aims to illustrate the history leading up to the detection of this elusive particle.

Theoretical postulation

In the early XXth century, the observation of nuclear decay processes, where nuclei transitioned into lighter ones while emitting particles, became a crucial point for understanding the nuclei inner mechanisms. Among these processes [1], beta decay signified as a relevant line of research, which was originally understood as the transformation of a parent nucleus X(A,Z) into a daughter nucleus Y(A,Z+1) accompanied by the emission of an electron:

$$X(A, Z) \rightarrow Y(A, Z + 1) + e^{-}. \tag{1.1}$$

This process suggested the possibility that a neutron could decay into a proton and an electron:

$$n \to p + e^{-}. \tag{1.2}$$

In a relativistic framework, assuming the initial nucleus X is at rest, the kinetic energy of the electron is well defined[1]. However, experimental observations[2] indicated that the observed electron kinetic energy spectrum exhibited a continuous distribution (see Figure 1), contrary to expectations for a two-body decay. In 1930, Wolfgang Pauli proposed the existence of another particle with neutral charge and much lighter mass, which was not being detected, to resolve this discrepancy. Later termed "neutrinos" by Enrico Fermi, these particles provided a theoretical explanation for the observed anomaly behavior in beta decay. Following the postulation of the new particle (and its respective antiparticle), beta decay is now understood as the decay of a proton or neutron mediated by the exchange of a charged boson W, emitting neutrinos in the process, as illustrated in Eqs. (1.3), (1.4) and in Figure 2.

$$\beta^{-} : X(A, Z) \to Y(A, Z+1) + e^{-} + \bar{\nu}, \tag{1.3}$$

$$\beta^{+} : X(A, Z) \to Y(A, Z-1) + e^{+} + \nu. \tag{1.4}$$

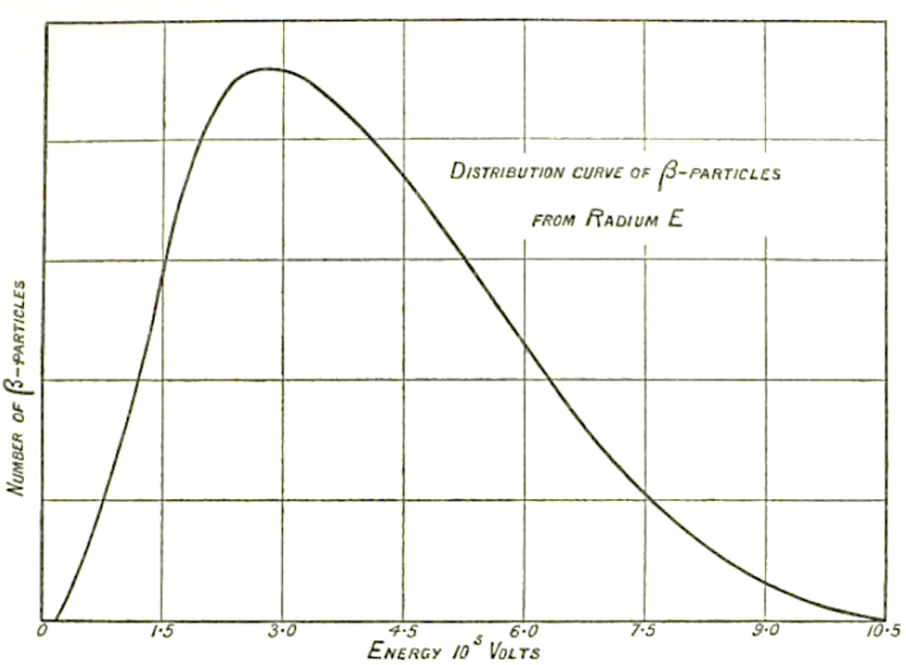

Figure 1: Electron kinetic energy spectrum obtained with an ionization chamber by Ellis and Wooster [4]. Note that "Radium E" is the name referred to ^{210}Bi.

[1] Under the text considerations, the kinetic energy of the electron is given by: $E_e = \left(\frac{M_X^2 - M_Y^2 + m_e^2}{2M_X}\right) c^2$.

[2] We include the study of ^{210}Bi decay in 1911 by Lisa Meitner [2], [3] and by Ellis and Wooster in 1927 [4].

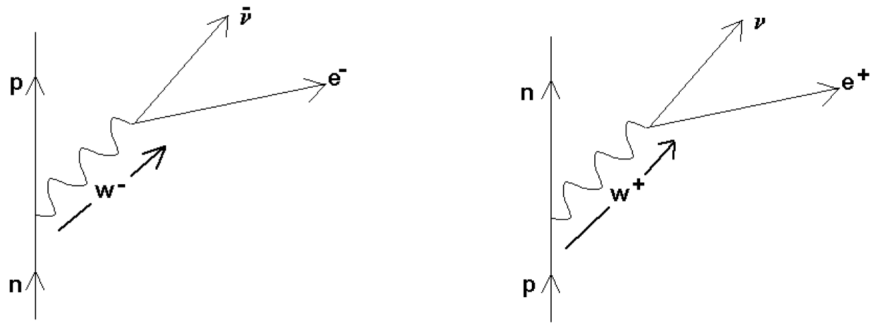

Figure 2: Beta decay Feynman diagrams at tree-level [5]. On the left, β^- decay and on the right, β^+ decay.

First experimental detection

After the postulation of the neutrino, in 1956, American physicists Clyde Cowan and Frederick Reines successfully detected this particle experimentally [6]. In their experimental setup, neutrons were emitted from the fission[3] of ^{235}U underwent β^- decay, producing antineutrinos which interact with protons in tanks filled with water solution of cadmium chloride, leading to the emission of positrons ($\bar{\nu} + p \rightarrow n + e^+$). Subsequently, the positrons annihilated with electrons, emitting photons that were absorbed by cadmium nuclei. Neutrons were captured by cadmium nuclei, also emitting photons as a result. The experimental signature of interest was the coincidental detection of these two photons. Figure 3 illustrates a schematic representation of the experimental setup. Since antineutrinos interact weakly with matter[4], they have an enormous mean free path (around 10^6 km under the experimental conditions). Hence, it was necessary to achieve a very intense antineutrino flux (on the order of 10^{13} particles cm^{-2}s^{-1}) to ensure sufficient statistical data.

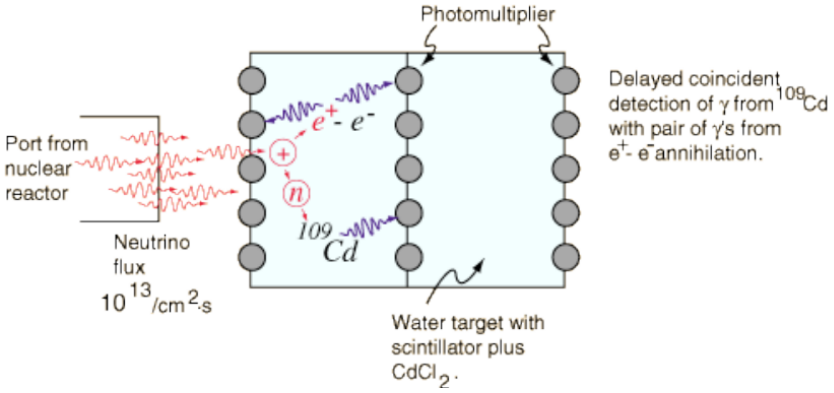

Figure 3: Schematic representation of the experimental setup conducted by C.L. Cowan and F. Reines in 1956 for the first experimental detection of the neutrino [7].

[3]In the experimental study, the fission channel is: $n + U(235, 92) \rightarrow F(235 - \mathrm{C}, 92) + \mathrm{C}n + \gamma$, with $^{235-\mathrm{C}}F$ the daughter nucleus and C an integer going from 1 to 8.

[4]The weak interaction cross-section is several orders of magnitude smaller than that of electromagnetism. For instance, antineutrinos with an energy of 1 GeV have an effective cross-section on the order of 10^{-39} cm^2 in the elastic scattering with a free nucleon.

The significance of this experiment was recognized with the Nobel Prize in Physics awarded to the American physicists in 1995. Subsequent research revealed that neutrinos exhibit different flavors, implying they are associated with a specific type of leptons following charged-current interactions. Muon neutrinos were first detected in 1962 at the Brookhaven National Laboratory [8], while tau neutrinos were experimentally confirmed in 2000 through the DONUT collaboration [9].

Currently, neutrino properties are described within the framework of the Standard Model, albeit with limitations. In the following subchapters, it is delved on their properties, eventually concluding why ongoing and future neutrino experiments are relevant for Physics beyond the Standard Model.

1.2 Neutrino properties in the Standard Model

Following its discovery, the neutrino assumed a crucial role in modern particle physics, finding its description within the theoretical framework of the Standard Model. In this section, we outline the fundamental properties of this particle, while also highlighting current lines of research aimed at scrutinizing aspects of its behavior that may deviate from theoretical predictions.

Lepton nature and flavours

Neutrinos are neutral charged leptons characterized by a spin of 1/2. The Standard Model recognises three distinct flavors of neutrinos: electron neutrinos (ν_e), muon neutrinos (ν_μ) and tauon neutrinos (ν_τ). Additionally, for each neutrino flavor, there exists a corresponding antineutrino, denoted by $\bar{\nu}_e$, $\bar{\nu}_\mu$ and $\bar{\nu}_\tau$ respectively. Hence, the Standard Model accounts for a total of six distinct types of active neutrinos.

However, in recent decades, the theoretical concept of a new type of neutrino known as "sterile neutrino" has been widely discussed. Theoretically, these are massive particles that would only interact via gravitational force. Experimentally, there are potential signatures suggesting that sterile neutrinos could explain the deficit of muon neutrinos observed in experiments from Kamiokande or IMB, as documented in [10], [11]. Further information regarding the current outlook on this hypothesis can be found in [12].

Lastly, the description provided by the Standard Model correspond to neutrinos being Dirac particles, meaning neutrinos and antineutrinos are distinct particles. However, an alternative theoretical framework proposes that neutrinos are their own antiparticles, referred to as Majorana particles. This possibility is currently under experimental investigation [13], with researchers attempting to detect neutrinoless double-beta decay ($0\nu\beta\beta$). This phenomenon involves a double-beta decay in which the two emitted antineutrinos interact with each other via pair annihilation, potentially providing evidence for neutrinos being Majorana particles. However, no conclusive confirmation has been obtained thus far.

Neutrino interaction with matter

Neutrinos interact solely through the weak nuclear force. This fundamental interaction is characterized by the following features:

- **Two distinct mechanisms**: charged-current interactions mediated by the exchange of charged $W^{\pm}$ bosons, and neutral-current interactions mediated by the exchange of neutral Z bosons. Only in the latter the neutrino maintains its nature, whilst in the first process there is a change from neutrino to its flavour associated charged lepton or viceversa.
- **Massiveness in particle mediator**, with rest-mass energies of approximately 80.377 ± 0.012 GeV and 91.1876 ± 0.0021 GeV, respectively for $W^{\pm}$ and Z [14]. Consequently, the range of the weak interaction is extremely short-distance, on the order of 10^{-17} meters. Furthermore, the cross section for weak interactions is 5-6 orders of magnitude lower than that of electromagnetic interactions.
- **Parity violation**, referring that the parity of the initial system can be different from the parity of the final system. However, in strong and electromagnetic interactions, parity is always conserved.

These properties lead to neutrino interactions being rare events in nature, presenting significant challenges for their experimental study. Nevertheless, theoretical analyses based on tree-level calculations (see [15] and [16]), such as those employing the Born approximation, can yield accurate predictions that match well with available experimental data.

Helicity

In the Standard Model, neutrinos exhibit a distinct helicity, whereby their spin is aligned opposite to their direction of movement, characterizing them as left-handed particles. Conversely, antineutrinos exhibit the opposite helicity, with both directions aligned. However, the rest of leptons exist in a superposition of both left- and right-handed states. This observation is justified in relativistic quantum mechanics, where only neutrinos and antineutrinos are considered massless leptons.

Nevertheless, with experimental evidence confirming that neutrinos indeed possess mass, theoretical frameworks have been developed to explain the possibility of the existence of right-handed neutrinos. A comprehensive examination of the current theoretical landscape and ongoing experiments aimed at detecting right-handed neutrinos can be found in [17].

Mass

In the Standard Model, neutrinos are conceived as massless particles. This is due to the consideration of only left-handed neutrinos since right-handed helicity in these particles have not been experimentally proven yet. However, the phenomena of neutrino oscillation proves that neutrinos indeed possess non-zero mass. Implicitly, the eigenstates of the

electroweak interaction (formally known as neutrino mass states and denoted as ν_1, ν_2 and ν_3) differ from the neutrino flavour states (ν_e, ν_μ and ν_τ). As detailed in subchapter 1.3, the relationship between these two sets of states is described by the Pontecorvo-Maki-Nakagawa-Sakata (PMNS) matrix, which depends on various parameters currently under research to refine their values.

As stated beforehand, neutrino oscillation needs non-zero masses for the mass eigenstates. However, the precise values of these masses are yet to be determined. It is only known accurately the information about the differences between these quantities squared, defined as Δm_{12}, Δm_{23} and Δm_{13} (formal definition is found in Eq. (1.12)). Consequently, two possible mass hierarchies are possible: the normal ordering and the inverted ordering (see Figure 4). Resolving this hierarchy question is crucial as it could lead to strengthen or eliminate numerous theoretical models explaining neutrino properties, as discussed in [18]. Recent studies strongly supports the normal ordering [19], [20].

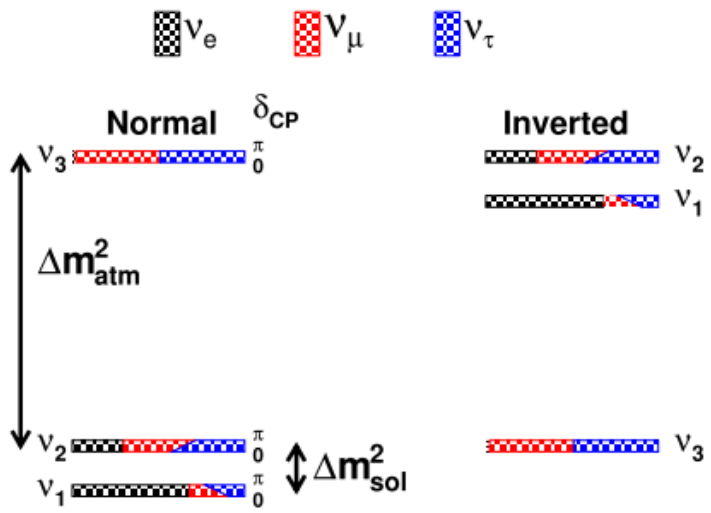

Figure 4: Scheme representation of the normal and inverted hierarchies. Flavor composition of the mass eigenstates as the function of the unknown CP phase δ_{CP} is shown. $\Delta m^2_{atm} \approx |\Delta m^2_{13}| \approx |\Delta m^2_{23}|$ and $\Delta m^2_{sol} \approx \Delta m^2_{12}$ stands conventionally for the atmospheric and the solar mass-squared splitting, respectively, as indicated in [18].

1.3 Neutrino oscillation

After describing the properties of neutrinos within the framework of the Standard Model, one of the most significant discoveries in neutrino physics is the phenomenon of neutrino oscillation. This not only confirms the existence of neutrino non-zero mass but also provides key-points details into their behavior. In this section, we delve into the historical background of neutrino oscillation, from its theoretical postulation as a solution to the solar neutrino problem to its experimental confirmation in the atmospheric neutrino experiment held in Super Kamiokande. Lastly, we examine the formalism from which this

phenomena is theoretically described.

First postulation: solar neutrino problem

In the nineteenth century, the study of solar reactions emerged as a relevant line of research aimed at gaining deeper understanding into stellar properties such as composition or evolution. Following the postulation of neutrinos in 1930 which provided a more comprehensive explanation of beta decay, Hans Bethe's article in 1939 [21] presented a theoretical framework for solar processes, describing what is now known as the proton-proton chain. This mechanism can be represented as:

$$4p \rightarrow {}^{4}\mathrm{He} + 2e^{+} + 2\nu_e. \tag{1.5}$$

In the 1960s, in an experimental attempt to validate the solar neutrino hypothesis, a neutrino detector was built in the Homestake mine in South Dakota [22]. The experimental setup aimed to capture neutrinos originating from the proton-proton chain reaction (Eq. (1.5)), which were considered the most feasible particle to detect due to their minimal interaction during their journey from the Sun to Earth.

Over a three-year period the detector gathered data, but the experimental results contradicted theoretical predictions. While theoretical models anticipated a neutrino capture rate of 7.2±1.2 Solar Neutrino Units[5] (SNU), the experimental data shown only 2.26±0.16 SNU. Criticism initially centered on the detector's inability to account for real-time solar flux fluctuations coming from stellar magnetohydrodynamics, despite the efforts to incorporate such uncertainties into the theoretical model predictions [23].

A strongly potential solution came with Bruno Pontecorvo's 1957 theoretical proposal [24], introducing the idea of neutrinos transitioning between different flavors during their propagation. This quantum phenomenon is currently known as neutrino oscillation. In the context of the Homestake experiment, electron neutrinos produced in the Sun could have transformed into other flavors as they propagated towards Earth, evading being detected due to the insufficiently sensitive detector, which only targeted electron neutrinos.

Experimental detection: atmospheric neutrinos

The first experimental evidence for neutrino oscillation was announced by the Super-Kamiokande collaboration in 1998. Over a period of 535 days, the Super-Kamiokande detector recorded data on atmospheric muon neutrinos at various intervals of zenith angles Θ. More information regarding the experimental setup and the analysis of the results can be found in [25].

Theoretical predictions indicated that in the absence of neutrino oscillation, Monte Carlo simulations would result in an isotropic Θ distribution of detected neutrinos due to their minimal interaction with matter. However, the experimental results revealed a deficit

[5]Solar Neutrino Unit or SNU is equivalent to 10^{-36} captures per second per target atom.

of muon neutrinos traveling through the Earth (∼12,800 km) compared to those coming directly from the atmosphere (∼15 km). When neutrino oscillation was incorporated into the simulations, the predicted distribution aligned closely with the experimental data. This discrepancy between the predictions with and without neutrino oscillation can be visualised in Figure 5.

The experimental evidence of neutrino oscillation phenomena lead to a Nobel Prize awarded to Takaaki Kajita in 2015. After the discovery, Super-Kamiokande continued recording data for about 5000 days in intervals of Θ cosine, thus enhancing the support towards neutrino oscillation, as discussed in the Nobel lecture [26].

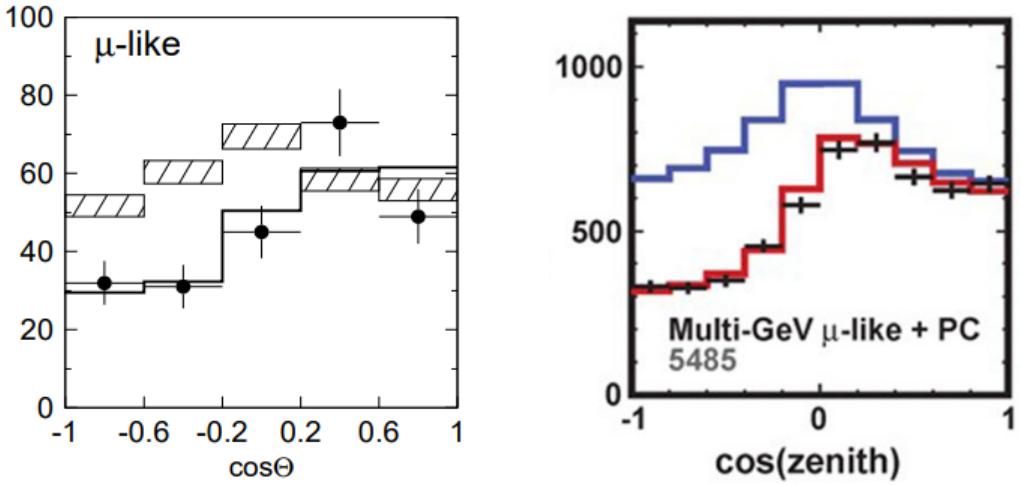

Figure 5: Muon neutrino events detected in Super-Kamiokande experiment versus the cosine of the zenith angle (Θ). Left: Data from 1998 [25]. Right: Data from 2015 [26]. Black dots represent experimental data, revealing a deficit of muon neutrinos at higher Θ. Hatched regions and blue line refer to predictions without neutrino oscillations, while black and red solid lines represent simulations accounting this phenomena. The agreement between simulations and data supports the existence of neutrino oscillation.

Neutrino oscillation formalism and current status

The significance of demonstrating neutrino oscillation lies in its indication of non-zero neutrino mass, contradicting the Standard Model's description. To understand this implication, we will delve into the formalism from relativistic quantum mechanics used to model oscillations between two states.

We start by postulating that the stationary states of neutrinos (denoted as ν_1 and ν_2, being the eigenstates of the electroweak interaction Hamiltonian) are linked to the flavor states ν_μ and ν_e through linear orthogonal combinations. As shown in Eq. (1.6), this relationship depends on a mixing angle factor θ. Furthermore, assuming an electron neutrino at time $t = 0$, originating, for instance, from a β^+ decay, we can apply the time-dependent Schrödinger Equation to determine the time evolution of the eigenstates

ν_1 and ν_2, as illustrated in Eq. (1.8).

$$|\nu_1\rangle = \cos\theta\,|\nu_\mu\rangle - \sin\theta\,|\nu_e\rangle\,; \quad |\nu_2\rangle = \sin\theta\,|\nu_\mu\rangle + \cos\theta\,|\nu_e\rangle\,, \tag{1.6}$$

$$\left\{ \begin{array}{l} |\nu_e(0)\rangle = |\nu_e\rangle\,, \\ |\nu_\mu(0)\rangle = |0\rangle\,, \end{array} \right\} \longrightarrow \left\{ \begin{array}{l} |\nu_1(0)\rangle = -\sin\theta\,|\nu_e\rangle\,, \\ |\nu_2(0)\rangle = \cos\theta\,|\nu_\mu\rangle\,, \end{array} \right\} \tag{1.7}$$

$$|\nu_1(t)\rangle = -\sin\theta e^{-\frac{iE_1 t}{\hbar}}\,|\nu_e\rangle\,; \quad |\nu_2(t)\rangle = \cos\theta e^{-\frac{iE_2 t}{\hbar}}\,|\nu_\mu\rangle\,. \tag{1.8}$$

To compute the probability of flavor change after a time t, we must express the state $|\nu_\mu(t)\rangle$ in terms of $|\nu_1(t)\rangle$ and $|\nu_2(t)\rangle$. This allows the calculation of the invariant amplitude:

$$P_{\nu_e\to\nu_\mu}(t) = |\,\langle\nu_\mu(t)|\nu_\mu(t)\rangle\,|^2 = \left[\sin(2\theta)\sin\left(\frac{E_2 - E_1}{2\hbar}t\right)\right]^2. \tag{1.9}$$

We now remark some considerations:

- We can establish a relationship between the parameter time t and the distance traveled L by assuming a velocity for neutrinos close to the speed of light[6]: $t \approx L/c$.
- Assuming neutrinos are massive particles, we can relate the energies of the eigenstates E with their respective masses m using energy-momentum conservation. Since $mc \ll p$, we can simplify the expression using a first-order Taylor expansion: $\sqrt{1+x} \approx 1 + x/2$. This yields:

$$E^2 = c^2p^2 + m^2c^4 \longrightarrow E = cp\sqrt{1 + \frac{m^2c^2}{p^2}} \approx cp\left(1 + \frac{m^2c^2}{2p^2}\right). \tag{1.10}$$

- The energy difference between eigenstates results in the following expression after applying the aforementioned approximation. To simplify further, we introduce the squared-mass difference parameter Δm^2, defined in Eq. (1.12):

$$E_2 - E_1 = \frac{(m_2^2 - m_1^2)c^3}{2p}, \tag{1.11}$$

$$\Delta m^2 \equiv m_2^2 - m_1^2. \tag{1.12}$$

These considerations lead to the final expression of the probability of flavor change, which depends on the distance traveled L:

$$P_{\nu_e\to\nu_\mu}(L) = \sin^2(2\theta)\sin^2\left(\frac{\Delta m^2 c^4 L}{4E\hbar c}\right). \tag{1.13}$$

It becomes apparent that a non-zero probability of flavor change requires a non-zero difference between the masses of the eigenstates m_1 and m_2. Modeling the flavor is crucial due to the associated charged lepton that emerges after a charged-current interaction,

[6]Technically, if neutrinos were to be massless particles, their velocity would be c. However, since we know that their are massive, but extremely light, this approximation is totally valid.

enabling the detection of these particles. Thus, the demonstration of neutrino oscillation phenomena confirms neutrino non-zero mass.

However, extending this to the real scenario of the three-flavor case involves resolving a more complex problem. Currently, the correspondence between the eigenstates ν_1, ν_2, and ν_3, and the flavor states ν_e, ν_μ, and ν_τ is fully detailed in the Pontecorvo-Maki-Nakagawa-Sakata (PMNS) matrix, as shown in Eq. (1.14). The components $U_{\alpha\beta}$ indicate the mixing relation between eigenstate-flavor, encompassing the mixing angles (θ_{12}, θ_{23}, and θ_{13}, the squared-mass differences Δm_{12}, Δm_{23} and Δm_{13} and the CP-violation term[7]. A comprehensive explanation of the parameters involved, as well as the origin and implications of this matrix, can be found in [27].

$$\begin{pmatrix} \nu_e \\ \nu_\mu \\ \nu_\tau \end{pmatrix} = \begin{pmatrix} U_{e1} & U_{e2} & U_{e3} \\ U_{\mu 1} & U_{\mu 2} & U_{\mu 3} \\ U_{\tau 1} & U_{\tau 2} & U_{\tau 3} \end{pmatrix} \begin{pmatrix} \nu_e \\ \nu_\mu \\ \nu_\tau \end{pmatrix}. \tag{1.14}$$

1.4 Long-baseline experiments

Long-baseline neutrino experiments aim to determine accurately the mixing angles and CP-violation terms, while providing insights into solving the mass hierarchy problem. These experiments involve detecting neutrinos after they travel macroscopic distances, exploring neutrino interactions and transformations over long distances. These experiments employ two detectors as illustrated in Figure 6: a near detector, positioned close to the neutrino source to measure the initial neutrino flux, and a far detector, situated at the end of the baseline to capture neutrinos after their journey. This setup allows for precise measurements of neutrino oscillations and interactions over extended distances.

Figure 6: Scheme of neutrino baseline detection in long-baseline neutrino experiments. Figure taken from [28].

The history of long-baseline experiments began with K2K (KEK to Kamiokande), which confirmed neutrino oscillation phenomena using the water Cherenkov Super-Kamiokande detector. Concurrently, the MINOS experiment at Fermilab (United States) focused on measuring mixing angles and mass splitting by observing the disappearance of muon

[7]CP violation in the context of neutrino oscillation is yet hypothesised and pending to be tested in the upcoming neutrino experiments. This effect implies that oscillation probabilities are different for neutrinos and antineutrinos. Implicit in the term δ_{CP}, this arises formally from the complex formalism of rotational matrices.

neutrinos. These experiments constitute the predominant representatives of the first generation of accelerator-based experiments [29], [30].

Currently, this field has entered the second generation, represented mainly by T2K and NOνA. As we will see, the status of art is such that neutrino physics are highly developed theoretically with few experimental data to check the hypothesis. Therefore, it is of high interest to perform experimental studies in order to proceed further with a consistent theoretical description of neutrinos.

In this section, we will delve into explaining the second and third generations of baseline experiments to provide a deep understanding of the context within which this thesis is situated.

1.4.1 Current generation

This generation is primarly represented by T2K and NOνA, succeeding KEK and MINOS and leading to the future Hyper-K and DUNE experiments, respectively [31]. The interest behind these two experiments comes from their supplementation: both can provide crucial insights towards CP violation, normal or inverted mass hierarchy and complementary results towards the parameters enclosed in the 3x3 unitary mixing framework.

T2K

The T2K experiment is specifically designed to investigate neutrino mixing and provide insights into the neutrino mass scale. Its primary objectives include in a muon neutrino/antineutrino beam the precise measurement of Δm^2_{23} and θ_{23} through the observation of muon neutrino disappearance, as well as the determination of θ_{13} via $\nu_\mu \rightarrow \nu_e$ appearance. T2K comprises a muon neutrino beamline, a near detector complex located at 280 m (referred to as ND280), and a far detector (Super-Kamiokande) positioned 295 km away. Data collection for this experiment commenced in 2010 and is expected to continue until 2027.

The neutrino beam is generated at a proton synchrotron in J-PARC and directed at a 2.5^o angle to ensure a peak energy around 0.6 GeV, thereby maximizing[8] the neutrino oscillation effects at the 295 km final distance.

The near detector complex, situated in Tokai, incorporates both on-axis and off-axis detectors. The on-axis detectors (INGRID) are close to the beam production point, measuring the neutrino beam direction and profile, while the off-axis detector (ND280) assess the muon neutrino flux and energy spectrum. Current efforts are focused on upgrading the ND280, which will involve enhancing the reconstruction of the final state by improving the angular acceptance and resolution of incoming charged particles through the implementation of new high-angle TPCs [32]. Additionally, there are plans to extend the

[8]Further details are provided in Chapter 4.1.

reconstruction capabilities to lower energies of the hadronic component in the final state using hydrocarbon materials [33]. Further simulation details regarding the T2K near detector upgrade can be found in [34].

The far detector is situated in the Kamioka Mining facility, shielded by a 1 km-thick layer of rock to mitigate spurious events caused by cosmic rays. It comprises a water Cherenkov detector housed within a stainless steel tank with a capacity of 50,000 tons. Equipped with 13,000 photomultiplier tubes, the detector reconstructs the direction, energy, and properties of neutrinos by collecting Cherenkov radiation emitted during their interactions with the pure water.

NOνA

The NOνA (NuMI Off-axis Neutrino Appearance) experiment, succeeding MINOS, plays a significant role in the development of DUNE. In contrast to T2K, NOνA features a longer separation distance between its near (located at Fermilab) and far detectors (located in Ash River, Minnesota), spanning 810 km, with a peak flux energy of 1.8 GeV. Data collection for NOνA commenced in 2014 and is anticipated to continue until 2026.

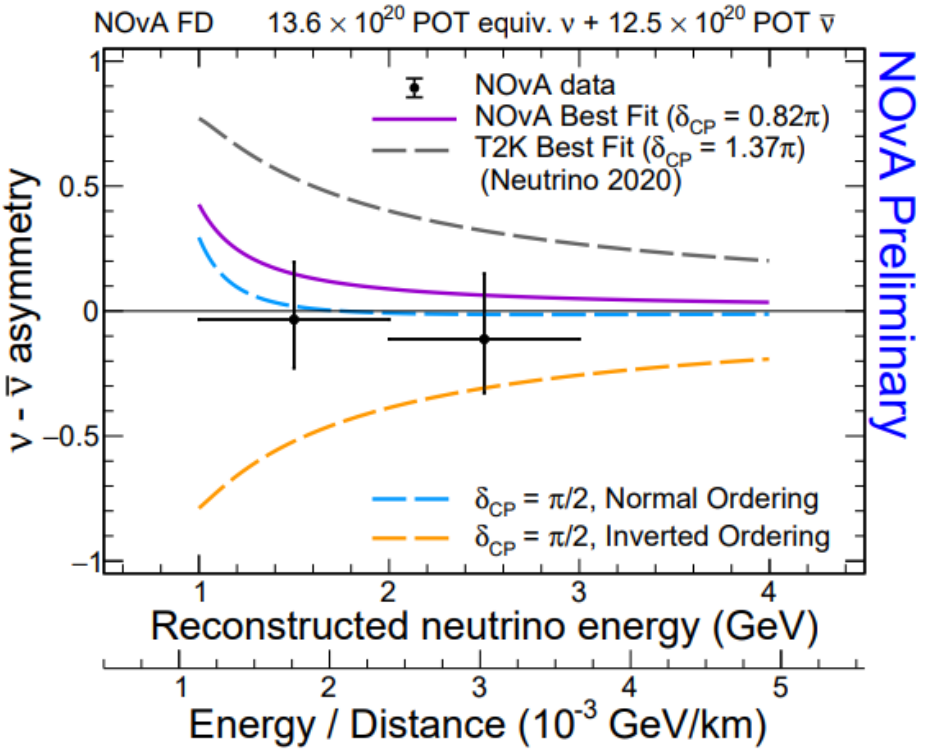

Figure 7: Neutrino-antineutrino event asymmetry as a function of resonstructed neutrino energy with the NOνA best fit shown in purple. T2K best fit results is also shown (grey dashed) for comparison. Theoretical $\delta_{CP} = \pi/2$ in normal and inverted ordering is displayed in blue and yellow dashed lines respectively. Figure extracted from [35].

The NuMI facility (Neutrinos at the Main Injector) serves as the muon neutrino source,

where 120 GeV protons collide with a graphite target. The resulting (anti)neutrinos travel 14 mrad off the beam axis towards the far detector, where measurements are made of the appearance rate of muon and electron (anti)neutrinos. This setup facilitates not only measurements related to the mixing parameters in the 3x3 representation but also provides valuable insights into the value of δ_{CP}, as illustrated in Figure 7.

1.4.2 Next generation

Following in the footsteps of T2K and NOνA, the next-generation experiments, T2HK (T2 Hyper-Kamiokande) and DUNE (Deep Underground Neutrino Experiment), are expected to offer deeper insights into CP violation, mixing angles, and eigenstate mass differences. With enhanced designs compared to their predecessors, these experiments will provide better statistical precision and incorporate matter effects, thereby advancing efforts to resolve the mass hierarchy problem [36].

T2HK

Approved in 2020 and scheduled to commence operations in 2027, T2HK features a baseline of 295 km, similar to T2K, thereby limiting its sensitivity to matter effects and the mass hierarchy. The peak flux neutrino energy will remain at 0.6 GeV.

The near detector, located at J-PARC, will undergo upgrades similar to the ND280 enhancements, while the far detector at the Tochibora mine in Kamioka boasts a volume 8.4 times larger than its predecessor, ensuring improved resolution of results. Additionally, the beam power will be boosted from 500 kW to 1.3 MW to significantly enhance statistical precision.

T2HK is expected to make substantial strides in improving systematics and excluding values for δ_{CP}, as illustrated in Figure 8. Assuming the normal ordering, the experiment aims to exclude up to 70% of potential δ_{CP} values at 5σ confidence level over its 10-year operational period.

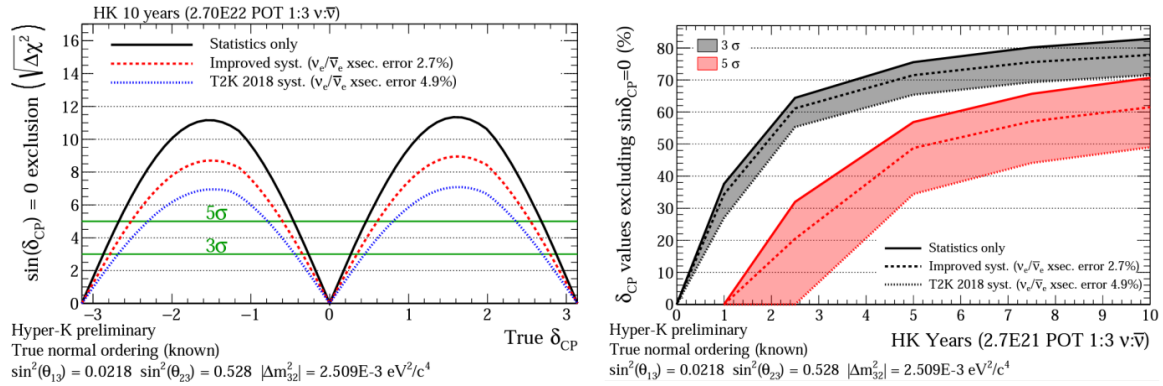

Figure 8: Assuming the normal ordering to be true, in the left it is displayed the uncertainty in the exclusion of the possible values of δ_{CP}. In the right, the evolution of the excluded values in % throughout time operation of T2HK. Figure extracted from [37].

Furthermore, T2HK is aimed at the detection of superNOνA neutrinos, aiding in the distinction between various burst mechanisms, and to probe theoretical proton decay due to its enhanced sensitivity, thereby establishing itself as a multi-purpose experiment.

DUNE

The Deep Underground Neutrino Experiment (DUNE) will be performed in the USA, with a baseline of 1300 km and a peak neutrino energy of 2.5 GeV, making it sensitive to matter effects. The experiment comprises the neutrino production facility (LBNF), a near detector at Fermilab, and a far detector at the Sanford Underground Research Facility in South Dakota, utilising liquid argon technology, the detectors are designed to cover a wide spectrum of neutrino energies.

The beam is planned to be upgraded to 2.4 MW, colliding protons with energies ranging from 60 to 120 GeV on a graphite target, producing muon (anti)neutrinos with varying energies.

The near detector, located 574 m from the source, characterises neutrino flux and flavor composition. It consists of three primary detectors: ND-LAr (identifying $\nu-$Ar interactions to improve systematics), ND-GAr (detecting muon tracks from ND-LAr), and SAND (determining neutrino spectrum and on-axis flux). The far detector comprises four modules, with the first two employing horizontal drift TPC and the remaining two using vertical drift TPC. Neutrinos interact with liquid argon in these modules, and resulting photons are collected by the Photon Detection System [38].

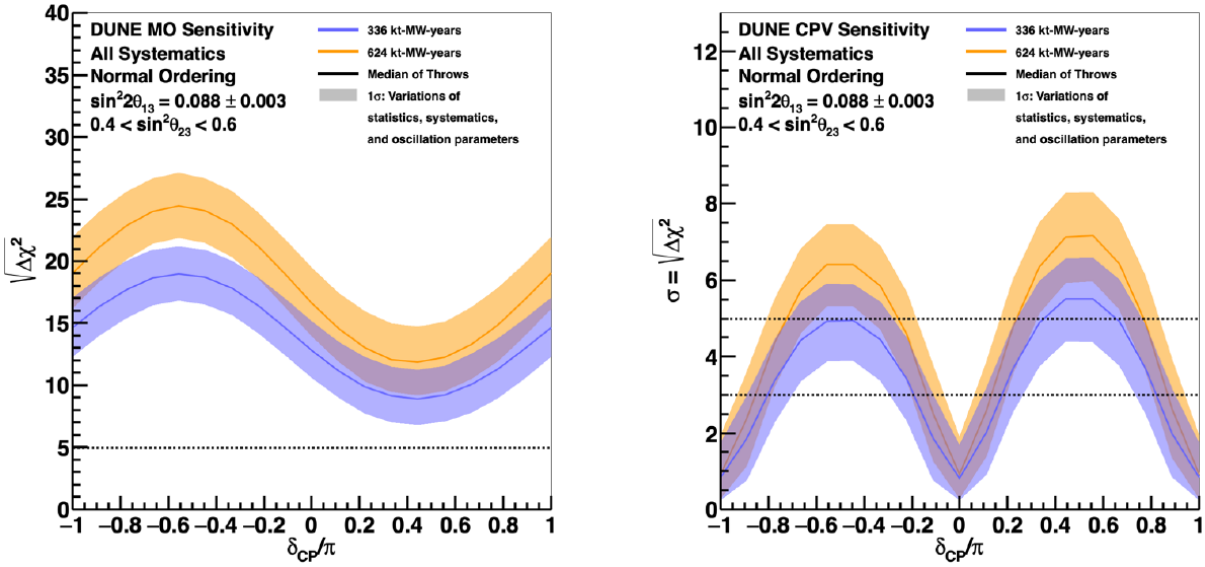

Figure 9: DUNE sensitivity, assuming normal mass ordering, to neutrino mass ordering (left) and CP violation (right) as function of δ_{CP} for the given exposures of 336 kt-MW-years and 624 kt-MW-years, corresponding respectively to an estimated operation time of 7-8 years and 11 years. Figure extracted from [39].

DUNE is still in the early stages of development, with operations expected to commence in 2031 and decisive results for CP violation can be achieved by 2039, as displayed in Figure 9. However, preliminary projects aimed at its development, such as ProtoDUNE at CERN, are currently underway.

1.5 Thesis structure

Current research in neutrino physics focuses on experimental studies to gather sufficient data for checking several theoretical descriptions of neutrino interactions. This Master Thesis aims to contribute to the future predominant experiments through a two-fold task.

Firstly, an extensive analysis of T2K data for charged-current neutrino-nucleus interactions with no pions in the final state (CC0π) is intended. Part II undertakes a comprehensive theoretical description of different nuclear responses widely used in current studies: Local Fermi Gas (LFG), Spectral Function (SF) and the recent SuSAv2 (based on the SuperScaling approach). This part begins with an introduction to the formalism of neutrino elastic interaction with a free nucleon and continues with the modeling of nuclear effects, comparing these responses with past experimental studies to validate their alignment with theoretical predictions.

Using the experimental T2K 2020 data provided at CERN, Part III conducts a thorough analysis on the Monte Carlo generator NEUT and GENIE performances based on the described nuclear responses. It is crucial to examine the consistency of the predicted results with the data, leading to further refinements in experimental tools and in the aforementioned theoretical models.

Secondly, this Thesis aims in Part IV to refine the beam in the ENUBET experiment directed from the University of Padova. By employing the Geant4 toolkit simulator, the current setup is analysed deeply to optimise the geometry for further purification of kaon production in the beam, ultimately improving the performance in neutrino production. ENUBET holds significant promise in contributing to the neutrino source for the new generation of long-baseline experiments, especially for T2HK and DUNE.

Lastly, Part V presents a summary and the main conclusions of this Master Thesis, providing a comprehensive overview of the work performed and significant results for future long-baseline experiments.

Part II

Theoretical description of nuclear response models in neutrino-nucleus scattering

2 Neutrino-nucleon elastic scattering

As a preliminary analysis, this chapter examines the basics of neutrino-nucleon scattering to describe the formalism of the electroweak elastic interaction at tree level for both neutrino and antineutrino processes.

However, this description does not fully explain the results obtained in experiments involving neutrino and light nuclei interactions, as no nuclear model is introduced. Thus, this preliminary analysis sets the groundwork for including nuclear effects in Chapter 3.

The importance of both chapters lies in gaining a better understanding of some relevant magnitudes to measure in neutrino-nucleus experiments (inclusive cross section, lepton momentum, and neutrino energy) and in conducting a comprehensive analysis of the experimental T2K data in Part III.

2.1 Inclusive cross-section formalism

This section methodically dissects the modeling of neutrino-nucleon interactions, covering the analysis of kinematics, S-matrix calculations, and cross-section expressions. In subsection 2.1.1, a detailed examination of kinematic aspects is conducted, adopting a laboratory frame and elucidating the approximations applied to model the neutrino-nucleon kinematics.

Transitioning to subsection 2.1.2, the focus sharpens on the formalism of S-matrix S_{fi} calculations, specifically within the context of first-order approximations for elastic charged-current scattering in neutrino-nucleon interactions. The formal definitions of S_{fi} and the interaction Hamiltonian H_W are grounded in Relativistic Quantum Mechanics, being mandatory the utilization of Dirac Algebra. Appendix A provides a comprehensive explanation of these concepts, along with detailed mathematical steps used throughout the calculus.

Subsequently, in subsection 2.1.3, attention shifts to cross-section expressions. The derivation of differential cross sections provides valuable insights into their dependencies on crucial kinematic parameters, namely, lepton energy (ε_l) and the cosine of the scattering angle ($\cos\theta$). These insights are anticipated to play a pivotal role in the subsequent analyses presented in further sections.

2.1.1 Analysis of the kinematics

To analyse the kinematics of neutrino-nucleon charged current elastic scattering, we adopt a laboratory frame, as depicted in Figure 10a. Here, the initial nucleon is considered at rest, and the transferred momentum $\vec{q}$ aligns with the z-axis, while both the initial and final nucleons reside within the XZ plane. The relevant kinematic parameters are detailed

below[9], and the corresponding Feynman diagram at first order is presented in Figure 10b:

- Neutrino ν_l: $K_\nu^\alpha = (\varepsilon_\nu, \vec{k}_\nu)$.
- Initial nucleon N_i: $P_i^\alpha = (M, \vec{0})$.
- Lepton l^-: $K_l^\alpha = (\varepsilon_l, \vec{k}_l)$.
- Final nucleon N_f: $P_f^\alpha = (E_f, \vec{P})$.
- Exchanged boson W^-: $Q^\alpha = (\omega, \vec{q})$.

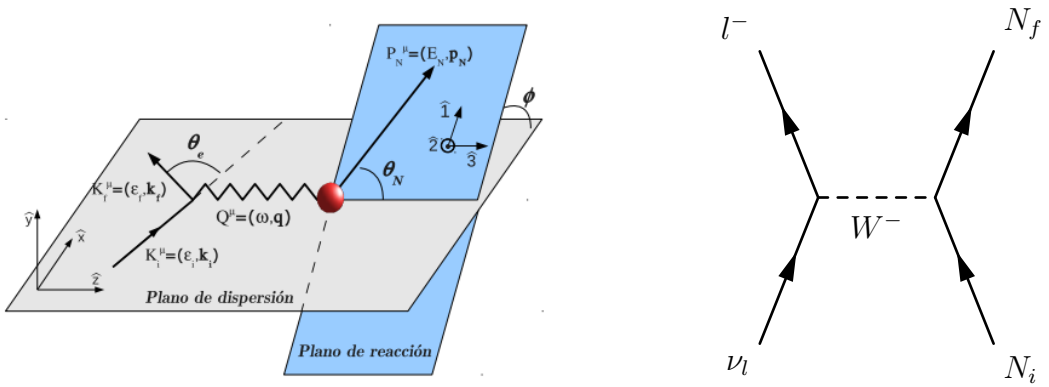

(a) (b)

Figure 10: a) Schematic representation of the laboratory frame employed for elastic neutrino-nucleon charged-current W^- scattering. In this thesis, it is assumed that the initial nucleon is at rest. b) Corresponding Feynman diagram at the first-order approximation.

Now, we proceed with an examination of the conservation of energy-momentum at the vertex. Given the range of energies under consideration, an ultrarelativistic approximation ($E \approx |\vec{k}|$) is effectively employed for neutrinos[10]. Consequently, the leptonic and hadronic vertices analysis conservation yield the following results:

Leptonic vertex

- Energy conservation: $\varepsilon_\nu - \varepsilon_l = \omega$.
- Momentum conservation: $\vec{k}_\nu - \vec{k}_l = \vec{q} \longrightarrow q^2 = \varepsilon_\nu^2 + |\vec{k}_l|^2 - 2\varepsilon_\nu |\vec{k}_l| \cos\theta$.

[9] Mass of the initial and final nucleon are denoted as M since it is employed the approximation $M_p \approx M_n \equiv M$.

[10] Given that the energies under consideration are on the order of GeV, the ultrarelativistic approximation is applied only in neutrinos. It is noteworthy that for leptons, this condition is most relevant for electrons, as their rest mass energy is $m_e = 0.511$ MeV. For muons and tauons, their rest mass energies cannot be neglected within this energy range.

Hadronic vertex

- Energy conservation: $E_f = M + \omega$.
- Momentum conservation: $\vec{q} = \vec{P}$.

From these relations, it can be demonstrated that the four-vector Q^α is space-like, therefore its invariant is negative:

$$E_f^2 = M^2 + q^2 \longrightarrow E_f^2 = \omega^2 + M^2 + 2M\omega = M^2 + q^2 \longrightarrow q^2 = \omega^2 + 2M\omega \tag{2.1}$$

$$|Q^2| = -Q^2 = -(\omega^2 - q^2) = -\omega^2 + \omega^2 + 2M\omega = 2M\omega > 0. \tag{2.2}$$

With the established framework and the presented expressions, we are proceeding to S-matrix calculations.

2.1.2 S-matrix calculation

The transition amplitude S_{fi} corresponding to the first-order approximation of elastic charged-current scattering of neutrino-nucleon is defined as follows:

$$S_{fi} = -i \int dX^4 H_W(X). \tag{2.3}$$

Here, $H_W(X)$ represents the Hamiltonian of this interaction, given by:

$$H_W(X) = \left(\frac{g}{2\sqrt{2}}\right)^2 (j_\alpha^{(l)})^\dagger(X) A_{(N)}^\beta(Y). \tag{2.4}$$

In this expression, g is the dimensionless weak coupling constant, connected to the Fermi constant G_F as shown in Eq. (2.5).

$$\frac{g^2}{8M_W^2} = \frac{G_F}{\sqrt{2}}; \quad G_F = 1.166 \times 10^{-5}\ \text{GeV}^2; \quad M_W = 80.401(38)\ \text{GeV}. \tag{2.5}$$

The Hamiltonian H_W can be conceptualized as the interaction between the neutrino, characterized by the leptonic current $j_\alpha^{(l)}(X)$, and the four-potential field $A_{(N)}^\beta(Y)$ created by the nucleon for this scattering. Formally, the latter can be defined as:

$$A_{(N)}^\beta(Y) = \int d^4Y \int \frac{d^4Q}{(2\pi)^4} D_W^{\alpha\beta}(Q) J_{(N)}^\beta(Y) e^{iQ(X-Y)}, \tag{2.6}$$

with $J_\beta^{(N)}(Y)$ representing the current associated to the hadronic vertex and $D^{\alpha\beta}(Q)$ the propagator of the charged weak interaction, defined in Eq. (2.7).

$$D^{\alpha\beta}(Q) = \frac{-g^{\alpha\beta} + Q^\alpha Q^\beta / M_W^2}{Q^2 - M_W^2 + i\varepsilon}. \tag{2.7}$$

It is worth noting that in elastic scattering, both terms Q^2 and $Q^\alpha Q^\beta$ can be safely neglected compared to M_W^2, and the infinitesimal factor $i\varepsilon$ is introduced to avoid singularities in the extreme case of $Q^2 \to M_W^2$. However, in elastic scattering, M_W^2 is significantly larger

than Q^2, justifying the neglect of this term. Consequently, the propagator simplifies to an expression dependent on the metric tensor $g^{\alpha\beta}$ and the mass of the boson W M_W:

$$D^{\alpha\beta} \approx \frac{g^{\alpha\beta}}{M_W^2}. \tag{2.8}$$

Regarding the definitions of the 4-vector currents in the weak interaction within the framework of Dirac Algebra (refer to Appendix A for detailed derivations), the leptonic current is expressed as a combination of a vector and axial part. The axial part accounts for parity violation, introducing a term with a sign $-(+)$ for the neutrino (antineutrino) situation:

$$j_\alpha^{(l)} = \bar{\Psi}_l(X)\gamma_\alpha(1 \mp \gamma_5)\Psi_\nu(X). \tag{2.9}$$

Similarly, the hadronic current for charged-current weak interaction incorporates a vector and axial part within the factor Γ_β, which overall characterizes the inner structure of the nucleon [40]. Denoting the subscripts f and i as the final and initial nucleon, respectively:

$$J_{(N)}^\beta = \bar{\Psi}_f(Y)\Gamma^\beta\Psi_i(Y), \tag{2.10}$$

$$\Gamma^\beta = F_1^V\gamma^\beta + i\frac{F_2^V}{2M}\sigma^{\beta\lambda}Q_\lambda + G_A\gamma^\beta\gamma^5 + \frac{G_P}{2M}Q^\beta\gamma^5. \tag{2.11}$$

Here, F_1^V and F_2^V are vector form factors, while G_A and G_P are axial and pseudoaxial form factors, all dependent on Q^2. Importantly, there exists a direct relationship between the vector part of the charged-current weak interaction and the electromagnetic interaction, known as the conserved vector current (CVC) hypothesis. This allows expressing F_1^V and F_2^V in terms of the Pauli and Dirac form factors $F_1^{n,p}$ and $F_2^{n,p}$, which can be parameterized using a dipolar contribution. A similar procedure can be applied to G_A, while for G_P, the Goldberger-Treiman relation is employed in the Partially Conserved Axial Current (PCAC) formalism. Detailed discussions on these aspects can be found in Section 2.3.

Finally, from the formal definition of the collision matrix, Eq. (2.3), a definitive expression within the framework of Dirac algebra is obtained. It is noteworthy that m_ν is introduced as a consequence of the definition of the Dirac wavefunction Ψ (refer to Appendix A.1). Although the assumption of massless neutrinos in Standard Model may lead to mathematical inconsistencies in Eq. (2.12), in this Master Thesis, we adopt the limit $m_\nu \to 0$ for the final results of the cross-section.

The derivation utilizes the mathematical properties of Dirac's delta, as illustrated in

Eqs. (2.13), (2.14) and (2.15), naturally leading to energy-momentum conservation.

$$S_{fi} = -\frac{ig^2}{8(2\pi)^4}\int d^4X \int d^4Q \int d^4Y (j_\alpha^{(l)})^\dagger(X) D_W^{\alpha\beta}(Q) J_{(N)}^\beta(Y) e^{iQ(X-Y)} \approx -i(2\pi)^4 \times$$

$$\times \int d^4Q \frac{g^2 M}{8V^2 M_W^2}\sqrt{\frac{m_\nu m_l}{\varepsilon_\nu \varepsilon_l E_f E_i}}(\bar{u}_l\gamma_\alpha(1\mp\gamma_5)u_\nu)^\dagger(\bar{U}_f\Gamma^\beta U_i)\delta^4(k_l+Q-k_\nu)\delta^4(P_f-P_i-Q) =$$

$$= -i(2\pi)^4 \frac{G_F M}{\sqrt{2}V^2}\sqrt{\frac{m_\nu m_l}{\varepsilon_\nu \varepsilon_l E_f E_i}}(\bar{u}_l\gamma_\alpha(1\mp\gamma_5)u_\nu)^\dagger(\bar{U}_f\Gamma^\beta U_i)\delta^4(k_l+P_f-k_\nu-P_i), \quad (2.12)$$

$$\int d^4X e^{i(k_l-k_\nu+Q)X} = (2\pi)^4\delta^4(k_l-k_\nu+Q), \quad (2.13)$$

$$\int d^4Y e^{i(P_f-P_i-Q)X} = (2\pi)^4\delta^4(P_f-P_i-Q), \quad (2.14)$$

$$\int d^4Q \delta^4(k_l-k_\nu+Q)\delta^4(P_f-P_i-Q) = \delta^4(P_f-P_i+k_l-k_\nu). \quad (2.15)$$

Finally, we will introduce here the invariant amplitude, defined as:

$$M_{fi} \equiv (\bar{u}_l\gamma_\alpha(1\mp\gamma_5)u_\nu)^\dagger(\bar{U}_f\Gamma^\beta U_i). \quad (2.16)$$

With the obtained results, we can further proceed with the analytic computation of cross section expressions.

2.1.3 Cross section expressions

Having established the leptonic and hadronic currents, we now possess a comprehensive expression for the collision matrix, as presented in Eq. (2.12). Beginning with the formal definition of the differential cross section, we will detail the methodology that leads to the final expressions for both the single and double differential cross sections. These expressions will be crucial in the subsequent subsections, where we will analyze their dependencies on the kinematic parameters $\cos\theta$ and ε_l.

Differential cross section

The effective differential cross section for elastic neutrino-nucleon scattering is defined as:

$$d\sigma = \frac{|S_{fi}|^2}{T\cdot|\vec{J}_{inc}|}dN_f. \quad (2.17)$$

In here,

- T represents time.
- dN_f is the density of final states, dependent on both lepton and final nucleon characteristics:

$$dN_f = \frac{V^2}{(2\pi)^6}d^3\vec{k}_l d^3\vec{P}. \quad (2.18)$$

- $|\vec{J}_{inc}|$ denotes the incident flux. In our framework, assuming a collinear scattering where the velocity directions of initial particles are the same, the derivation of the incident flux is detailed in Appendix X, resulting in:

$$|\vec{J}_{inc}| = \frac{\varepsilon_\nu \varepsilon_l V}{M k_\nu}. \quad (2.19)$$

Regarding the term $|S_{fi}|^2$, we need to multiply Eq. (2.12) by its complex conjugate. After applying the Dirac delta property shown in Eq. (2.21), we obtain:

$$|S_{fi}|^2 = \frac{G_F^2}{2}(2\pi)^4\delta^4(P_f - P_i + k_f - k_i)\frac{1}{V^4}\frac{m_\nu m_l M^2}{\varepsilon_\nu \varepsilon_l E_i E_f}|M_{fi}|^2 = \\ = \frac{G_F^2}{2}(2\pi)^4\delta^4(P_f - P_i + k_f - k_i)\frac{T}{V^3}\frac{m_\nu m_l M^2}{\varepsilon_\nu \varepsilon_l E_i E_f}|M_{fi}|^2, \tag{2.20}$$

$$[\delta^4(P_f - P_i + k_f - k_i)]^2 = \frac{TV}{(2\pi)^4}\delta^4(P_f - P_i + k_f - k_i). \tag{2.21}$$

The term M_{fi} represents the invariant amplitude, formally defined in Eq. (2.22) depending on the initial and final spin states. $|M_{fi}|^2$ derivation towards a final expression requires the application of the Trace Theorems, and a subsequent development of the contraction between the resulting leptonic tensor $\eta_{\alpha\beta}$ and hadronic tensor $W^{\alpha\beta}$, which is detailed in Appendix A.4. The final expression is found in Eq. (2.23), dependant on the W_i functions.

$$|M_{fi}|^2 = \sum_{s_i, s_f, S_i, S_f} |(\bar{u}_f \Gamma^\alpha u_i)(\bar{U}_f \Gamma_\beta U_i)|^2, \tag{2.22}$$

$$|M_{fi}|^2 \equiv 2\frac{\eta_{\alpha\beta}W^{\alpha\beta}}{m_\nu m_l} = \frac{4\varepsilon_l\varepsilon_\nu}{m_l m_\nu M^2}\left(\left(2W_1 \pm W_3\frac{\varepsilon_l + \varepsilon_\nu}{M}\right)\sin^2\frac{\theta}{2} + W_2\cos^2\frac{\theta}{2}\right). \tag{2.23}$$

$$W_1 = \frac{|Q^2|}{4M^2}[(F_1^V + F_1^V)^2 + G_A^2] + G_A^2, \tag{2.24}$$

$$W_2 = (F_1^V)^2 + \frac{|Q^2|}{4M^2}(F_2^V)^2 + (G_A)^2, \tag{2.25}$$

$$W_3 = 2G_A(F_1^V + F_2^V), \tag{2.26}$$

$$W_4 = \frac{(F_2^V)^2}{(4M)^2}(|Q^2| - 4M^2) - G_A G_P + \frac{|Q^2|}{(4M)^2}(G_P)^2, \tag{2.27}$$

$$W_5 = W_2. \tag{2.28}$$

As detailed in the Appendix A.4, once applied the condition of massless neutrinos $m_\nu \to 0$, W_4 and W_5 do not appear in the $|M_{fi}|^2$ final expression. Therefore, the pseudo-axial term G_P do not contribute in our results. Finally, we arrive at a conclusive expression for the differential cross section:

$$d\sigma = \frac{G_F^2}{4\pi^2}\frac{M}{\varepsilon_\nu}\frac{d^3\vec{k}_l}{\varepsilon_l}\frac{d^3\vec{P}}{E_f}\delta^4(k_l - k_\nu + P_f - P_i)\eta_{\alpha\beta}W^{\alpha\beta}. \tag{2.29}$$

Double differential cross section

After developing $d^3\vec{k}_l$ and integrating over the final nucleon state (check appendix A.3), we arrive at the double differential cross section:

$$\frac{d^2\sigma}{d\varepsilon_l d\cos\theta} = \frac{G_F^2}{4\pi}\frac{|\vec{k}_l|}{\varepsilon_\nu}\delta\left(\omega - \frac{|Q^2|}{2M}\right)\eta_{\alpha\beta}W^{\alpha\beta}. \tag{2.30}$$

The energy conservation term can be further simplified in terms of $\cos\theta$. Neglecting the lepton and neutrino masses and applying the ultrarrelativistic approximation for the neutrino, we obtain:

$$\delta\left(\omega - \frac{|Q^2|}{2M}\right) \approx \frac{M}{|\vec{k}_l|\varepsilon_\nu}\delta(\cos\theta_0 - \cos\theta), \tag{2.31}$$

where $\cos\theta_0 \equiv 1 - M\frac{\omega}{\varepsilon_\nu|\vec{k}_l|}$. This leads to the resulting expression for the double differential cross section, which can be further integrated over the kinematics parameters.

$$\frac{d^2\sigma}{d\varepsilon_l d\cos\theta} = \frac{G_F^2}{4\pi}\frac{M}{\varepsilon_\nu^2}\delta(\cos\theta_0 - \cos\theta)\eta_{\alpha\beta}W^{\alpha\beta}. \tag{2.32}$$

Single differential cross section

To obtain the cross section with respect the lepton energy ε_l, we need to integrate over the $\cos\theta$ variable. The resulting expression is immediately obtained using the properties of the Dirac Delta:

$$\frac{d\sigma}{d\varepsilon_l} = \int d\cos\theta \frac{d^2\sigma}{d\varepsilon_l d\cos\theta} = \frac{G_F^2}{4\pi}\frac{M}{\varepsilon_\nu^2}\eta_{\alpha\beta}W^{\alpha\beta}\Big|_{\cos\theta=\cos\theta_0}. \tag{2.33}$$

By applying the jacobian, we can obtain the single differential cross section with respect $\cos\theta$:

$$\frac{d\sigma}{d\cos\theta} = \frac{d\sigma}{d\varepsilon_l}\left|\frac{d\varepsilon_l}{d\cos\theta}\right| = \frac{G_F^2}{4\pi}\frac{M}{\varepsilon_\nu^2}\frac{|\vec{k}_l|}{1 + \frac{M}{\varepsilon_\nu} - \frac{\varepsilon_l}{|\vec{k}_l|}\cos\theta}\eta_{\alpha\beta}W^{\alpha\beta}\Big|_{\cos\theta=\cos\theta_0}. \tag{2.34}$$

This expression can be further simplified by introducing the term known as the recoil factor f_{rec}^{-1}:

$$\frac{d\sigma}{d\cos\theta} = \frac{G_F^2}{4\pi}\frac{|\vec{k}_l|}{\varepsilon_\nu}f_{rec}^{-1}\eta_{\alpha\beta}W^{\alpha\beta}\Big|_{\cos\theta=\cos\theta_0}, \tag{2.35}$$

where $f_{rec} \equiv 1 + \frac{\varepsilon_\nu(|\vec{k}_l| - \varepsilon_l\cos\theta)}{M|\vec{k}_l|}$. Either of the Eqs. (2.33) and (2.35) is useful to obtain the full cross section by integrating over the corresponding kinematic parameters. However, for the analysis with experimental data, it will be highly relevant to work with the single differential cross sections.

2.2 Response functions

In an alternative notation to the calculation involving the contraction of leptonic and hadronic tensors $\eta_{\alpha\beta}W^{\alpha\beta}$, the cross section formulae can be expressed more compactly[11] in the laboratory frame as follows:

$$\left[\frac{d^2\sigma}{d\Omega}\right]_\chi \equiv \sigma_0\mathcal{F}_\chi^2, \tag{2.36}$$

[11] As commented in [41], there are are several possibilities when introducing the term $\mathcal{F}_\chi^2$. The difference between these are the redefinition of the parameter σ_0. Whichever notation is used, the important detail to account for is that the relation (2.38) is satisfied.

where $\chi = +(-)$ refers to neutrino (antineutrino) processes. The term σ_0 is given by Eq. (2.37), expressed in terms of the Cabibbo angle[12] θ_C and a generalized angle $\tilde{\theta}$ defined in Eq. (2.39).

$$\sigma_0 = \frac{G_F^2 \cos\theta_C^2}{2\pi^2} |\vec{k}_l| \varepsilon_l \cos^2 \frac{\tilde{\theta}}{2} f_{rec}^{-1}, \tag{2.37}$$

$$\eta_{\alpha\beta} W^{\alpha\beta} = \frac{v_0}{2} \mathcal{F}_\chi^2, \tag{2.38}$$

$$\tan\frac{\tilde{\theta}}{2} \equiv \frac{|Q^2|}{v_0}; \quad v_0 = (\varepsilon_\nu + \varepsilon_l)^2 - q^2 = 4\varepsilon_\nu \varepsilon_l - |Q^2|. \tag{2.39}$$

The term $\mathcal{F}_\chi^2$ encompasses the leptonic kinematic factors (V_K) and the hadronic response functions (R_K):

$$\mathcal{F}_\chi^2 = [V_{CC} R_{CC} + 2V_{CL} R_{CL} + V_{LL} R_{LL} + V_T R_T] + \chi[2V_{T'} R_{T'}]. \tag{2.40}$$

Here, the subindexes account for different $\mu\nu$ combinations in the contraction $\eta_{\alpha\beta} W^{\alpha\beta}$. Note that 0 refers to time components, and the rest concern the direction of momentum transfer, with 3 denoting longitudinal and $1, 2$ representing transversal components.

- CC: charge-charge ($\mu\nu = 00$).
- LL: longitudinal-longitudinal ($\mu\nu = 33$).
- CL: charge-longitudinal ($\mu\nu = 03, 30$).
- T: transverse ($\mu\nu = 11, 22$).
- T': transverse pseudo-axial interference ($\mu\nu = 12, 21$).

It is noteworthy that the symmetric vector part of the tensor contraction satisfies current conservation, i.e., $Q_\mu J_V^\mu = 0$, leading to $\omega J_V^0 = q J_V^3$. In this formalism, it is thus fulfilled:

$$\eta_{03}^V = \eta_{30}^V = \frac{\omega}{q} \eta_{00}^V; \quad \eta_{33}^V = \left(\frac{\omega}{q}\right)^2 \eta_{00}^V. \tag{2.41}$$

$$W_V^{03} = W_V^{30} = \frac{\omega}{q} W_V^{00}; \quad W_V^{33} = \left(\frac{\omega}{q}\right)^2 W_V^{00}. \tag{2.42}$$

This allows us to express the vector-type functions in terms of the longitudinal contribution. To further simplify notation, we define V_L and R_L^{VV} to encompass all vector-type contributions for both leptonic and hadronic contributions, respectively. The product of these two terms, X_L^{VV}, should include all vector-type contributions in these weak response functions $\mathcal{F}_\chi^2$.

$$X_L^{VV} \equiv V_L R_L^{VV} = V_{CC} R_{CC}^{VV} + 2V_{CL} R_{CL}^{VV} + V_{LL} R_{LL}^{VV}. \tag{2.43}$$

[12]This term arises from the quark up and down mixing in the nucleon since these are different from the mass eigenstates in the weak interaction (see [42] for details). In this case, $\cos\theta_C^2 = 0.975$.

However, for the axial components, current conservation is not fulfilled. Therefore, it is not possible to simplify in the same way as with vector-type terms. We define:

$$X_{C/L}^{AA} \equiv V_{CC} R_{CC}^{AA} + 2V_{CL} R_{CL}^{AA} + V_{LL} R_{LL}^{AA}. \tag{2.44}$$

The transversal component, is expressed as follows:

$$X_T \equiv V_T (R_T^{VV} + R_T^{AA}). \tag{2.45}$$

Finally, we will define another term to encompass the pseudo-axial interference function:

$$X_{T'} \equiv 2V_{T'} R_{T'}^{VA}. \tag{2.46}$$

This leading to the final expression:

$$\mathcal{F}_\chi^2 = X_L^{VV} + X_{C/L}^{AA} + X_T + \chi X_{T'}. \tag{2.47}$$

To simplify the notation further in the response functions, we will define the adimensional parameters λ, κ, τ, δ, ρ, and ρ'. Notice that $\lambda = \tau$ due to energy-momentum conservation:

$$\lambda \equiv \frac{\omega}{2M}, \quad \tau \equiv \frac{|Q^2|}{4M^2}, \quad \kappa = \frac{q}{2M}, \tag{2.48}$$

$$\omega = \frac{|Q^2|}{2M} \rightarrow \lambda = \tau$$

$$\delta \equiv \frac{m_l}{\sqrt{|Q^2|}}, \quad \rho \equiv \frac{|Q^2|}{q^2} = \frac{\tau}{\kappa^2}, \quad \rho' \equiv \frac{q}{\varepsilon_\nu + \varepsilon_l} = \frac{\tan\tilde{\theta}/2}{\sqrt{\rho + \tan^2\tilde{\theta}/2}} \in (0,1). \tag{2.49}$$

Leptonic kinematic factors V_K

To express the different elements of the leptonic tensor $\eta_{\alpha\beta}$, we introduce the kinematic factors V_K:

$$V_{CC} = \frac{2}{v_0}\eta_{00} = 1 - \delta^2 \tan^2\frac{\tilde{\theta}}{2}, \tag{2.50}$$

$$V_{CL} = \frac{2}{v_0}\frac{1}{2}(\eta_{03} + \eta_{30}) = \frac{2}{v_0}\eta_{03} = \frac{\lambda}{\kappa} + \frac{\delta^2}{\rho'}\tan^2\frac{\tilde{\theta}}{2}, \tag{2.51}$$

$$V_{LL} = \frac{2}{v_0}\eta_{33} = \left(\frac{\lambda}{\kappa}\right)^2 + \left(1 + \frac{2\lambda}{\kappa\rho'} + \rho\delta^2\right)\delta^2\frac{\tilde{\theta}}{2}, \tag{2.52}$$

$$V_T = \frac{2}{v_0}(\eta_{11} + \eta_{22}) = \frac{\rho}{2} + \tan^2\frac{\tilde{\theta}}{2} - \frac{\delta^2}{\rho'}\tan^2\frac{\tilde{\theta}}{2}\left(\frac{\lambda}{\kappa} + \frac{\rho\rho'\delta}{2}\right), \tag{2.53}$$

$$V_{T'} = \frac{2}{v_0}\frac{i}{2}(\eta_{12} + \eta_{21}) = \frac{1}{\rho'}\tan^2\frac{\tilde{\theta}}{2}\left(1 - \frac{\lambda\rho'}{\kappa}\delta^2\right). \tag{2.54}$$

The vector type kinematic factors can be encompassed in the relation:

$$V_L \equiv V_{CC} - 2\frac{\omega}{q}V_{CL} + \left(\frac{\omega}{q}\right)^2 V_{LL}. \tag{2.55}$$

Hadronic response factors R_K

To express the different elements of the hadronic tensor $W_{\alpha\beta}$, we introduce the hadronic response factors R_K:

$$R_{CC} = W^{00} = R_{CC}^{VV} + R_{CC}^{AA}, \tag{2.56}$$

$$R_{CL} = -\frac{1}{2}(W^{03} + W^{30}) = R_{CL}^{VV} + R_{CL}^{AA}, \tag{2.57}$$

$$R_{LL} = W^{33} = R_{LL}^{VV} + R_{LL}^{AA}, \tag{2.58}$$

$$R_T = W^{11} + W^{22} = R_T^{VV} + R_T^{AA}, \tag{2.59}$$

$$R_{T'} = -\frac{i}{2}(W^{12} - W^{21}) = R_{T'}^{VA}. \tag{2.60}$$

It is noteworthy that the vector-type components can be expressed as:

$$R_L^{VV} \equiv \left(\frac{q^2}{|Q^2|}\right)^2 \left[W_{VV}^{00} - \frac{\omega}{q}(W_{VV}^{03} + W_{VV}^{30}) + \left(\frac{\omega}{q}\right)^2 W_{VV}^{33}\right] = W_{VV}^{00} = R_{CC}^{VV}. \tag{2.61}$$

This formalism can be further detailed with the introduction of nucleon form factors (Section 2.3 is devoted to their formal description). The vector contribution can be expressed using the weak isovector Sachs form factor G_E^V (check Eq. (2.72)):

$$R_L^{VV} = R_{CC}^{VV} = \frac{\kappa^2}{\tau}(G_E^V)^2, \tag{2.62}$$

while the axial contribution is described by the weak axial Sachs form factor G^A, formally defined with respect to the axial G_A and pseudo-axial G_P nucleon form factors:

$$G^A \equiv G_A - \tau G_P, \tag{2.63}$$

$$R_{CC}^{AA} = W_{AA}^{00} = \frac{\kappa^2}{\tau}\left(\frac{\lambda}{\kappa}\right)^2 (G^A)^2, \tag{2.64}$$

$$R_{LL}^{AA} = W_{AA}^{33} = \frac{\kappa^2}{\tau}(G^A)^2, \tag{2.65}$$

$$R_{CL}^{AA} = -\frac{1}{2}(W_{AA}^{03} + W_{AA}^{30}) = -\frac{\kappa^2}{\tau}\frac{\lambda}{\kappa}(G^A)^2. \tag{2.66}$$

Lastly, the transversal components are expressed if we introduce the other weak isovector Sachs formfactor G_M^V (Eq. (2.73)):

$$R_T^{VV} = W_{VV}^{11} + W_{VV}^{22} = 2\tau(G_M^V)^2, \tag{2.67}$$

$$R_T^{AA} = W_{AA}^{11} + W_{AA}^{22} = 2(1+\tau)(G_A)^2, \tag{2.68}$$

$$R_{T'}^{VA} = -\frac{i}{2}(W_{VA}^{12} - W_{VA}^{21}) = -2\sqrt{\tau(1+\tau)}G_M^V G_A. \tag{2.69}$$

2.3 Hadronic structure

To incorporate the information of the internal nucleon structure, various form factors have been employed: vector (F_1^V and F_2^V), axial (G_A) and pseudo-axial (G_P). This section provides a formal description and modeling of these contributions, serving as the final step before comparing the theoretical results from neutrino-nucleon scattering with experimental neutrino-nuclei cross-section data in Section 2.4.

Vector structure

Analogous to the electromagnetic interaction, the vector-type form factors F_1^V and F_2^V representing the inner nucleon structure in Eq. (2.11) can be expressed using the Conserved Vector Current (CVC) in terms of Dirac ($F_1^{n,p}(Q^2)$) and Pauli ($F_2^{n,p}(Q^2)$) form factors [43]. These are closely related to the electric and magnetic Sachs form factors $G_{E,M}^{n,p}(Q^2)$.

$$G_E^{n,p} \equiv F_1^{n,p} - \tau F_2^{n,p}, \tag{2.70}$$

$$G_M^{n,p} \equiv F_1^{n,p} + F_2^{n,p}, \tag{2.71}$$

where τ is formally defined in Eq. (2.48). For neutrino-nucleon scattering, F_1^V and F_2^V exhibit a similar relation to the isovector weak Sachs form factors $G_{E,M}^V$, which are related to $G_{E,M}^{n,p}$. This leads to a formal description of F_1^V and F_2^V in terms of $G_{E,M}^{n,p}$, as expressed in Eq. (2.74).

$$F_1^V - \tau F_2^V \equiv G_E^V = G_E^p - G_E^n, \tag{2.72}$$

$$F_1^V + F_2^V \equiv G_M^V = G_M^p - G_M^n, \tag{2.73}$$

$$F_1^V = \frac{(G_E^p - G_E^n) + \tau(G_M^p - G_M^n)}{2(1+\tau)}, \quad F_2^V = \frac{(G_M^p - G_M^n) - (G_E^p - G_E^n)}{2(1+\tau)}. \tag{2.74}$$

To gain further insight into the dependence on the transferred four-momentum Q^2 in the electric and magnetic Sachs form factors, we consider extreme scenarios in the original electromagnetic electron-nucleon scattering. In the static limit ($Q^2 \to 0$), the kinematics result in the interaction of the lepton with a point-like particle with charge +e (proton) or null charge (neutron). Therefore, the form factor must satisfy:

$$F_1^p(0) = 1, \quad F_1^n(0) = 0, \tag{2.75}$$

$$F_2^p(0) = 0, \quad F_2^n(0) = 1, \tag{2.76}$$

leading to:

$$G_E^p(0) = 1, \quad G_E^n(0) = 0, \tag{2.77}$$

$$G_M^p(0) = \mu_p = 2.793, \quad G_M^n(0) = \mu_n = -1.913, \tag{2.78}$$

where $\mu_{n,p}$ represent the neutron or proton magnetic momentum. In contrast, the asymptotic limit ($Q^2 \to \infty$), necessitates a study through QCD.
However, the established parametrizations of $G_{E,M}^{n,p}$ are derived from experimental data. In this project, the Galster dipolar parametrization will be utilized [44], proposing the expression of the Sachs weak isovector in terms of functions from a dipolar contribution $G_D(Q^2)$, defined as:

$$G_D(Q^2) = \frac{1}{\left(1 + \frac{|Q^2|}{M_V^2}\right)^2}, \tag{2.79}$$

where $M_V = 0.843$ GeV is the vector mass. It can be verified that the static limit is satisfied: $G_D(Q^2 \to 0) \to 1$. The electric and magnetic Sachs factors can be expressed in

this parametrization as:

$$G_E^p = G_D^V, \quad G_E^n = -\mu_n \tau G_D^V \varepsilon_n, \quad G_M^p = \mu_p G_D^v, \quad G_M^n = \mu_n G_D^v, \tag{2.80}$$

$$\varepsilon_n = (1 + \lambda_n \tau)^{-1}, \quad \lambda_n = 5.6. \tag{2.81}$$

Axial structure

From the inner nucleon structure, the axial structure is composed of the axial G_A and the pseudo-axial G_P form factors.

Current data is not sufficient to model the functional form of G_A. However, a dipolar contribution is widely used as an analogy to the vector-type form parametrization.

$$G_A(Q^2) = \frac{g_A}{\left(1 + \frac{Q^2}{M_A^2}\right)^2}, \tag{2.82}$$

where $g_A = -1.267$ is the axial-vector coupling constant and $M_A = 1.03$ GeV, the nucleon axial mass.

Concerning the pseudo-axial term G_P, it can be related to the axial form factor G_A via Goldberger-Treiman relation, Eq. (2.83), within the Partially Conserved Axial Current (PCAC) formalism.

$$G_P(Q^2) = \frac{4M^2}{|Q^2| + m_\pi^2} G_A(Q^2), \tag{2.83}$$

with m_π being the pion mass. However, as stated in Appendix A.4, once applied the condition of massless neutrinos $m_\nu \to 0$, the pseudo-axial term G_P does not appear in our results since its contribution (included in W_4 and W_5 terms) vanishes, as displayed in Eq. (2.23).

2.4 Comparison with light nuclei experimental data

After describing the formalism employed for neutrino-nucleon elastic scattering and presenting the Galster dipolar parametrization to model the nucleon form factors, we compare these theoretical results with experimental data of neutrino-light nuclei interactions[13], displayed in Figures **11** and **12**. Specifically, we include data from:

- Deuterium (D^2) from Argonne National Laboratory in 1973 [45] and 1977 [46] and from Brookhaven National Laboratory [47].
- Bromotrifluoromethane (CF_3Br) from the Gargamelle experiment in 1977 [48].
- Propane (C_3H_8) from the Gargamelle experiment in 1979 [49].

[13]The experimental data used has been obtained from the Quasielastic channel in the corresponding neutrino-nucleus interaction (see Chapter 3), in which one of the nucleons is ejected from the nuclear medium.

It is noted that the predicted results overestimate the data, especially with antineutrinos, where heavier nuclei are targeted. In contrast, the agreement with deuterium data is better, though the theoretical results do not fully enclose within the error bars despite achieving the same order of magnitude. Additionally, the disagreement increases with higher incident neutrino energy, indicating that nuclear effects[14], such as multi-nucleon emission or the nucleon-nucleon correlations, become more significant in the cross-section as neutrino energy increases.

Since no nuclear effects were accounted for in this theoretical approach, a poor agreement is expected. To accurately improve the goodness of the reproduction of these results, nuclear effects must be properly described and implemented. Henceforth, this task will be addressed in Chapter 3, leaving the current chapter as an introduction to the neutrino-nucleus scattering theoretical framework.

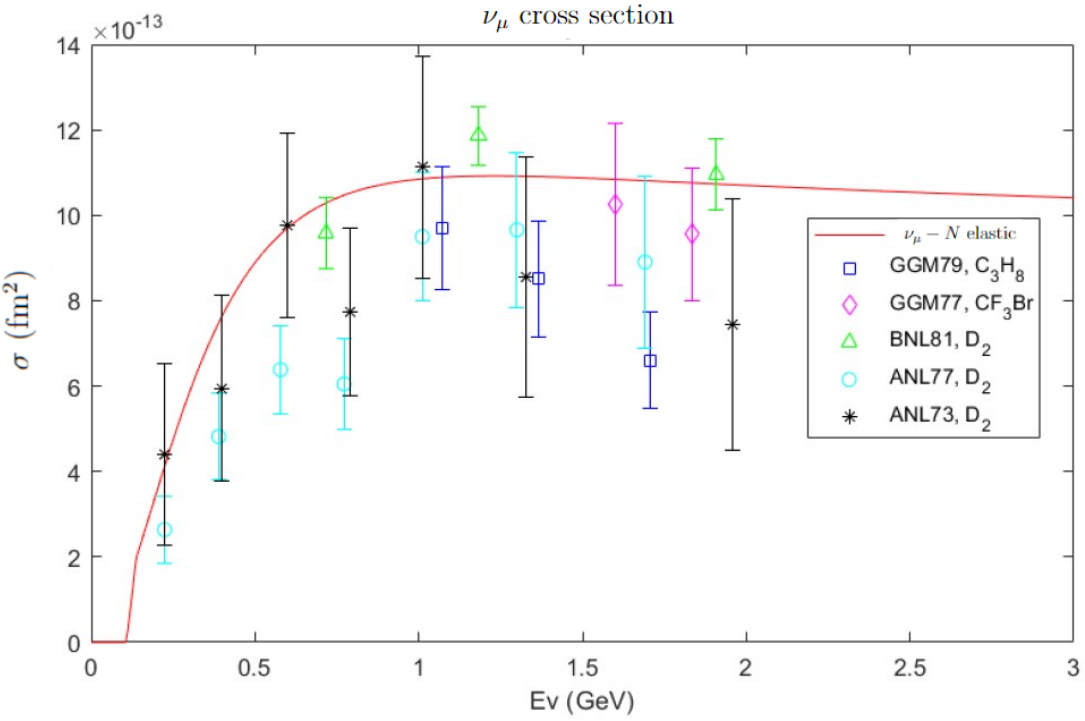

Figure 11: Comparison of experimental results with the elastic scattering results of the charged-current $\nu_\mu - N$ case. Data extracted from the publications [45]–[49].

[14]The theoretical approach of some of these nuclear effects, such as Fermi motion or nucleon removal energy, are discussed in Chapter 3. A list of those considered during the implementation in the Monte Carlo generators can be found in Appendix C.2.

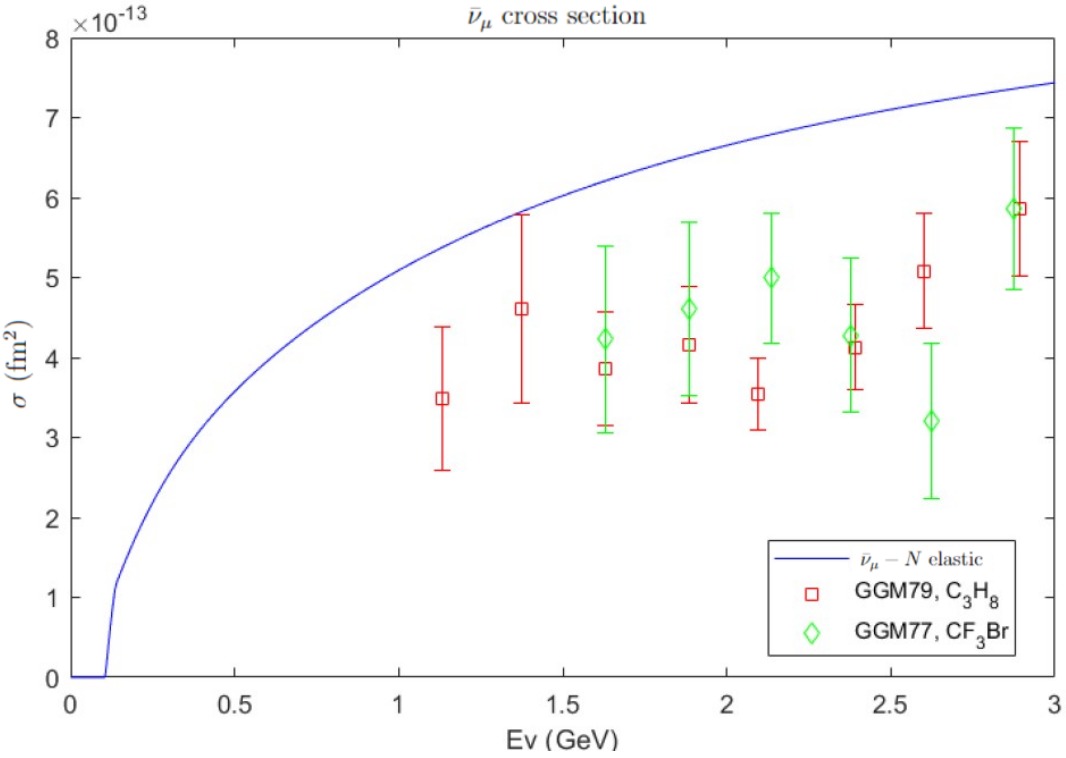

Figure 12: Comparison of experimental results with the elastic scattering results of the charged-current $\bar{\nu}_\mu - N$ case. Data extracted from the publications [48], [49].

3 Neutrino-nucleus scattering

Developing the charged-current elastic scattering neutrino-nucleon inclusive cross-section formalism in Chapter 2 constitutes the basics of modelling the charged-current neutrino-nucleus weak interactions. The next step is to include the nuclear effects in the neutrino energy range from hundreds of MeV to tens of GeV. Hence, in this chapter it is given a big overview of the processes involved in this regime to provide a comprehensive theoretical description of the nuclear responses, being essential for establishing the theoretical foundation required to effectively analyse the experimental muon neutrino 2020 data from T2K in Part III.

Neutrino-nucleus scattering encompasses various reaction channels dependent on the transferred energy ω. Figure 13 provides an overview of these processes, including:

- **Elastic scattering**. There is a transfer of energy from the neutrino to the nucleus, altering the kinematics of the incident particles while the nuclear structure remains unchanged.
- **Giant resonances (GR)**, resulting in a collective motion of protons and neutrons in opposite directions within the nucleus.
- **Quasielastic (QE) and 2-Nucleon interaction (2N)**, which are of interest in this Thesis, detailed in Section 3.1.
- **Pion production**, resulting from nucleon excitation via resonant (Δ) or non-resonant (N^*) processes.
- **Deep inelastic scattering (DIS)**. The incident neutrino interacts directly with the quarks, breaking the nucleon bound quantum system.

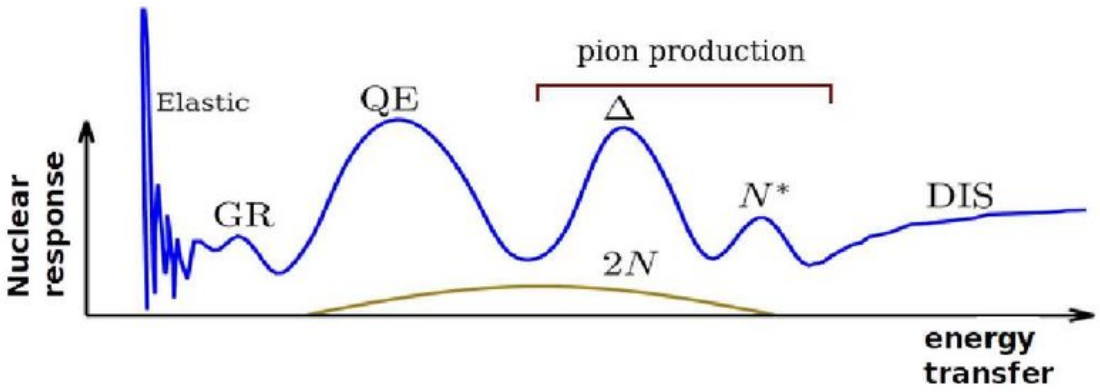

Figure 13: Nuclear response functions as a function of the energy transfer ω [50]. For the range of study (low energies up to few GeV) this Thesis focuses on processes involving no pions in the final state (CC0π), where the Quasielastic (QE) regime predominates.

For current and forthcoming experiments, the operational range extends to the order of few GeV, where resonances beyond QE may appear. However, this Thesis focuses on charged-current processes wherein no pions are emitted in the final state, referred to as CC0π. These interactions can be selected accurately by the detectors as proceed in T2K (see Part III). Therefore, our initial focus will be on comprehending the mechanisms involved in CC0π processes, explained in Section 3.1.

The impact of nuclear effects on the final state is significant; however, a detailed theoretical model description exceeds this Thesis work. Therefore, it will be provided an in-depth theoretical examination of nuclear models specifically for CCQE interactions in Section 3.2. The models discussed include the Relativistic Fermi Gas (RFG), Super Scaling Analysis version 2 (SuSAv2), and Spectral Function (SF), each tailored for the QE region.

It is important to note that these models applied in the QE regime are based on the Impulse Approximation (IA). Other approaches to account for nuclear correlations, such as resonance production, require alternative theoretical frameworks beyond IA that are outside the scope of this Thesis.

3.1 CC0π Channel Reactions

This section offers an overview of the processes considered within CC0π: CCQE, meson exchange current (MEC-2p2h) and pion absorption. Understanding these mechanisms is crucial for modeling nuclear responses and improving the accuracy of the predictions from Monte Carlo generators.

Charged-current Quasielastic (CCQE)

In the Quasielastic regime, a neutrino interacts with a nucleus $X(Z, A)$, so that in the final state, a charged-lepton and an outgoing nucleon emerge, leading to a knock-out reaction:

$$\nu_l + X(Z, A) \longrightarrow l^- + p + Y(Z, A-1),$$
$$\bar{\nu}_l + X(Z, A) \longrightarrow l^+ + n + Y(Z-1, A-1),$$

where p (n) denotes the respective proton (neutron) emitted after the interaction with the neutrino (antineutrino). Figure 14 displays the respective lowest-order Feynman diagram.

Unlike neutrino-nucleon scattering, the hadron is not static (although the nucleus can be considered static) and due to the nuclear effects within, the nucleon is considered quasi-free. More specifically, there is a change since the latter goes from being bounded to gain enough energy to go to the continuous. These bounding nucleon effects are accounted effectively based on the collective influence of the rest of the nucleons. Many theoretical approaches evaluate these effects within the IA, from which the neutrino is assumed to interact solely with a nucleon, leading to a one-body operator in the S-matrix calculus.

In this Thesis context, three nuclear models will be described in Section 3.2: RFG, SuSAv2 and SF; which will be used in Part III to obtain results from Monte Carlo generators.

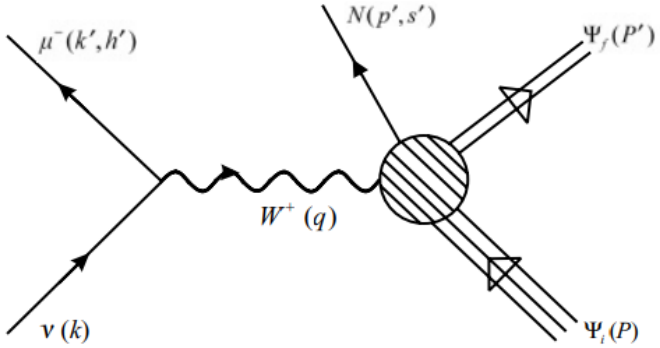

Figure 14: Lowest-order Feynman diagram of a charged-current neutrino-nucleus scattering in the Quasielastic regime (CCQE). The final state involves a charged muon and a free nucleon, leading to a knock-out process [51].

Two-particle two-hole Meson Exchange Currents (2p2h-MEC)

2p2h-MEC involves those processes where multiple nucleons are emitted from the nucleus via the exchange of virtual mesons between the nucleons. In 2p2h-MEC contributions, the weak boson from the leptonic current is exchanged by a pair of nucleons, leading to a 2-nucleon emission as similarly seen in Figure **15** for the case of lepton-nucleus interaction.

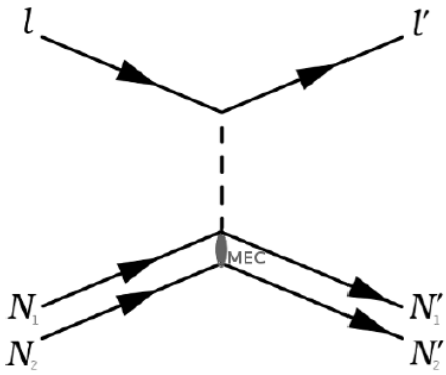

Figure 15: Scheme of a MEC process in lepton-nucleus interaction. Figure extracted from [52].

The inclusion of 2-body current at tree-level via π exchange[15] is considered in a highly sophisticated formalism described in [53]. The main idea is that there are different processes leading to a 2-nucleon emission that must be accounted when computing the hadronic tensor. These processes can be observed in Figure **16**:

[15] At the energies considered, heavier mesons like ρ are very unlikely to contribute significantly, therefore having pions the predominant role as the meson exchanged between nucleons.

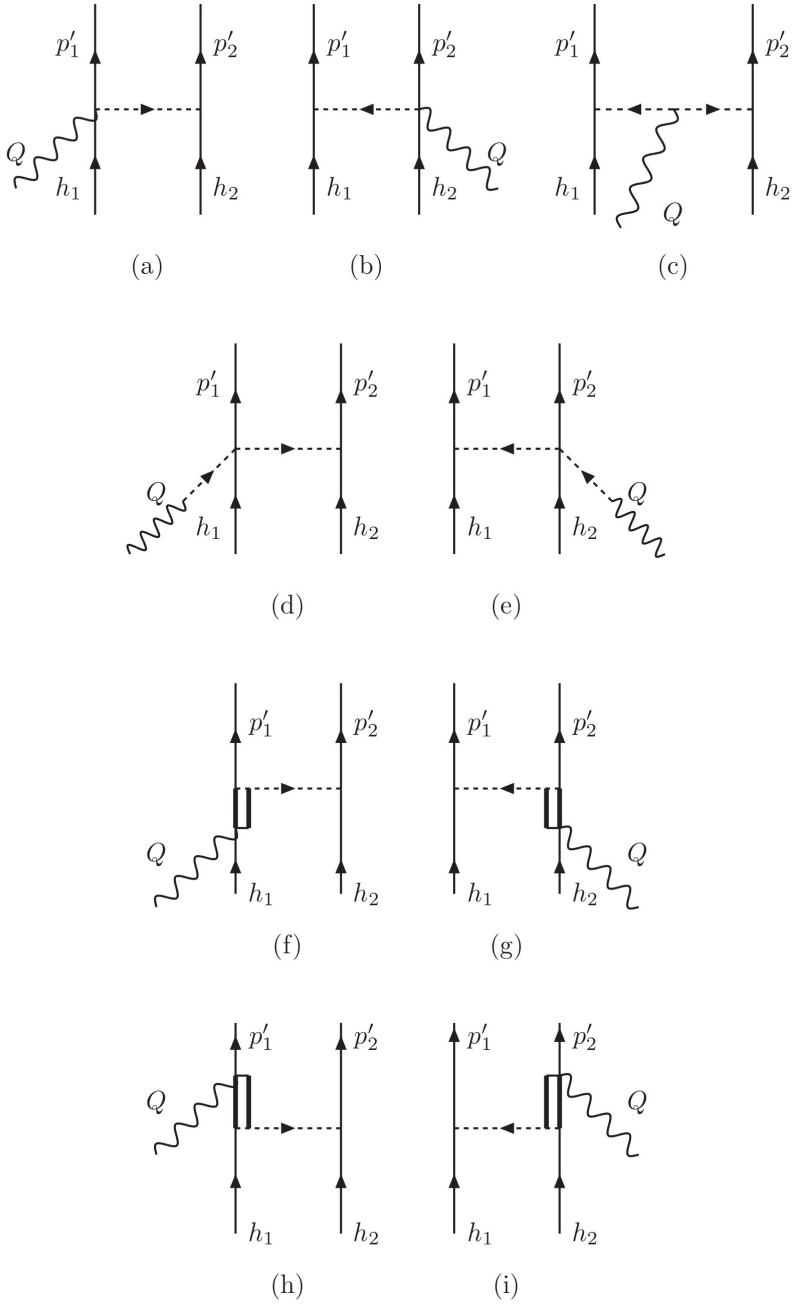

Figure 16: Lowest-order MEC Feynman diagrams in the theoretical study [53], including seagull (a,b), pion-in-flight (c), pion-pole (d,e) and Δ pole (f-i) contributions.

- Seagull or contact terms (a,b): the charged boson interacts in the $NN\pi$ vertex.
- Pion-in-flight (c): the boson interacts with the virtual pion directly. Its axial part vanishes, therefore being purely vector contribution.
- Pion-pole (d,e): the boson decays into a virtual pion that interacts directly with the nucleons, thus resulting in two pion propagators. Its contribution is purely axial, therefore being absent in electromagnetic scattering.

- Δ pole: Δ resonance is achieved during the two-nucleons interaction. Depending on the time reference of the resonance, it is distinguished between forward (f,g) and backward (h,i) Δ pole processes.

Pion absorption

In the GeV energy range, neutrino interactions with nuclei often produce pions. However, due to the strong interaction, pions frequently undergo absorption within the nuclear medium, resulting in no pions in the final state. This phenomenon, known as pion absorption, can present difficulties since it may be misidentified as a quasielastic event.

Various mechanisms can cause pions to interact with a nucleus, but at GeV energies, pion absorption is predominantly mediated by an intermediate Δ resonance state:

$$\pi + N \longrightarrow \Delta, \quad \Delta + N \longrightarrow N + N. \tag{3.1}$$

Understanding Pion Absorption is crucial for accurately reconstructing neutrino energy in experiments using Monte Carlo generators, as employed in Part III. Experimental studies, such as [54], have highlighted the challenge of distinguishing true CCQE events from CC1π events, as illustrated in Figure 17.

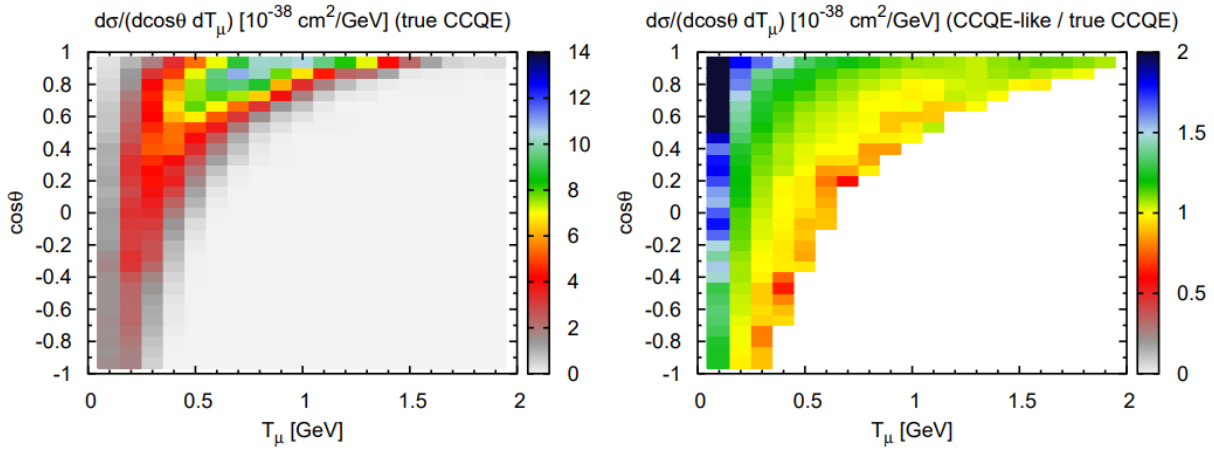

Figure 17: Double differential cross section on ^{12}C as a function of the muon scattering angle in $\cos\theta$ and the muon kinetic energy T_μ. In the left it is displayed the true CCQE events whilst in the right it is shown the ratio between of the CCQE detections and the true CCQE events [54]. Notice how Pion Absorption is noticeable for high energy transfer (low T_μ) and forward angles.

3.2 Nuclear models in CCQE processes

This section focuses on CCQE processes, delving in how to properly account for nuclear dynamics through various models: RFG, LFG, SuSAv2, and SF. However, the frameworks of the first two models rely on the phenomena of scaling. Hence, we begin with an introduction to scaling and superscaling whilst defining the scaling variable and the

scaling function.

Subsequently, we examine the RFG model, which describes the many-body dynamics within the nucleus by assuming a relativistic Fermi gas motion, resulting in an independent-particle relativistic description. However, RFG exhibits limitations when compared to experimental data, primarily due to the scaling functions employed, thereby constituting the basis for more sophisticated nuclear response models. An enhanced version, known as Local Fermi Gas (LFG) [55], considers a more realistic distribution of nucleon momenta within the nucleus.

To improve the treatment of nuclear dynamics, the Super Scaling Analysis (SuSA) incorporates within the RFG formalism an universal scaling function derived from electron scattering data. SuSA exhibits better agreement with experimental results compared to the RFG model. SuSAv2 extends this approach by including scaling functions from the relativistic mean field (RMF) and the relativistic plane wave impulse approximation (RPWIA), offering a more realistic framework in the description of final state interactions (FSI) while adopting a relativistic treatment of the nucleon dynamics.

Alternatively, a phenomenological approach to nuclear structure and dynamics is provided by the SF model. While this method simplifies the formalism, it lacks accuracy in accounting for FSI and nucleon-nucleon correlations. Nevertheless, SF offers computational efficiency with greater accuracy than RFG.

These models will be utilised in Monte Carlo generators to simulate CCQE events, as discussed in Part III. For processes involving MEC-2p2h, a formalism beyond the IA is necessary. For instance, the SuSAv2-MEC model employs relativistic calculations based on the RFG [56]. However, Pion Absorption employs an empirical FSI model known as hA, whose description falls outside the scope of this Master's thesis.

3.2.1 Introduction to scaling and superscaling models

In neutrino-nucleus scattering, modeling the behavior of nuclei in kinematic analyses presents difficulties in computing the complex response function due to multiple nucleons participating in the scattering process or emerging nuclear effects. However, in the QE regime, the predominant interaction involves an exchange of energy (ω) and momentum ($\vec{q}$) with a single nuclear component, allowing these parameters to be considered initially independent in the IA.

Under certain kinematic conditions, the nuclear response becomes dependent on the combination of both ω and $\vec{q}$, conventionally known as the scaling variable $\psi(\omega, \vec{q})$. Within the context of this Thesis, the phenomenological scaling function $f(\psi, \vec{q})$ is defined as the experimental differential cross-section divided by the single-nucleon cross section divided over the Fermi momentum k_F, establishing a relationship between the nuclear response

and the response of free nucleons [57].

$$f(\psi, \vec{q}) = \frac{1}{k_F} \frac{\left(\frac{d^2\sigma}{d\varepsilon_l d\Omega}\right)_{exp}}{\left(\frac{d^2\sigma}{d\varepsilon_l d\Omega}\right)_{s.n.}} \tag{3.2}$$

The concept of scaling first appeared in other fields such as solid-state physics and atomic physics. In high-energy physics, scaling phenomena are particularly prominent in deep inelastic lepton scattering, where the nuclear response depends on the scaling Bjorken parameter x (measured in the 1970s with electrons scattering (e, e') [58]). Analogously, a similar phenomenon known as y-scaling emerged, focusing on determining nuclear responses for lepton-nucleus scattering under specific kinematics [59]–[61]. Experimental analyses of y-scaling confirmed the dominant behavior of leptons interacting with nucleus constituents in the QE regime as one-body knock-out reactions. In this phenomenon, at sufficiently high momentum transfer values, the scaling function becomes dependent solely on the scaling variable:$f(\psi, \vec{q}) = f(\psi)$.

Depending on the nature of the scaling, various behaviors can be distinguished:

- Scaling of zero-th kind: the longitudinal and transverse scaling functions are equal, denoted as $f_L = f_T \equiv f$, where the distinction between longitudinal and transverse is made with respect to the direction of the momentum transfer $\vec{q}$. The total scaling function f can be related to the cross-section, while f_L and f_T are associated with the longitudinal R_L and transverse R_T nuclear responses respectively, as it will be seen in Eqs.(3.38)-(3.43) for SuSAv2.
- Scaling of first kind: the scaling function is independent of q, being explicitly dependent only on the scaling variable ψ, as seen in the left graphs from Figure **18**.
- Scaling of second kind: the scaling function is independent of the nuclear species, as observed in the right pannel of Figure **18**.
- Superscaling: both scaling of first and second kind conditions are met simultaneously. The scaling function can therefore be expressed as a function only of the scaling variable, this is: $f(\psi, \vec{q}) = f(\psi)$.

In the context of the QE regime, the dominant process involves an initial elastic scattering of neutrino-nucleon (subject to certain nuclear constraints), followed by ejection from the nucleus. Consequently, the nuclear form factors can be considered highly related to the hadronic form factors derived from the single nucleon analysis. This justifies the approach taken in establishing the relationship between the nuclear response function and the hadronic response via the scaling function.

In the theoretical description of the RFG and LFG models for neutrino-nucleus scattering, scaling phenomena appear implicitly. The strategy adopted is to compute the

inclusive cross-section under the IA, where the nuclear responses depend on the responses of single nucleons and the corresponding scaling functions. Thus, this Thesis aims at describing both the theoretical RFG scaling function and the more realistic SuSA and SuSAv2 scaling functions.

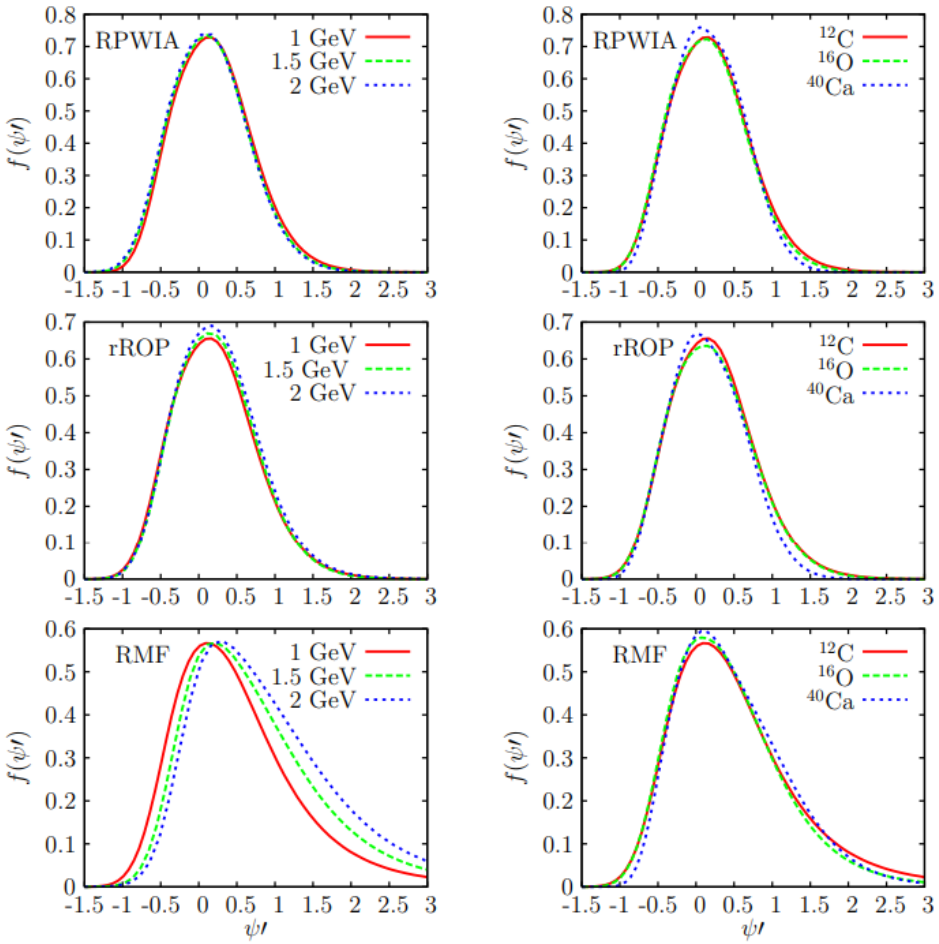

Figure 18: Example of different kinds of scaling. The theoretical scaling functions correspond to neutrino-nucleus scattering evaluated within different nuclear response models: RPWIA, rROP (RMF using a real optical potential to account for inelastic channels) and RMF. Notice that the left graphs denote the behaviour for different incident energies, thereby exhibiting scaling of first kind, whilst the right graphs display the behaviour for different nuclei, satisfying scaling of second kind. Figure extracted from [62].

3.2.2 Relativistic Fermi Gas (RFG)

The RFG model is the simplest description of a fully relativistic nuclear system in which the response functions can be computed analytically [62].

Kinematics

In neutrino-nucleus interaction, the nucleus is assumed to be originally at rest, although the nucleons within are continuously moving, i.e. they have non-zero momenta. Adopting the notation from single nucleon case, we now need to account for nucleons in the

kinematics description, thereby leading to:

- Neutrino ν_l: $K^\alpha_\nu = (\varepsilon_\nu, \vec{k}_\nu)$.
- Initial nucleus N_i: $P^\alpha_i = (M_i, \vec{0})$.
- Initial bound nucleon that will break free n_i: $p^\alpha_{n,i} = (\varepsilon_{n,i}, \vec{p}_{n,i})$.
- Lepton l^-: $K^\alpha_l = (\varepsilon_l, \vec{k}_l)$.
- Final nucleus N_f: $P^\alpha_f = (E_f, \vec{P})$.
- Final free nucleon n_f: $p^\alpha_{n,f} = (\varepsilon_{n,f}, \vec{p}_{n,f})$.
- Exchanged boson W^-: $Q^\alpha = (\omega, \vec{q})$.

The collective nucleon interaction is accounted directly in the nuclear binding effect, formally introduced with the Fermi momentum parameter k_F and the energy shift E_{shift}. This representation implies that nucleons momenta are initially below[16] k_F, which remains locally constant within the nucleus in this model. Employing the IA lead to neutrino interacting solely with a bound nucleon, thus giving enough energy to break free from nuclear binding ($p_{n,f} > k_F$) and the final nucleon is on-shell[17].

Both the energy shift and the Fermi momentum vary depending on the nuclear species. From electron inclusive scattering data analysis it has been extracted relative values that are taken as references[18] [60]. To have some examples, Table **1** displays the former parameters for different nuclei, whilst in Figure **19** it is observed the effects of k_F and E_{shift} in inclusive (e, e') cross sections on ^{12}C within the RFG formalism.

[16] Since nucleons are fermions, special attention must be put in Pauli exclusion principle. The resulting effect, known as Pauli blocking, will be explained in the Appendix C.2.

[17] On-shell condition implies that the momentum and the energy of a given particle satisfy the relation $E^2 = m^2 + p^2$. Initially, nuclear binding effects lead to an extra contribution in energy different from momentum ($\varepsilon^{RFG}_{n,i} \to \varepsilon^{free}_{n,i} + E_{shift}$, with $\varepsilon^{free}_{n,i}$ the nucleon energy if it were originally unbound from nucleus), thus the former relation is not satisfied anymore (off-shell condition). When the nucleon is free from nucleus after the interaction with neutrino, the energy-momentum equation is satisfied, i.e. on-shell.

[18] Notice that we are not referring here to absolute values since k_F is adjusted to fit with respect scaling functions ψ', while E_{shift} is adapted to reproduce the shift in the quasielastic peak.

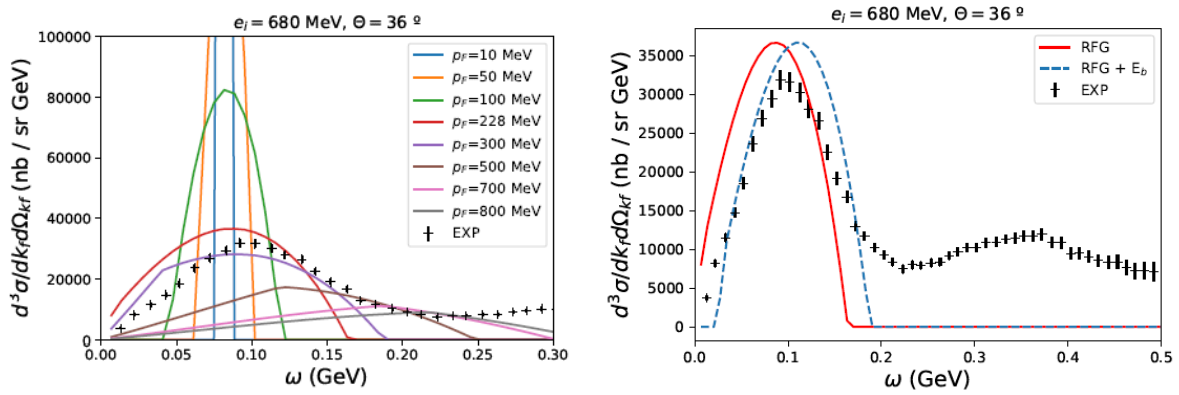

Figure 19: Inclusive $(e,^{12}C)$ cross section theoretical results (continuous lines) in RFG with respect the experimental data (black dots) for an incident energy of 680 MeV at 36º. It can be seen in the left how the distribution changes sharply with increasing values of k_F and in the right the horizontal shift caused by the consideration of $E_{shift} = 20$ MeV in the prediction.

Nucleus	k_F (MeV/c)	E_{shift} (MeV)
Lithium	165	15
Helium	200	15
Carbon	228	20
Magnesium	230	25
Aluminium	236	18
Calcium	241	28
Iron	241	23
Nickel	245	30
Tin	245	30
Gold	245	25
Lead	248	31

Table 1: Values of Fermi momentum k_F and energy shift E_{shift} for different nuclei, which have been determined via electron inclusive scattering measurements [60].

Formalism in inclusive cross section

In this framework, the nucleons wave functions can be modelled as plane waves multiplied by the Dirac spinors $u_s(\vec{p})$:

$$\Psi_{\vec{p},s}(\vec{r}) = \frac{1}{\sqrt{V}} e^{i\vec{p}\cdot\vec{r}} u_s(\vec{p}). \tag{3.3}$$

In RFG, the nuclear description given by the hadron tensor $W^{\alpha\beta}$ is formally characterised by the approximation to one-body operator (leading to 1p1h excitation) and the Heaviside distributions $\Theta(k_F - |\vec{p}_{i,j}|)$ and $\Theta(|\vec{p}_{n,f}| - k_F)$ to refer to initial nucleon being bound in

the nucleus and then breaking into the continuum after the interaction.

$$W^{\alpha\beta} = \sum_{\vec{p}_{n,i}} \sum_{s_i, s_f} \delta(\varepsilon_{n,f} - \varepsilon_{n,i} - \omega) \frac{M^2}{\varepsilon_{n,i}\varepsilon_{n,f}} J^{\alpha\star}_{s_f,s_i}(\vec{p}_{n,f}, \vec{p}_{n,i}) J^{\beta}_{s_f,s_i}(\vec{p}_{n,f}, \vec{p}_{n,i}) \times \\ \times \Theta(k_F - |\vec{p}_{n,i}|)\Theta(|\vec{p}_{n,f}| - k_F). \tag{3.4}$$

Considering the thermodynamic limit, i.e. the number of nucleons is sufficiently large so the density is uniform, summing over the initial nucleon momentum becomes an integral operation, introducing the volume $V = 3\pi^2 N/k_F^3$ for the nuclear system with N total number of nucleons. This leads to an expression of the RFG hadron current that is related to the free nucleon hadron tensor ($\equiv w^{\alpha\beta}_{s.n.}$):

$$W^{\alpha\beta} = \frac{V}{(2\pi)^3} \int d^3 p_{n,i} \delta(\varepsilon_{n,f} - \varepsilon_{n,i} - \omega) \frac{M^2}{\varepsilon_{n,i}\varepsilon_{n,f}} 2 w^{\alpha\beta}_{s.n.} \Theta(k_F - |\vec{p}_{n,i}|)\Theta(|\vec{p}_{n,f}| - k_F) \tag{3.5}$$

Regarding the energy transferred from neutrino to the nucleon, there is a need to redefine this term in RFG framework. When the nucleon reaches the continuum, the final nuclei can get excited by an energy ω_0. Denoting M_i and M_f the rest-mass energies of the initial and final nucleus respectively, ω_0 is formally defined as shown in Eq. (3.6). Therefore, the energy-momentum conservation of the electroweak process changes naturally into Eq. (3.7). The effective transferred energy ω' from the neutrino to the nucleon is thereby displayed in Eq. (3.8).

$$\omega_0 \equiv \frac{1}{2M_i}(M_f^2 - M_i^2), \tag{3.6}$$

$$\omega = \omega_0 + \frac{|Q^2|}{2M_i} = \varepsilon_\nu - \varepsilon_l, \tag{3.7}$$

$$\omega' = \omega - E_{shift}, \tag{3.8}$$

With the former considerations, the mathematical procedure to compute the inclusive cross section follows the same derivation as the one described for the elastic neutrino-nucleon scattering described in Chapter 2: developing the S-matrix with the new hadronic tensor expression, computing the corresponding integrals and calculating $|M_{fi}|^2$. For simplicity, we will remark the inclusive cross section results with this formalism (see [62] for clarifications of the implicit mathematical steps).

Starting from the double differential cross section and employing the weak response function notation $\mathcal{F}_\chi^2$, we get:

$$\frac{d\sigma}{dk_l d\Omega} = \frac{\varepsilon_l}{\varepsilon_\nu} \frac{G_F^2}{4\pi^2} \frac{v_0}{2} \mathcal{F}_\chi^2, \tag{3.9}$$

while the single differential cross section maintains the same structure with respect the free nucleon case:

$$\frac{d\sigma}{d\Omega} = \sigma_0 \mathcal{F}_\chi^2. \tag{3.10}$$

Nuclear response functions

In QE regime, the difference with respect the free nucleon situation relies on the nuclear response, therefore, these are redefined following the general structure:

$$R_K^{RFG} = \frac{N}{k_F}\Lambda_0 f_{RFG}(\psi) U_K. \tag{3.11}$$

The former expression involves the usage of the parameters κ, λ and τ defined in Eq. (2.48) alongside the dimensionless Fermi parameters η_F and ξ_F:

$$\eta_F = \frac{k_F}{M}, \quad \xi_F = \sqrt{1+\eta_F^2} - 1. \tag{3.12}$$

By using the latter, Eq. (3.11) is decomposed in:

- N the corresponding number of nucleons, since in charged-current interactions, neutrinos (antineutrinos) interact only with neutrons (protons).
- The RFG scaling function $f_{RFG}(\psi')$ based on the scaling variable ψ:

$$\psi \equiv \frac{1}{\sqrt{\xi_F}} \frac{\lambda - \tau}{\sqrt{(1+\lambda)\tau + \kappa\sqrt{\tau(\tau+1)}}}. \tag{3.13}$$

  However, we will redefine the scaling variable as ψ' to account for the energy shift within the energy transferred ω' since the scaling function considers by definition the nuclear effects and the energy shift is amongst them:

$$\psi' \equiv \frac{1}{\sqrt{\xi_F}} \frac{\lambda' - \tau'}{\sqrt{(1+\lambda')\tau' + \kappa\sqrt{\tau'(\tau'+1)}}}, \tag{3.14}$$

$$\lambda' = \frac{\omega'}{2M}, \quad \tau' = \kappa^2 - \lambda'. \tag{3.15}$$

  Thus being the scaling function:

$$f_{RFG}(\psi') = \frac{3}{4}(1-\psi'^2)\Theta(1-\psi'^2), \tag{3.16}$$

  for which it is observed that $f_{RFG}(\psi')$ is restricted in the domain $\psi' \in [-1, 1]$.

- Λ_0 a global factor that contains the relativistic correction D:

$$D = 1 + \frac{1}{2}\xi_F(1+\psi^2), \tag{3.17}$$

$$\Lambda_0 = \frac{\xi_F}{\eta_F^2 \kappa D}. \tag{3.18}$$

- The single nucleon responses U_K, which are essentially the hadronic response factors R_K from the free nucleon case (Eqs.(2.56) to (2.69)), but with extra terms Δ and $\tilde{\Delta}$ accounting for the Fermi motion within the nucleus.

$$\Delta(\lambda,\tau) = \frac{\tau}{\kappa^2}\left\{-\frac{(\lambda-\tau)^2}{\tau} + \xi_F\left[(1+\lambda)(1+\psi) + \frac{\xi_F}{3}(1+\psi^2+\psi^4)\right]\right\}, \tag{3.19}$$

$$\tilde{\Delta} = \frac{1}{\sqrt{\tau(1+\tau)}}\left[\frac{\tau}{\kappa}(1+\lambda) - \sqrt{\tau(\tau+1)} + \frac{\tau}{\kappa}\frac{1}{2}\xi_F(1+\psi^2)\right]. \tag{3.20}$$

The corresponding expressions for the different components from U_K are extensively calculated in the Appendix C from [62].

Starting with the CC contributions, by means of CVC and PCAC hypothesis[19] it is distinguished between conserved ($c.$) and non-conserved ($n.c.$) axial parts:

$$U_{CC} = U_{CC}^{VV} + (U_{CC}^{AA})_{c.} + (U_{CC}^{AA})_{n.c.}, \tag{3.21}$$

$$U_{CC}^{VV} = \frac{\kappa^2}{\tau}\left[(2G_E^V)^2 + \frac{(2G_E^V)^2 + \tau(2G_M^v)^2}{1+\tau}\Delta\right], \tag{3.22}$$

$$(U_{CC}^{AA})_{c.} = \frac{\kappa^2}{\tau}G_A^2\Delta, \tag{3.23}$$

$$(U_{CC}^{AA})_{n.c.} = \frac{\lambda^2}{\tau}(G_A - \tau G_P)^2. \tag{3.24}$$

Regarding CL and LL contributions, CVC hypothesis can be applied as well:

$$U_{CL} = -\frac{\lambda}{\kappa}[U_{CC}^{VV} + (U_{CC}^{AA})_{c.}] + (U_{CL}^{AA})_{n.c.}, \tag{3.25}$$

$$U_{LL} = \frac{\lambda^2}{\kappa^2}[U_{CC}^{VV} + (U_{CC}^{AA})_{c.}] + (U_{LL}^{AA})_{n.c.}, \tag{3.26}$$

$$(U_{CL}^{AA})_{n.c.} = -\frac{\lambda\kappa}{\tau}(G_A - \tau G_P)^2, \tag{3.27}$$

$$(U_{LL}^{AA})_{n.c.} = \frac{\kappa^2}{\tau}(G_A - \tau G_P)^2. \tag{3.28}$$

The transverse components are expressed as follows:

$$U_T = U_T^{VV} + U_T^{AA}, \tag{3.29}$$

$$U_T^{VV} = 2\tau(2G_M^V)^2 + \frac{(2G_E^V)^2 + \tau(2G_M^V)^2}{1+\tau}\Delta, \tag{3.30}$$

$$U_T^{AA} = G_A^2[2(1+\tau) + \Delta], \tag{3.31}$$

$$U_{T'} = 2G_A(2G_M^V)\sqrt{\tau(1+\tau)}[1+\tilde{\Delta}], \tag{3.32}$$

RFG limitations

The RFG model constitutes the basis to introduce the superscaling phenomena in neutrino nucleus scattering. However, this description brings several limitations when analysing experimental data.

[19] Partially conserved axial current, or PCAC, establishes conditions based on chiral symmetry to the axial matrix elements. See [63] for more details.

Regarding the scaling function $f^{QE}_{RFG}(\psi')$, even though it arises from the theoretical calculus, it cannot explain the non-null experimental values in the region $1 \leq |\psi'| \leq 2$. Moreover, it is observed a symmetric behaviour in RFG, whilst data shows an assymmetric long tail in the positive domain of the scaling variable ψ' (see Figure **20** for a comparison regarding electron scattering data). However, these mismatches can be explained by mean of a relativistic mean-field, therefore accounting for FSI and nucleon-nucleon correlations, as studied in [64].

The RFG description provides an universal scaling function, leading to scaling of zero-th kind. However, in Figure **21** the experimental data shows a clear violation of this symmetry, concurring that $f^{QE}_{T}(\psi') > f^{QE}_{L}(\psi')$. Furthermore, it can be checked that the scaling phenomena is present in the whole domain of the longitudinal scaling function, but the scaling is violated in the transversal component for $\psi' > 0$, for which non-QE channels, such as 2p2h or resonances, have important contributions. These observations reinforces the need for an alternative to the universal scaling function, which are palliated later with the description of SuSAv2.

Lastly, RFG formalism leads to a high dependence on the model. This is observed in the parameters k_F and E_{shift}, for which constant values are considered depending on the nucleus species. However, the constant k_F arises from the unrealistic assumption of all initial nucleon momenta below k_F are equally likely. In [65] it is suggested a dependency of E_{shift} with respect the momentum q since a constant value might be too large for low-q values and too small in regions with higher q values. The latter is due to the unaccounted FSI in the assumption of constant E_{shift}.

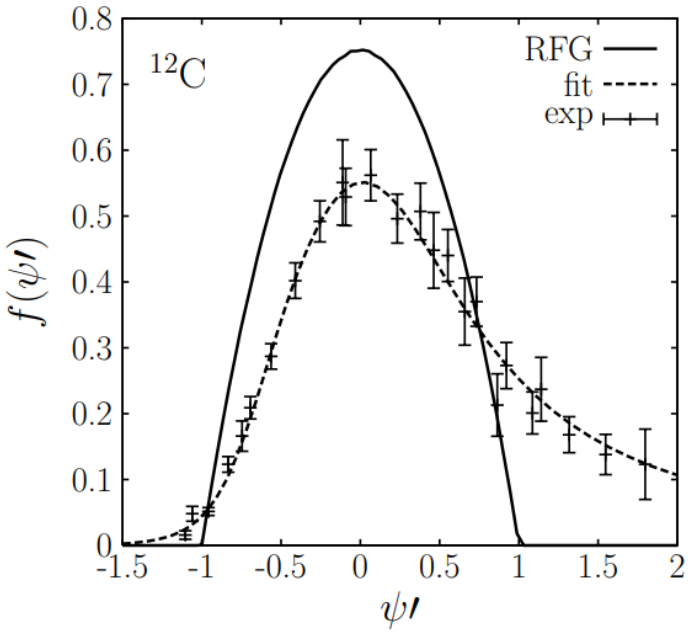

Figure 20: RFG scaling function compared with experimental data in electron scattering with ^{12}C. Figure extracted from [66].

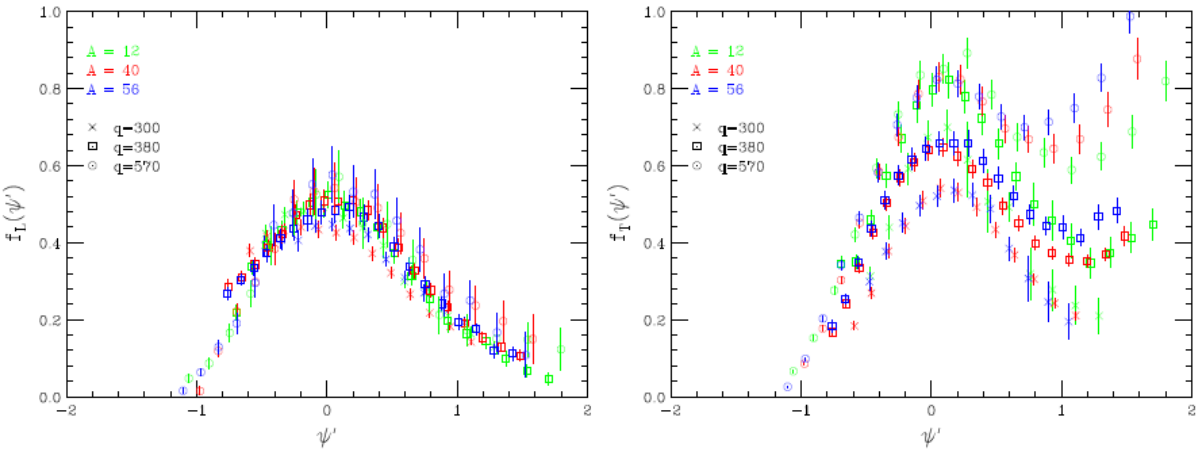

Figure 21: Longitudinal $f_L(\psi')$ (left) and transversal $f_T(\psi')$ (right) scaling functions for different nuclei and for different values of momentum q in units of MeV/c. Figure taken from [52] and data from [67].

3.2.3 Local Fermi Gas (LFG)

Similarly to RFG model, Local Fermi Gas assumes a gas of relativistic nucleons moving within the nuclear field. However, the interaction between nucleons no longer yield radially equal likelihood for initial nucleons, but rather a bump distribution that depends on the radial distance r. This is known as the Local Density Approximation (LDA) and it provides good results when computing nuclear responses in finite size nuclei [55]. Under the same assumption of the initial nucleon momenta being smaller than k_F, now this parameter becomes a decreasing function dependent as well on the radial distance r, as seen in Figure 22.

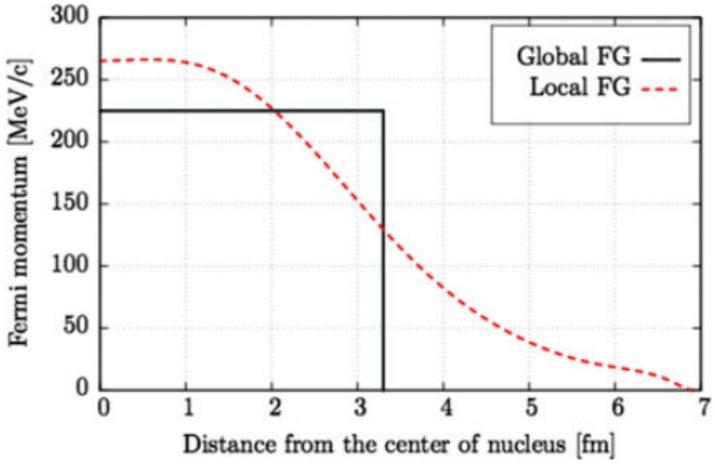

Figure 22: Nucleon distribution versus the distance with respect the center of the nucleons r in LFG and RFG for the given values of $k_F = 225$ MeV/c and $r_{max} = 3.2$ fm [68].

$$k_F(r) = \left(3\pi^2 \frac{\rho(r)}{3}\right)^{1/3}, \tag{3.33}$$

with $\rho(r)$ being the nucleon density[20]. Figure 23 displays how LFG improves the initial nucleons momenta distribution with respect to RFG.

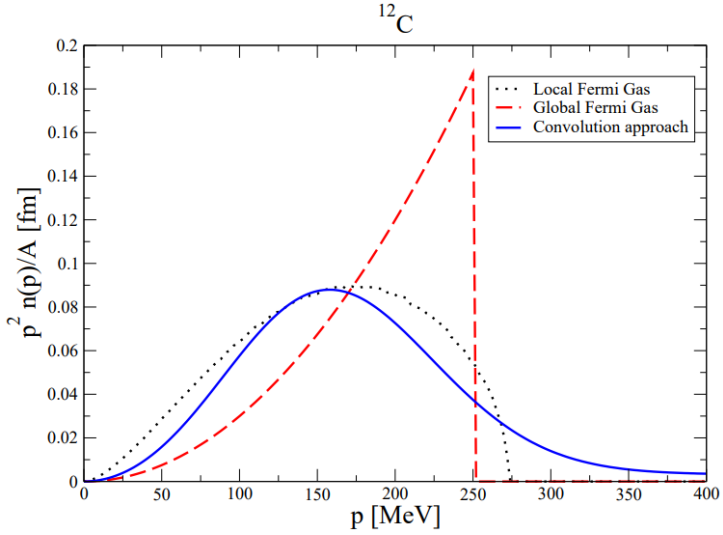

Figure 23: Comparison between RFG (referred as Global Fermi Gas) and LFG models behaviour regarding nucleon density. Figure taken from [69], from which another model which uses convolution is also displayed.

3.2.4 The SuSA and SuSAv2 models

The semi-phenomenological scaling models SuSA and SuSAv2 arise as alternatives to further improve the behaviour found in RFG superscaling, thereby providing a more realistic description in neutrino nucleus scattering. This is achieved by considering experimental (e, e') data (SuSA) and by introducing a blending between RMF and RPWIA formalisms (SuSAv2).

SuperScaling Approach (SuSA)

Initially, several electron-nucleus scattering experiments were analysed under the scaling formalism [59], [60], proving successful predictions from these models. Moreover, in the QE regime, the longitudinal scaling function superscales whilst the transversal does not due to the appearance of non-QE processes for high energies ω. Therefore, the scaling of zero-th kind is violated, leading to an asymmetry in between the scaling functions.

The longitudinal scaling function from (e, e') data however, was thought to be employed as an universal scaling function to predict CCQE reactions in neutrino nucleus scattering,

[20] In [55], it is modelled the nucleon density within the context of a modified harmonic oscillator for light nuclei (A≤16): $\rho(r) = \rho_0 \left[1 + a\left(\frac{r}{R}\right)^2\right] e^{-(r/R)^2}$; or a two-parameter Fermi distribution for heavier nuclei ($A \geq 16$): $\rho(r) = \rho_0/\{1 + e^{[(r-R)/a]}\}$.

known this description as SuSA. This concept was based on the hypothesis that the cross section scales as does in the electron scattering case due to the IA approach.

Hence, the phenomenological SuSA scaling function follows:

$$f_{SuSA}(\psi') \equiv f_L(\psi') = \frac{p_1}{[1 + p_2^2(\Psi' - p_3)^2](1 + e^{p_4\psi'})}, \tag{3.34}$$

with the parameters $p_1 = 2.9883$, $p_2 = 1.9438$, $p_3 = 0.67310$ and $p_4 = -3.8538$ [62].

SuperScaling Approach version 2 (SuSAv2)

Theoretical efforts were put to combine SuSA and the physics from RMF [70] and RPWIA [71] models, thereby originating an extended description of the superscaling known as SuSAv2. This new approach is based on the following assumptions:

1. $f_L^{ee'}$ superscales, as suggested the original model SuSA.

2. $f_T^{ee'}$ superscales for $\psi < 0$, although it can be extended for the whole range if we remove the contributions coming from non-QE channels.

3. RMF reproduces very well the dependence of the scaling function with respect to q at low and medium values[21], leading to a good agreement with $f_{L,exp}^{ee'}$ and the relation $f_T^{ee'} > f_L^{ee'}$ in connection with transverse scaling data..

4. At high q values, scaling function must approach to RPWIA results since FSI effects disappear.

Using the RMF model leads to the employment of three references for scaling functions, yielding naturally to the violation of the scaling of zero-th kind, as previously suggested: transverse ($f_T^{T=1} \equiv f_T$), longitudinal isoscalar ($f_L^{T=0}$) and longitudinal isovector ($f_L^{T=1}$). Note that, in this formalism, $T = 0$ and $T = 1$ refer respectively to isoscalar and isovector components. Introducing RPWIA to satisfy the statement 4 implies the employment of two references scaling functions that are evaluated at $q = 1100$ MeV/c: longitudinal ($\tilde{f}_L^{RPWIA}$) and transversal ($\tilde{f}_T^{RPWIA}$). Moreover, the energy shift appearing in the scaling functions from RMF and RPWIA are dependent of the momentum q, as shown in Figure **24**.

[21] In [65] it is referenced that low and medium values corresponds to set of data below to $q < 800$ MeV/c, while high-q values is considered for $q > 800$ MeV/c.

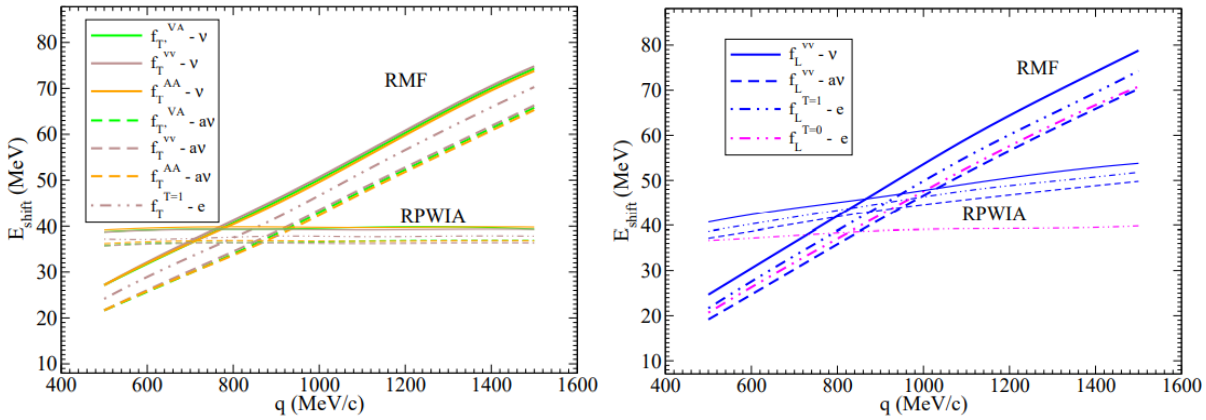

Figure 24: Energy shift evolution with respect q in RMF and RPWIA for different scaling functions. In the legend, e, ν and $a\nu$ correspond to electron, neutrino and antineutrino case respectively. Figure taken from [65].

To combine the scaling functions from both models, we introduce the following expressions (see [65] for more details):

$$\mathcal{F}_L^{T=0,1} \equiv \cos^2\chi(q) f_L^{T=0,1} + \sin^2\chi(q)\tilde{f}_L^{RPWIA}, \tag{3.35}$$

$$\mathcal{F}_T \equiv \cos^2\chi(q) f_T + \sin^2\chi(q)\tilde{f}_T^{RPWIA}, \tag{3.36}$$

where $\chi(q)$ contains the dependence with the momentum q and it is used[22] $q_0 = 800$ MeV/c and $w_0 = 200$ MeV:

$$\chi(q) \equiv \frac{\pi}{2}\left[1 - \left(1 + e^{\frac{q-q_0}{w_0}}\right)^{-1}\right]. \tag{3.37}$$

The nuclear responses in SuSAv2 are described as follows in terms of the previous combination of scaling function and the single nucleon responses in RFG formalism U_K:

$$R_L^{VV,\nu(\bar{\nu})}(q,\omega) = \frac{1}{k_F}\mathcal{F}_L^{T=1}(\psi')U_L^{VV}(q,\omega), \tag{3.38}$$

$$R_{CC}^{AA,\nu(\bar{\nu})}(q,\omega) = \frac{1}{k_F}\mathcal{F}_L^{T=0}(\psi')U_{CC}^{AA}(q,\omega), \tag{3.39}$$

$$R_{CL}^{AA,\nu(\bar{\nu})}(q,\omega) = \frac{1}{k_F}\mathcal{F}_L^{T=1}(\psi')U_{CL}^{AA}(q,\omega), \tag{3.40}$$

$$R_{LL}^{AA,\nu(\bar{\nu})}(q,\omega) = \frac{1}{k_F}\mathcal{F}_L^{T=1}(\psi')U_{LL}^{AA}(q,\omega), \tag{3.41}$$

$$R_T^{\nu(\bar{\nu})} = \frac{1}{k_F}\mathcal{F}_T(\psi')\left[U_T^{VV}(q,\omega) + U_T^{AA}(q,\omega)\right], \tag{3.42}$$

$$R_{T'}^{\nu(\bar{\nu})} = \frac{1}{k_F}\mathcal{F}_T(\psi')U_{T'}^{VA}(q,\omega). \tag{3.43}$$

Overall, SuSAv2 greatly improves the formal description of the nuclear effects, therefore

[22] To clarify the meaning of these parameters, the transition between RMF and RPWIA occurs around q_0 within a region of width w_0.

providing a more realistic model that aligns better[23] to the experimental data, as seen in Figure 25. However, the portrait given in this Section is valid only in the IA representation, thereby processes beyond[24] IA must be added separately within a different formalism.

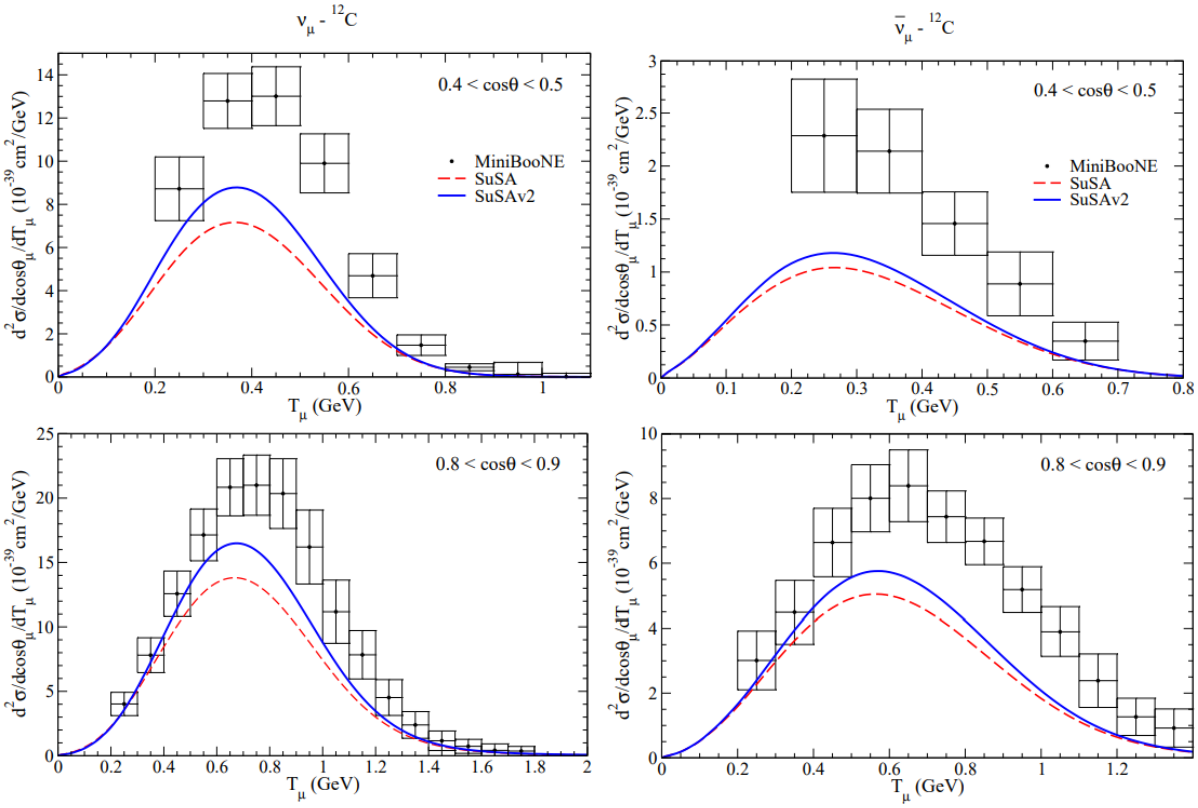

Figure 25: Inclusive cross section in (ν, μ^-) and (ν, μ^+) in the scattering with ^{12}C nuclei. Theoretical predictions from SuSA (red) and SuSAv2 (blue) are compared with the experimental data from MiniBooNE. Figure extracted from [65].

3.2.5 Spectral Function

Spectral Function refers to a semiphenomenological description of the target nuclear information and it is introduced in the denoted Spectral Function $P(\vec{p}, E)$. The latter expresses the probability that the residual nucleus is left with an excitation energy E after removing a nucleon of momentum $\vec{p}$ and it is normalised to the nucleon momenta distribution when integrating over energy and to the unit when integrated over both parameters. This function is modelled by the experimental analysis of semi-inclusive nucleon knock-out in electron scattering and the theoretical calculus of density nuclear matter under the LDA [72], therefore accounting effectively for the short-range nucleon-nucleon correlations. The former can be observed in Figure 26, for which there are non-zero probability of finding

[23] With respect to SuSA, SuSAv2 provides larger cross section. However, as it is studied in Part III, the experimental data represents CC0π processes, therefore missing the inclusion of MEC-2p2h and Pion Absorption channels in the theoretical results.

[24] MEC-2p2h, pion absorption, DIS, etc.

initial nucleons at high momentum values.

$$n(\vec{p}) = \int dE P(\vec{p}, E), \quad \int dE d^3\vec{p} P(\vec{p}, E) = 1. \tag{3.44}$$

Regarding neutrino-nucleus scattering, the formalism can be given by the assumption of nucleons moving as a relativistic Fermi gas within the nucleus and the semi-inclusive cross section is computed within the IA. Similar to SuSAv2, the validity of this spectral function in neutrino scattering is based on the scaling argument from electron scattering to neutrino situation, although strict approximations[25] must be employed to connect the spectral function with the scaling concept, as studied in [73] under the Plane Wave Impulse Approximation. The general scheme to compute the double semi-inclusive cross section is the following:

$$\frac{d\sigma}{dk_l d\Omega} = \int d^3\vec{p} dE P(\vec{p}, E) N \left[\frac{d\sigma}{dk_l d\Omega}\right]_{f.n.}, \tag{3.45}$$

with N the corresponding nucleon number (neutrons for neutrinos and protons for antineutrinos) and the subscript $f.n.$ denoting the free elastic neutrino-nucleon case.

Currently, it has been developed several different spectral function models to use as an input into event generators. Despite providing a formalism based on RFG, spectral functions have also been computed within other descriptions such as Independent Particle Shell Model or even Distorted Wave Impulse Approximation (DWIA) to account for FSI. The formalism of nuclear spectral functions is extensively detailed in the work of Benhar [72], [74].

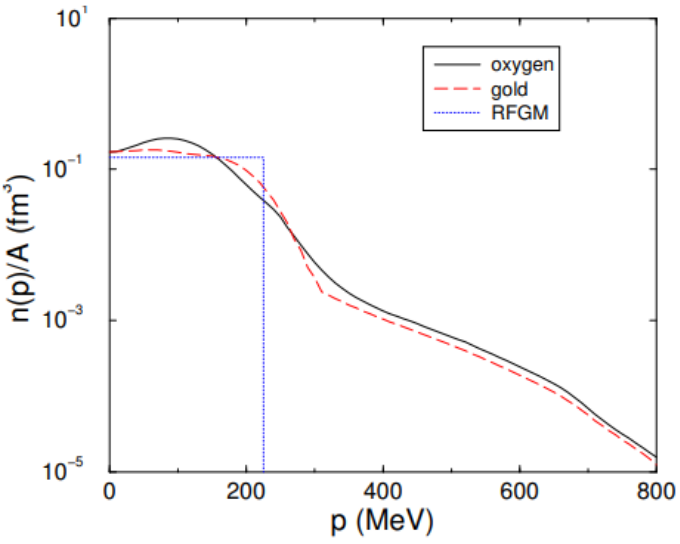

Figure 26: Nucleon momentum distribution normalised to the number of nucleons A. It is compared the results from RFG (denoted as RFGM) and with oxygen and gold by using the corresponding spectral functions. Figure taken from [75].

[25] Notice that for neutrino-nucleus interactions, spectral function models the nucleus information according to electron scattering experimental data.

Part III

Evaluation of Monte Carlo generators performance for T2K ND280 neutrino and antineutrino cross-sections measurements

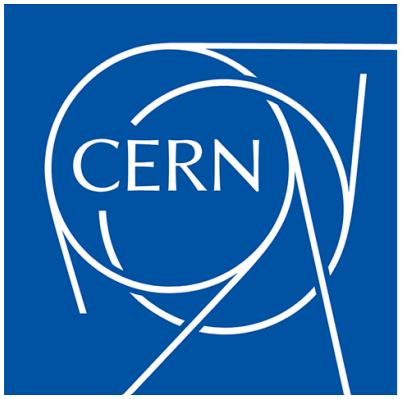

4 Monte Carlo performance in ND280 cross-section measurements

In 2020, the T2K collaboration published experimental data collected from 2009 to 2019 in the near and far detector after a thorough and careful reconstruction of the neutrino events [76]. To summarise, this experiment involves emitting a beam of muon neutrinos or antineutrinos, characterised initially by the near detector, to study neutrino flavour oscillation by measuring the kinematics of the corresponding leptons in the far detector.

This collaboration is crucial in neutrino research because it provides more statistical data to characterise neutrino oscillations.. As explained in Section 1.4, the experimental results of long-baseline experiments such as T2K are essential for not only understanding mass ordering and CP violation but also helping to refine the values in the PNMS matrix, thereby leading to a robust and consistent theory concerning the electroweak interaction.

Among many other analyses with the near detector, the T2K collaboration has published simulatenous measurements of neutrino and antineutrino cross section with ND280, which is available in [77]. These measurements have been compared[26] with various theoretical models to assess the agreement and the performance of the Monte Carlo generators. In this Thesis, we aim to contribute to the same purpose by evaluating the effectiveness of reproducing results from some of the most used neutrino generators in ongoing experiments: NEUT [82] and GENIE [83]. However, only CC0π events will be considered since involving pion production might require extensive descriptions[27] to accurately portray the theory and conduct a proper analysis.

This chapter begins with a brief explanation of the neutrino and antineutrino flux used in T2K for this analysis, which will serve as the input for our Monte Carlo generators. Next, the methodology of the analysis will be thoroughly explained, including the experimental data structure, the different nuclear models we are using and the methods employed to asses the agreement with the T2K data. Finally, the results achieved in this Thesis are presented, providing an in-depth discussion regarding the accuracy of the current performance of Monte Carlo generators. The conclusions has been published recently in Symmetry: [84].

4.1 Neutrino and antineutrino flux

In the employment of Monte Carlo generators for neutrino-nucleus interactions, an incident neutrino or antineutrino flux is needed to predict the outgoing particle kinematics. To that end, it is displayed in Figure **27** the shape of the fluxes used, for both neutrino and antineutrino events. These fluxes are obtained by predicting neutrino events using

[26] To cite some of the T2K studies, [78]–[81].

[27] Resonances (RES), deep inelastic scattering (DIS), ...

FLUKA [85] and GEANT3 [86] simulation models, which involve the interaction of primary beam protons in the T2K target, hadron decay, and muons producing neutrinos. The first T2K study predicting fluxes was published in 2013 [87], detailing the technical simulation methods for estimating the fluxes at both the near and far detectors. Additionally, it explains how the narrow-band beam is achieved by directing the incident flux off-axis by 2.5°, resulting in a peak neutrino energy around 0.6 GeV, for which the oscillation effects are maximal for T2K's baseline of 295 km. Figure **28** illustrates the flux distribution changes with the off-axis angle and the survival probability of muon neutrinos with respect to neutrino energy.

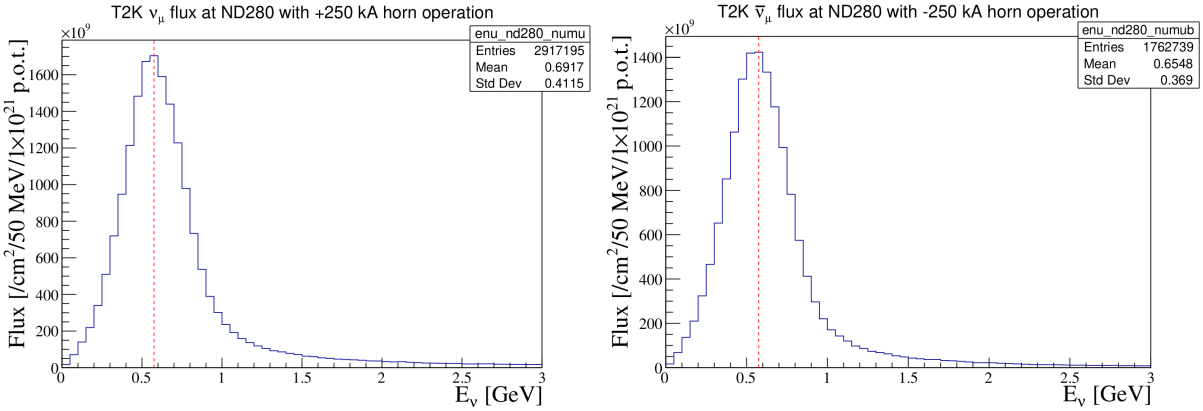

Figure 27: Muon neutrino (left) and antineutrino (right) fluxes predicted as a function of the neutrino energy in the T2K near detector in 2016 with an off-axis set at 2.5° . The peak of the spectra is remarked with a red dashed line, being close to 0.6 GeV.

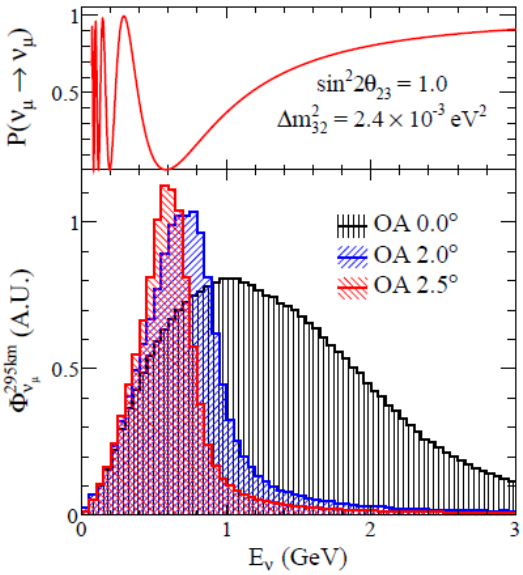

Figure 28: Muon neutrino survival probability at 295 km (top) and neutrino fluxes corresponding to different off-axis angles. As observed, 2.5° achieves a maximum around 0.6 GeV (where the maximum oscillation probability is achieved) while narrowing the spectrum. Figure extracted from [87].

Since 2013, more data in the near detector has been collected and dedicated hadron production experiments were performed, such as NA61 [88], enabling a refinement in the flux simulation. Consequently, this Thesis[28] employs the flux results from 2016 [89], being the experimental data available in the T2K website [90].

4.2 Methodology

To perform a comprehensive analysis of the experimental data, this section aims to explain and justify the procedure employed for the results obtained in Section 4.3.

The first part involves describing the structure of the data. In doing so, it is identified the key elements we are looking for when predicting results. Next, we outline the nuclear dynamics we intend to test using the Monte Carlo generators and detail how these predicted results are obtained. Finally, the statistical analysis procedure is explained, in which two methods are applied to provide a meaningful and complementary discussion on the accuracy of NEUT and GENIE predictions compared to the T2K data.

T2K experimental data structure

The experimental data used in this analysis can be found on the T2K website [90]. It consists of a single ROOT file containing cross-section measurements made at the near detector from the different neutrino and antineutrino interactions with the hydrocarbon nuclei. The data is divided into 9 $\cos\theta$ regions (where θ is the lepton scattering angle) and each region is further subdivided into non-uniform bins that encompass different muon momentum ranges up to 30 GeV (see Table **2**).

Figure **29** displays examples of the double differential cross section with respect the muon momentum p_μ, illustrating how this data appears in a ROOT graph. This format will be maintained for future subsections.

Nuclear models employed in Monte Carlo generators

Monte Carlo generators are utilised to predict results to compare with the ND280 experimental data. This subsection clarifies the different models employed in both NEUT and GENIE[29]. The main goal is to simulate each type of CC0π interaction individually—namely CCQE, MEC, and pion absorption. In this context, note that the term "model" refers to the sum of contributions of these processes under the nuclear dynamics descriptions implemented in the generators. In this Thesis the Monte Carlo cross-section results are weighted over the width of the bin momentum and $\cos\theta$ range (see Appendix D.1).

[28] In the T2K website, it is published newer flux prediction data (2020), corresponding to a better target and more neutrino statistics. Unfortunately, it was tested that NEUT is not compatible yet with this flux version, thereby using 2016 data (check Appendix C.1 for a flux comparison).

[29] An introduction to Monte Carlo generators can be found in Appendix C.

$[\cos\theta_i, \cos\theta_f]$	Number of p bins	Edges (GeV)
[-1.00, 0.20]	1	0,30
[0.20, 0.60]	5	0, 0.3, 0.4, 0.5, 0.6, 30
[0.60, 0.70]	6	0, 0.3, 0.4, 0.5, 0.6, 0.8, 30
[0.70, 0.80]	6	0, 0.3, 0.4, 0.5, 0.6, 0.8, 30
[0.80, 0.85]	7	0, 0.3, 0.4, 0.5, 0.6, 0.7, 1, 30
[0.85, 0.90]	8	0, 0.3, 0.4, 0.5, 0.6, 0.8, 1, 1.5, 30
[0.90, 0.94]	7	0, 0.4, 0.5, 0.6, 0.8, 1.25, 2, 30
[0.94, 0.98]	10	0, 0.4, 0.5, 0.6, 0.8, 1, 1.25, 1.5, 2, 3, 30
[0.98, 1.00]	8	0, 0.5, 0.7, 0.9, 1.25, 2, 3, 5, 30
Total	58	–

Table 2: T2K binning used for this measurement as a function of the different $\cos\theta$ slices and p non-uniform momentum bins up to 30 GeV. Notice how there are more subdivisions in the forward region, which aims to achieve a more refined description with the current resolution of the near detector. There are 58 experimental bins for the whole angular region in both neutrino and antineutrino, resulting in a total of 116 bins.

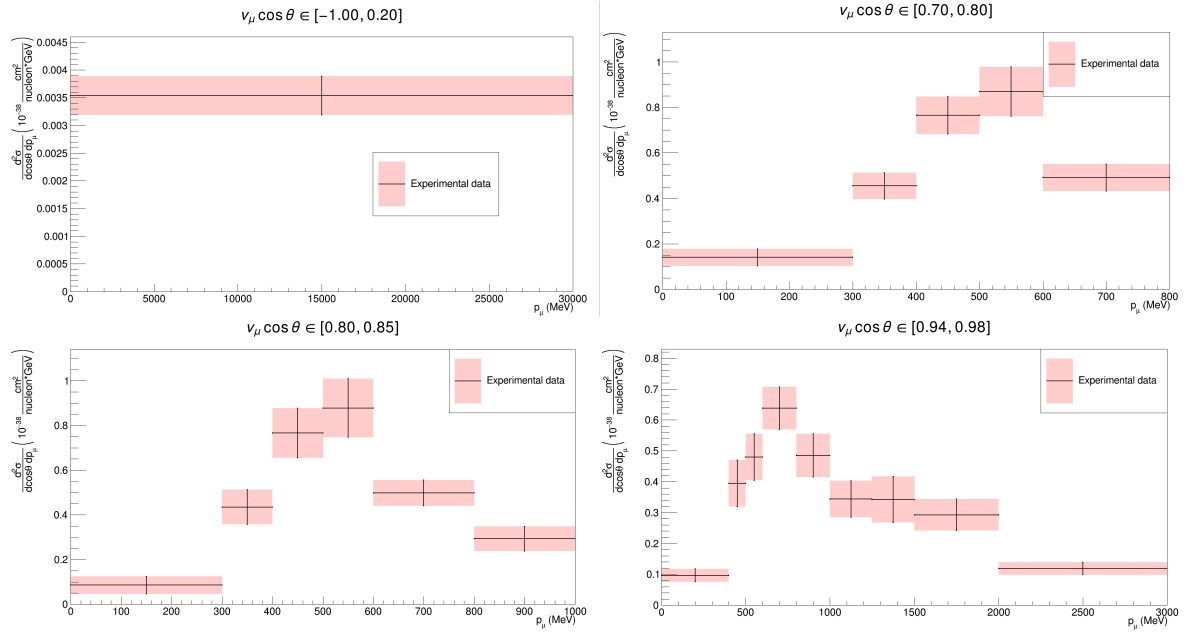

Figure 29: Examples of T2K neutrino cross-section measurements divided into different $\cos\theta$ slices containing non-uniform p bins within. Antineutrino measurements follow the same structure. The pink shading denotes the statistical and systematical uncertainty. More subdivisions, and thereby information, are found in the forward region. Note that the last p bin (the one covering up to 30 GeV) is omitted to ease the reading.

Table 3 displays the models used for the contributions accounted for in this analysis, labeling each combination for future reference. The main difference between models lies

in the CCQE events, as MEC and pion absorption are considered in the SuSAv2-2p2h model and Cascade/Empirical FSI generation respectively due to their effectiveness in prediction and their minor contributions to the overall result. Additionally, the theoretical CCQE frameworks corresponding to SF, LFG, and SuSAv2-QE are thoroughly described in Chapter 3.2.

Model label	CCQE	MEC	Pion Absorption
SF	SF NEUT	SuSAv2-2p2h GENIE	Cascade FSI GENIE
LFG	LFG NEUT	SuSAv2-2p2h GENIE	Cascade FSI GENIE
SuSAv2	SuSAv2-QE NEUT	SuSAv2-2p2h GENIE	Cascade FSI GENIE
DUNE	LFG GENIE	SuSAv2-2p2h GENIE	Empirical FSI GENIE

Table 3: Nuclear model and Monte Carlo generator employed in each CC0π contribution. Each combination is labeled for the future comparison with experimental data in Section 4.3.

Figure **30** shows examples of predicted results. For a sufficiently high number of statistics[30], it is illustrated how the different contributions are weighted with respect to the global result. At low lepton momentum, pion absorption and MEC play significant roles. However, beyond 300-400 MeV, the major contribution rapidly comes from CCQE[31]. Consequently, changing the nuclear description of CCQE is expected to yield different results, enabling a comprehensive comparison of nuclear dynamics.

Methods proposed in the statistical analysis

Once explained the structure of the experimental results and which nuclear dynamics will be accounted for in the Monte Carlo generators, this section aims at describing the procedure used in Section 4.3 to comprehensively discuss the results.

The analysis begins with calculating the values of χ^2 and p-values[32]. This involves a detailed characterisation of these parameters across all nine $\cos\theta$ regions for both neutrinos and antineutrinos. Additionally, to provide a broader discussion, χ^2 and p-values are computed considering:

- All neutrino bins.
- All antineutrino bins.

[30] For all the Figures in Part III containing predicted Monte Carlo results, the number of events simulated is 10^6, which guarantees minimal effects from statistical fluctuation.

[31] Despite displaying examples only for LFG, similar observations hold for the other nuclear models. Generally, CCQE predominates over MEC and pion absorption except at low lepton momentum for small scattering angles, in where the incident neutrino energy is primarily transferred to nuclear effects.

[32] An introduction to these concepts and their calculations in this Thesis can be found in Appendix D.2.

- All data combined.

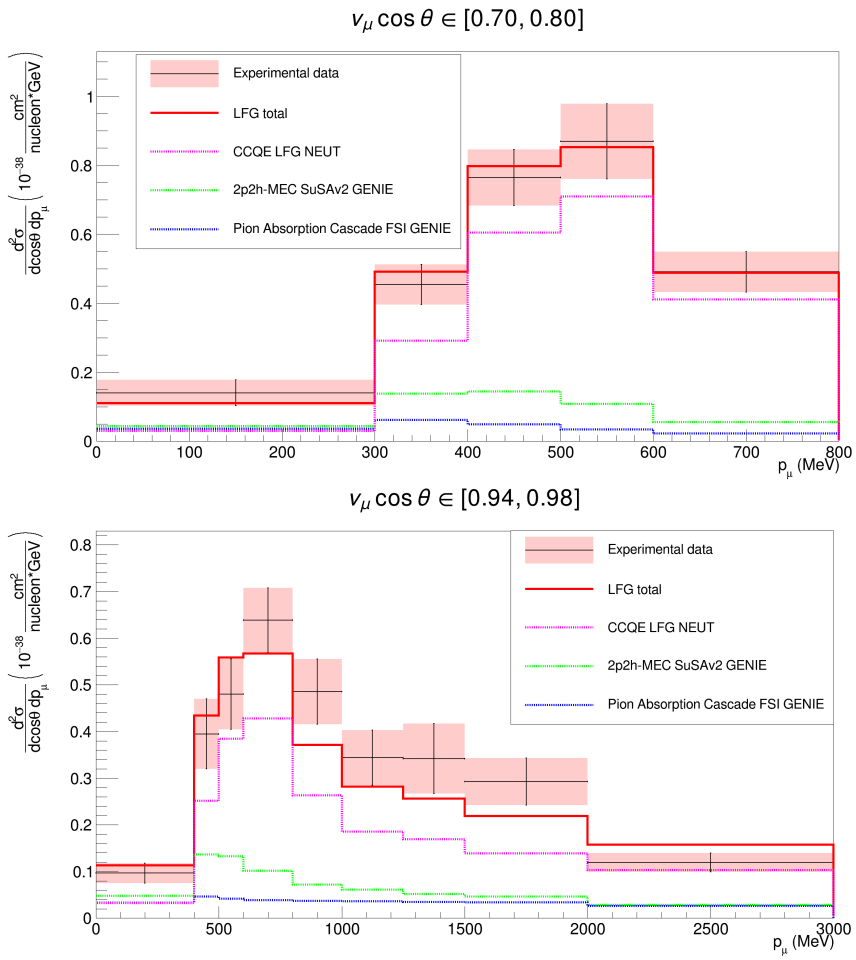

Figure 30: Examples of predicted results compared to experimental data, particularised for the LFG model. Initially, the CCQE, MEC and pion absorption contributions are obtained (dashed lines) and then summed to produce the model used for comparison with the experimental data (continuous line).

According to the publication [78], it is observed that the ND280 systematic uncertainties are higher in the first and last p bins in each angular region (see Figure **31**), due to a low reconstruction efficiency. Therefore, the inclusion of the former bins might not be reliable in the calculation of χ^2. To address this, two methods are proposed for calculating the statistical parameters for the three aforementioned scenarios:

- Method 1: consider all momentum bins.
- Method 2: exclude the first and last momentum bins from each region, therefore reducing their impact on χ^2.

In the angular region [-1.00,0.20], only Method 1 will be applied because there is only one momentum bin ranging from 0 to 30 GeV directly.

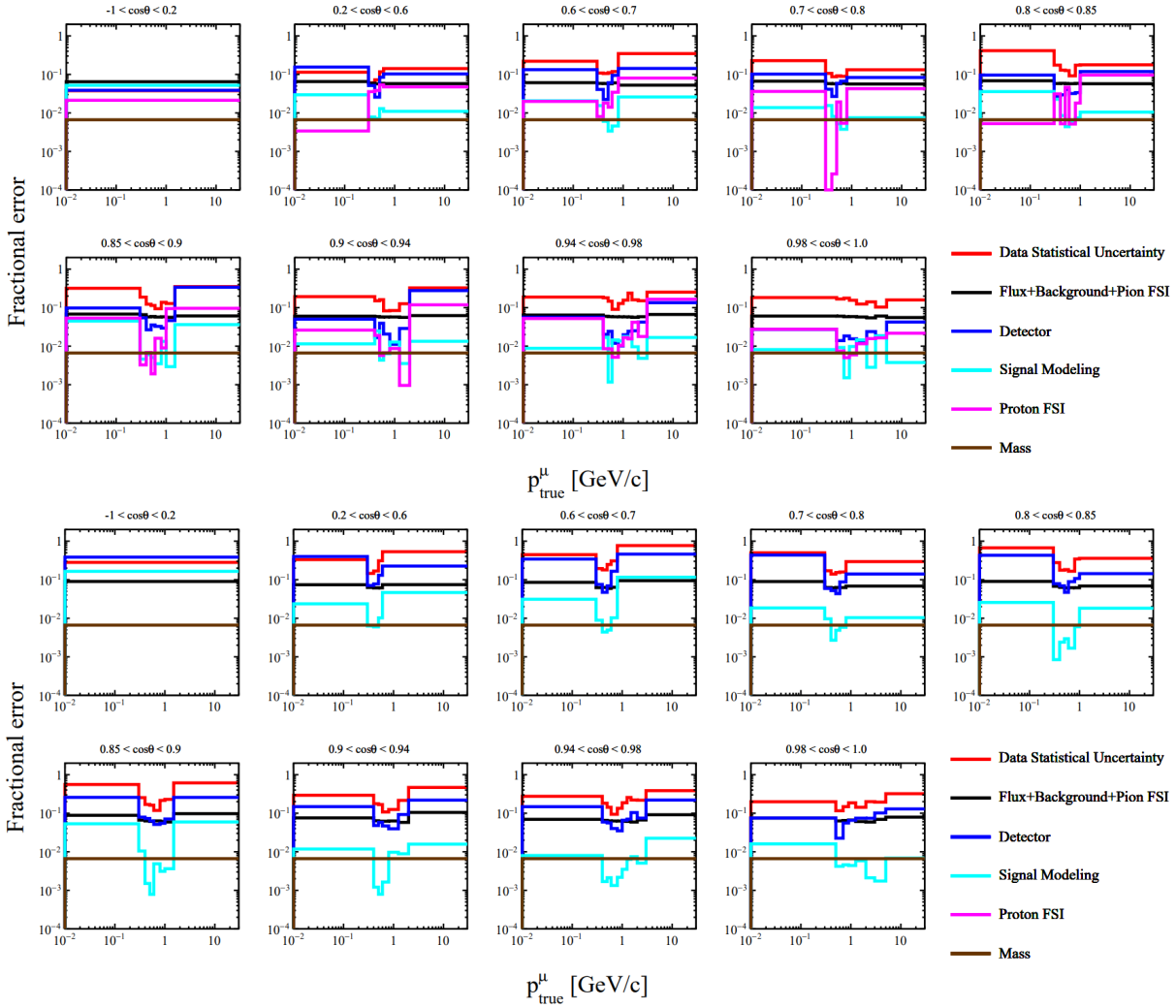

Figure 31: ND280 systematic uncertainties for neutrino (top) and antineutrino (bottom) for the CC0π cross section in each p bin. Notice how the uncertainties are higher in the first and last bins from each angular region. Plots extracted from [78].

4.3 Analysis of the results

This section analyses the predictions of ND280 experimental data from Monte Carlo generators under the four nuclear models labelled previously in Table **3** as SFG, LFG, SuSAv2, and DUNE. Two methods are employed in the calculations: one considering all the p bins, and the other excluding the first and last bins from each $\cos\theta$ interval. A comprehensive analysis is pursued, leading to a two-fold discussion concerning:

1. The goodness of the agreement in each angular region, i.e. in each of the nine interval of $\cos\theta$.

2. The consideration of all neutrino bins, antineutrino bins and the combination of both.

Monte Carlo results have been generated for each angular region, and χ^2 values have

been computed for all considered scenarios. To avoid graphical saturation in the main body of this work, the analysis will focus on the p-values, with the χ^2 results presented in Appendix E.1.

4.3.1 Assessment of the agreement in each angular region

Figure 32 displays the p-values for all nuclear models labeled in Section 4.2, separated by neutrino and antineutrino data. Strong colors represent Method 1 (considering all momentum bins), while pale colors represent Method 2 (excluding the first and last bins in each angular region).

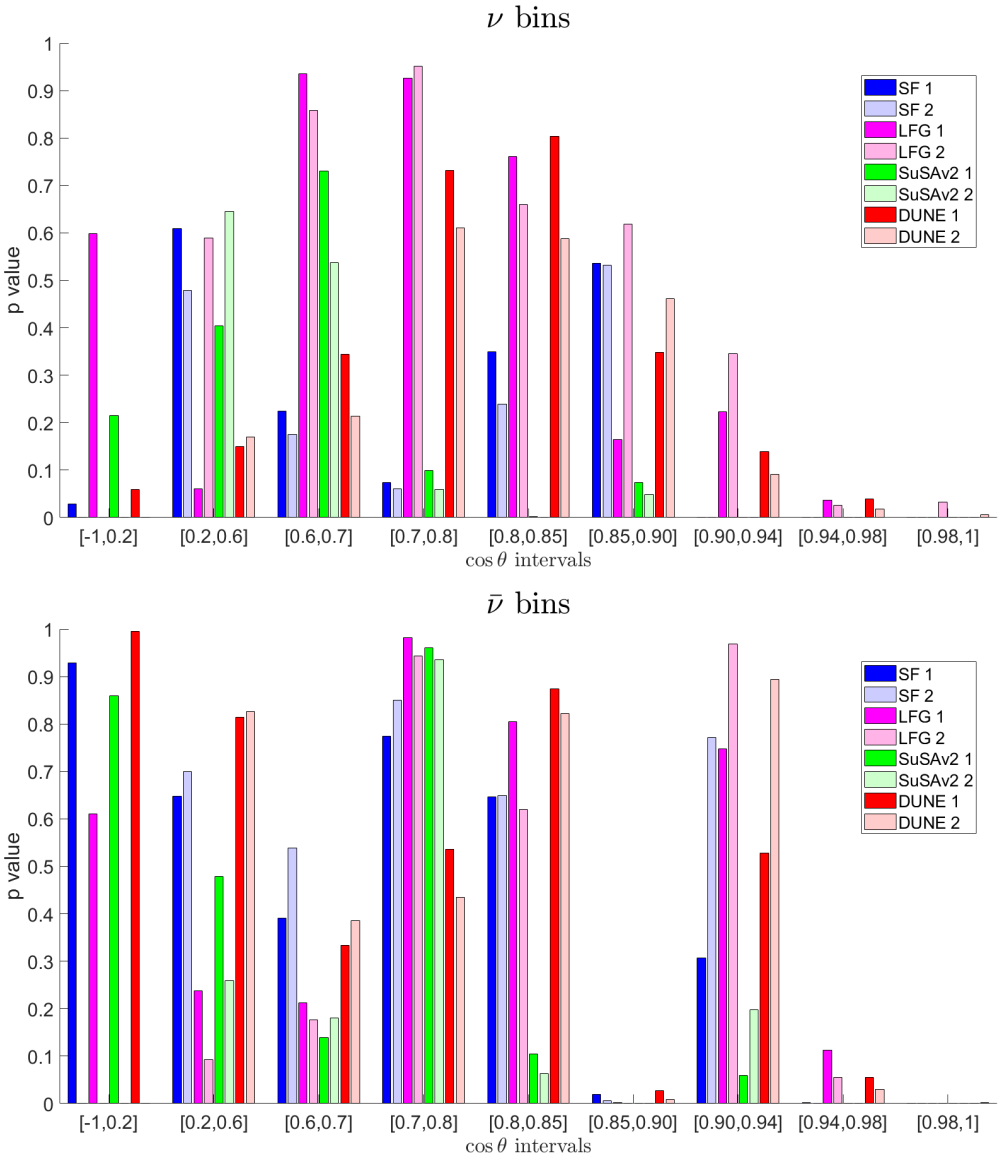

Figure 32: Performance evaluation displaying p-value results of the four Monte Carlo models for all the 9 angular regions. Top (bottom) graph corresponds to neutrino (antineutrino) data. Method 1 and 2 results are represented by strong and pale colors respectively.

The following observations are noted:

- **Poor reproducibility in the forward region**: For both neutrino and antineutrino data, none of the models consistently reproduce the experimental values for small scattering angles. In this region, nuclear effects play a major role, indicating that effects such as those related to the nuclear screening or the influence of the collective potential of the nucleus might be mis-modelled

- **SuSAv2 vs. tuned models**: SuSAv2 aims to be a realistic model by minimizing reliance on tuned parameters, while SF relies more on empirical data, and LFG is based on several assumptions to describe the nuclear field[33], as detailed in Chapter 3.2. Despite this, SuSAv2 shows significant discrepancies with experimental results compared to the other models. SuSAv2-QE is planned for further study with the implementation of resonant models, other nucleon form factors or low-energy nuclear medium effects from RMF theory that are not effectively accounted for yet (see [84]), indicating its great potential in describing neutrino-nucleus interactions.

- **LFG and DUNE**: While DUNE model also employs LFG for QE events, the major difference between them lies in the generator used, leading to different implementations of nuclear effects. In antineutrino data, DUNE shows better agreement in the backward region, while LFG performs better in the forward region.

- **Overestimation of SuSAv2 and SF in the cross section**: Appendix E.1 shows that these two Monte Carlo models overestimate the cross section the most among the models considered, resulting in poorer agreement with repect the experimental measurements as reflected in the p-values. SuSAv2 is expected to improve further theoretically (low-energy nuclear effects from RMF theory might correct the overestimation once implemented in the model), while SF relies on the PWIA approximation. Incorporating DWIA[34] could provide a more accurate description of neutrino-nucleus interactions.

- **Antineutrino vs neutrino agreement**: The four Monte Carlo models better reproduce the antineutrino data compared to the neutrino bins, particularly in the backward and intermediate regions for the $\bar{\nu}_\mu$ case. One potential reason for this could be the $\bar{\nu}_\mu - H$ interaction, which enhances the cross section, especially in the forward region. Also, antineutrino cross section measurements present larger uncertainties. From Appendix E.1, it is observed that for antineutrino data, LFG and DUNE tend to underestimate the experimental results, while SF and SuSAv2 slightly overestimate them. For neutrino data, all four models generally overestimate the data, especially in the forward region.

[33] Nucleon removal energy, Fermi motion, RPA or FSI, among others, are described by the introduction of magnitudes whose values can change from one target to another. See [55] for more details.

[34] See Section 3.2 for a review of PWIA and DWIA in SF formalism.

- **Method 2 efficiency**: Depending on the bin, Method 2 results lead to either higher or lower p-values compared to Method 1, indicating that further work is needed to determine its effectiveness relative to Method 1.

Lastly, during the calculus of χ^2, specific p_μ bins were observed to increase the χ^2 value. A list of these bins is provided in Appendix E.2, representing a complementary observation to the main analysis.

4.3.2 Assessment of the agreement considering all the data

This section aims at discussing the performance of the different nuclear Monte Carlo models in the consideration of the whole dataset rather than angular subsets. As commented in Chapter 4.2, three scenarios are considered: neutrino bins, antineutrino bins and all bins.

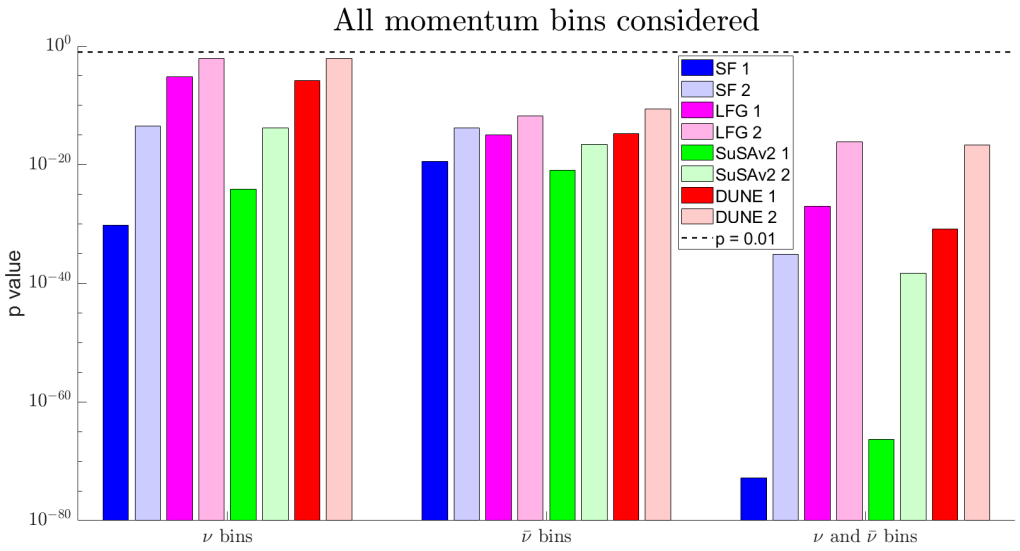

Figure 33: Performance evaluation displaying p-value results of the four Monte Carlo models considering three scenarios: neutrino bins, antineutrino bins and all data points. Method 1 and 2 results are represented by strong and pale colors respectively.

Figure 33 displays the p-values, where strong (pale) colors represent Method 1 (2). A reference for $p = 0.01$ is introduced to facilitate the comparison with the Monte Carlo results, leading to the rejection of all models for the considered scenarios. However, we list the following observations:

- **Method 2 efficiency**: The exclusion of the first and last p bin in each angular region significantly increases the p-value, particularly when considering the entire dataset. This confirms that the uncertainties found in these regions play a relevant role in the Monte Carlo agreement with the data.
- **Neutrinos vs antineutrinos data**: LFG and DUNE perform better with neutrino bins, whereas SuSAv2 and SF p-values increase with antineutrino data. While the

latter is expected from the previous analysis, LFG and DUNE results are noteworthy as Figure 32 showed these models reproduced better in the antineutrino high-angle kinematics.

4.3.3 Conclusions of the analysis

The main objective of this section is to evaluate the agreement of Monte Carlo simulations using GENIE and NEUT from SF, LFG, SuSAv2 and DUNE models with the T2K ND280 experimental data. To achieve this, χ^2 and p-values were calculated for each angular region and for the entire dataset, considering both the inclusion and exclusion of the first and last p bins from each $\cos\theta$ interval. While only p-values are presented here, a graphical comparison of predicted results and their corresponding χ^2 values is available in Appendix E.1.

Overall, none of the four models consistently reproduce the cross section, leading to their rejection when considering the entire dataset.

Regarding performance in each angular interval, the models better describe backward kinematics, particularly for antineutrinos, but fail to agree in the forward region where nuclear effects are more significant. This suggests that the former are not effectively reproduced in the four Monte Carlo models. The following potential reasons are identified:

- **DUNE and LFG**: The primary difference lies in the generator used for QE events (NEUT for LFG and GENIE for DUNE), leading to similar results for both models. The disagreement in the forward region might indicate that RPA and FSI are not modeled realistically, especially for antineutrinos.
- **SF**: SF relies on PWIA, a simplistic approach where FSI do not have an impact on the outgoing lepton kinematics. Additional features in NEUT could incorporate improvements to better replicate nuclear effects, for example, to Pauli Blocking. These observations might justify the model's poor agreement at small angles.
- **SuSAv2**: Despite achieving the lowest p-values among the four models, SuSAv2 aims to be a realistic approach while minimising reliance on tuned parameters. SuSAv2-QE is planned for further theoretical refinement with the inclusion of low-energy nuclear medium effects and resonance models [84].

Additionally, when considering the entire dataset, LFG and DUNE show better agreement with the neutrino case. Further research is required to justify this observation.

As expected, the inclusion of the first and last bins in each angular region significantly increases the disagreement, noticed especially when considering the entire dataset. Furthermore, more bins overestimating χ^2 were found at intermediate energies, where the efficiency should be best according to [78]. However, as there is no clear justification,

they are noted as observations in Appendix E.2.

These results are crucial in assessing the current performance of Monte Carlo generators in simulating neutrino-nucleus interactions. While nuclear effects are not yet effectively accounted for, advancements are expected with the forthcoming ND280 upgrade. The current T2K near detector configuration leads to systematic errors in neutrino oscillation parameter measurements, estimated at approximately 6%. However, the upgrade will reduce these errors to around 4% by reducing uncertainties in the main systematic parameters, as depicted in Figure **34**. Two high-angle Time Projection Chambers (TPCs) and the Super Fine-Grained Detector (SuperFGD) will be incorporated in the experimental setup [91] (see Figure **35**) to provide a full angular coverage of the detector, facilitating finer resolution in high-angle regions. Ultimately, ongoing efforts in long-baseline experiments aim at more measurements and better precision to accurately determine neutrino oscillation parameters in the near future.

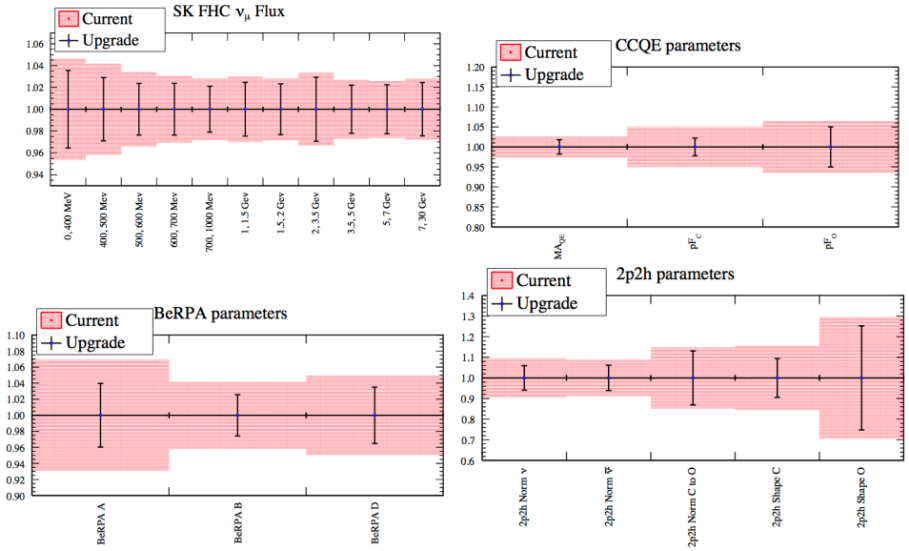

Figure 34: Error of the main systematic parameters for the ND280 upgrade (black lines) compared to the current configuration (red bars). With the ND280 upgrade, an overall reduction of systematic uncertainties by 30% is expected. More details on these uncertainties can be found in [92], from where this figure is extracted.

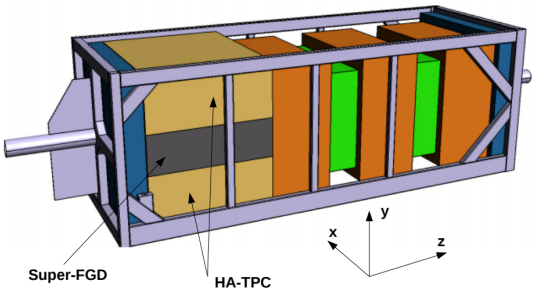

Figure 35: 3D model of the ND280 upgrade, highlighting the two high-angle TPCs and the SuperFGD detector. Figure extracted from [92].

Part IV

ENUBET monitored neutrino beam optimisation for next-generation of long-baseline experiments

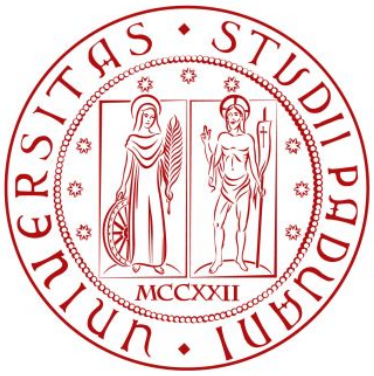

UNIVERSITÀ
DEGLI STUDI
DI PADOVA

5 ENUBET goals

The goal of ENUBET is to provide the first monitored neutrino beam, in which the neutrino flux is known with a precision of $\mathcal{O}(1\%)$, i.e. about one order of magnitude better than the current state of the art. Such a beam would allow a high precision neutrino cross section determination that can significantly enhance the discovery potential of the next generations of long-baseline experiments (such as Hyper-Kamiokande and DUNE), by reducing one of the main source of systematic uncertainties.

Chapter 5 delves on a detailed explanation of this experiment to understand its importance towards future neutrino experiments. A description of the experimental setup is given, being crucial for understanding the beam optimisation process performed via Geant4 simulations in Chapter 6.

5.1 Overview and context of ENUBET

In the last 50 years, detectors used in long-baseline neutrino experiments have improved in terms of resolution and complexity. However, advancements in beam technology have primarily focused on increasing intensity by several orders of magnitude. The ongoing research in this field aims to further reduce systematic uncertainties and enhance the control of the intensity.

The Enhanced NeUtrino BEam from kaon Tagging (ENUBET [93]) is an international project designed to produce intense beams of electron and muon neutrinos from the decay of positively charged kaons (K^+) and pions (π^+). Kaons have a rest mass of 493.667 MeV/c and a decay time of 12.38 ns, while pions have a rest mass of 139.570 MeV and a decay time of 26 ns. The project focuses[35] on the kaon decay modes that produce antimuons and positrons, resulting in muon and electron neutrinos: K_{e3}, K_{e2} and $K_{\mu 2}$ (see Eq.(5.1)).

$$K_{\mu 2} : K^+ \to \mu^+ \nu_\mu, \quad K_{\mu 3} : K^+ \to \mu^+ \nu_\tau^0, \quad K_{e3} : K^+ \to e^+ \pi^0 \nu_e, \tag{5.1}$$

ENUBET would be the first monitored neutrino beam, where the neutrino flux is reconstructed using the lepton rates from the instrumented decay region. The primary concept involves measuring the decay products in a long tunnel whose walls are instrumented with a sampling calorimeter (tagger), allowing the neutrinos to be characterised through the detection of positrons and antimuons (see Figure **36**). Conversely, the antineutrino beam can be achieved by collecting the corresponding muon and electron from the K^- decay modes.

[35] Muon neutrinos can be obtained by pion decay ($\pi^+ \to \mu^+ + \nu_\mu$.). However, it is not likely that the resulting antimuon hit the calorimeter due to its small deviation angle. Nonetheless, ENUBET is working to incorporate instrumentation in the forward region to be able to monitor these neutrinos in the future.

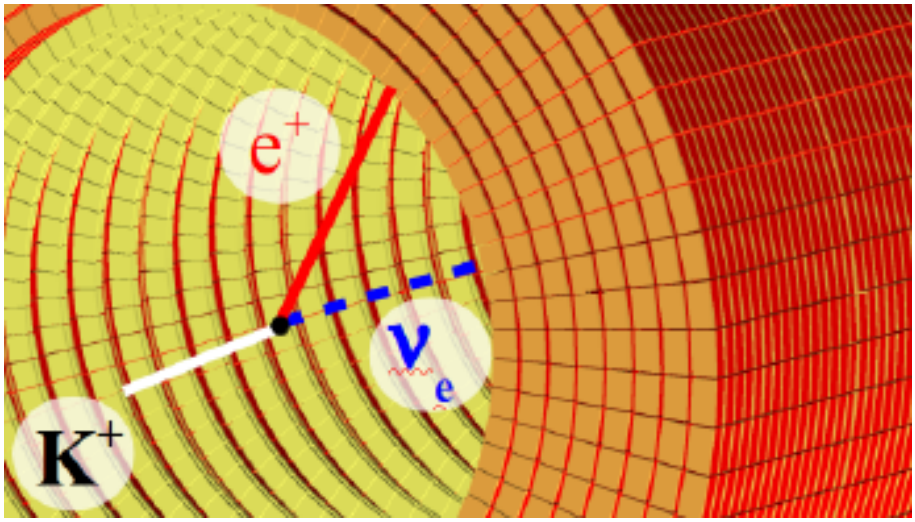

Figure 36: Event detection inside the tunnel decay accounting for the production of a neutrino by gathering the positron in the calorimeter [94].

History of ENUBET

The ENUBET collaboration began in 2015. The project was approved by the European Research Council as ENUBET ERC, running from 2016 to 2022 and hosted by the University of Padova and INFN. It provided the first monitored neutrino beam simulation by detecting large-angle positrons[36] in the decay tunnel. The goal was to create an electron neutrino source with a flux measured to better than 1% accuracy at the GeV level. The simulation results (see Figure **37**) demonstrates the ENUBET potential for a significant reduction in neutrino flux uncertainty compared to present experimental results.

The project is also hosted at CERN Neutrino Platform (NP06), expanding the detection to include muon neutrinos from the decay of kaons and pions[37]. Figures **38** and **39** show the number of current-charged neutrino interactions normalised to 1 pot (proton on target) produced in different parts of ENUBET, with the red spectrum representing the ones arising from neutrinos generated in the decay tunnel, the region of interest. Pions and kaons produce neutrino energies greater and less than 4 GeV respectively, resulting in two distinct neutrino populations in the energy spectra. ENUBET aims to measure both populations in the decay tunnel, but currently the latter component is the one that was better studied due to its larger acceptance in the experiment.

[36]Positrons from kaon decay deviate more than those from muons ($\mu^+ \to e^+ + \nu_e + \bar{\nu}_\mu$). For a parent meson of 8.5 GeV, the mean positron angles are 88 mrad and 25 mrad, respectively.

[37]Pions provide less energetic neutrinos and more forward muons than kaons. The current ENUBET setup is inefficient at detecting this muon population, but efforts are underway to improve instrumentation after the tagger to account for forward muons in NP06.

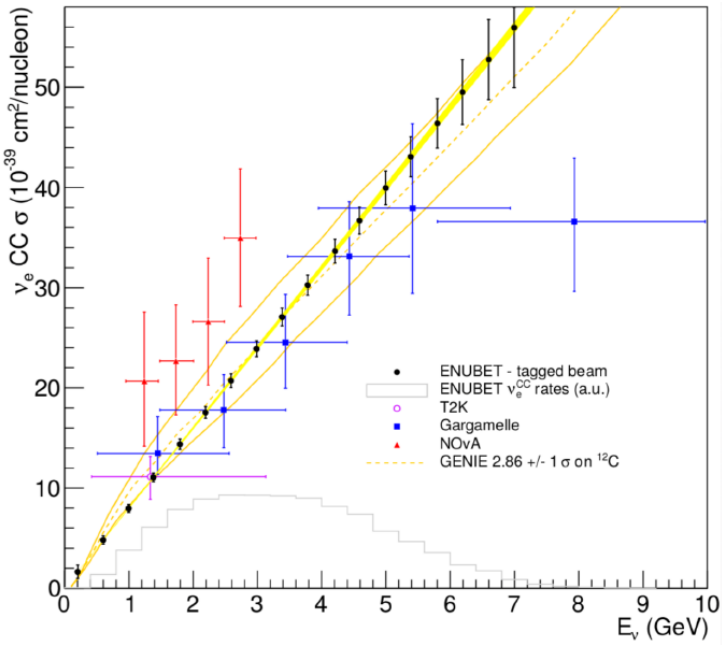

Figure 37: Simulation ν_e charged-current cross section results potentially considering 10^4 events in ENUBET (black dots) with respect to the experimental results from T2K, NOνA and Gargamelle. Simulation with GENIE has been shown for comparison and in grey it is displayed the energy flux distribution. Figure taken from [95].

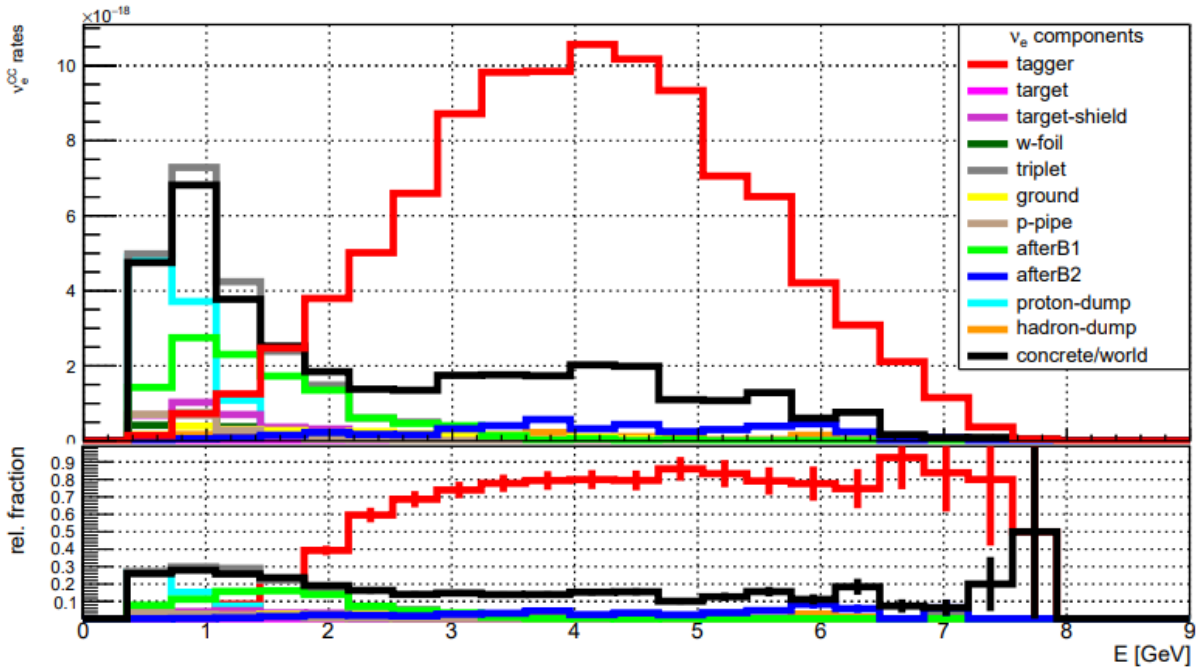

Figure 38: Top: Total energy spectra of ν_e detected via charged-current interactions and normalised to 1 pot [96]. The red line shows neutrinos that have been produced within the decay tunnel, which is the region of interest for ENUBET. Bottom: fraction of each spectrum relative to the total of ν_e^{CC} interactions.

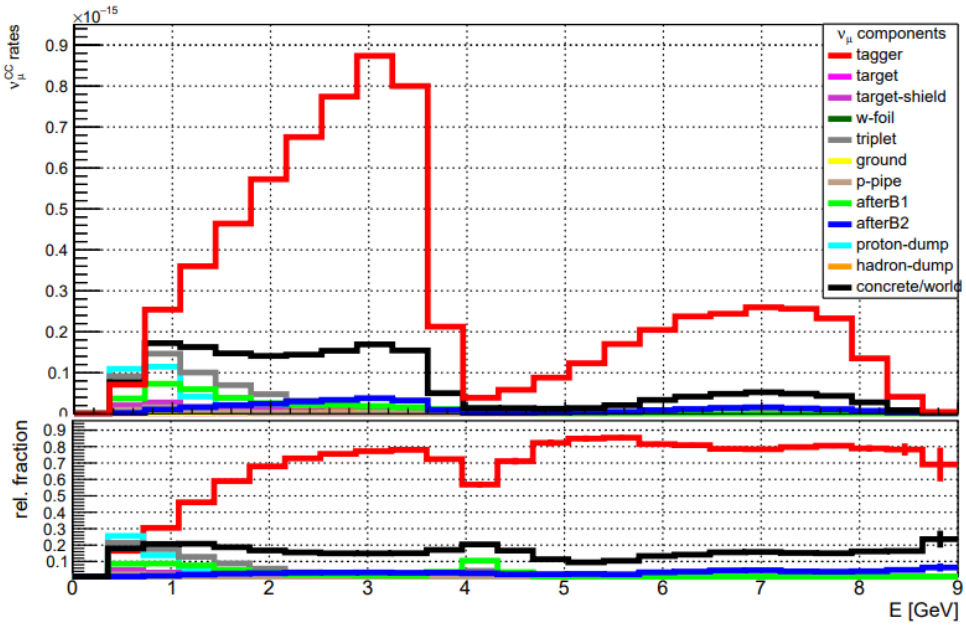

Figure 39: Top: Total energy spectra of ν_μ detected via charged-current interactions and normalised to 1 pot [96]. The red line shows neutrinos that have been produced within the decay tunnel, which is the region of interest for ENUBET. Bottom: fraction of each spectrum relative to the total of ν_μ^{CC} interactions. Notice two populations in both plots: lower energy spectra from pions decay ($E_{\mu_\nu} < 4$ GeV) and higher energy spectra from kaons decay ($E_{\mu_\nu} > 4$ GeV).

The tunnel instrumentation has been tested with different prototypes during 2016-2018 [97]–[99]. A large scale demonstrator of the ENUBET tunnel instrumentation was built at INFN-LNL labs and tested at CERN PS East Hall in August 2023 and 2024 [100]. The simulations show that the goal of less than 1% precision on the neutrino flux using the monitoring technique is achievable.

Current status

Figure 40 presents a Geant4 simulation[38], displaying the particle distribution in ppot (particle per proton on target) entering the decay tunnel with the current ENUBET setup (tlr6v6). The collaboration's next steps focus on optimising the beamline.

The tagger is designed to detect μ^+ and e^+ from the decays of K^+ within the decay region (40 meters). Currently, ENUBET is designed to produce neutrinos from parent mesons around 8.5 GeV. As shown in Figure 39, accurate inclusion of μ from π^+ decay can further enhance the neutrino monitoring capabilities of ENUBET.

The goal of ENUBET is to suppress the beam halo background and to have almost only decay products hitting the target, ensuring an effective detection of antimuons and

[38]The results shown in Figures 40, 41, and those in Chapter 6, correspond to a small part of the beam simulation. However, the statistics are sufficient for an effective analysis, as detailed in Appendix B.1.

positrons to accurately measure the neutrino flux, while retaining at the same time a large enough meson flux for an intense neutrino beam. Figure 41 shows particles hitting the calorimeter detectors in the tunnel[39] in the reference ENUBET setup.

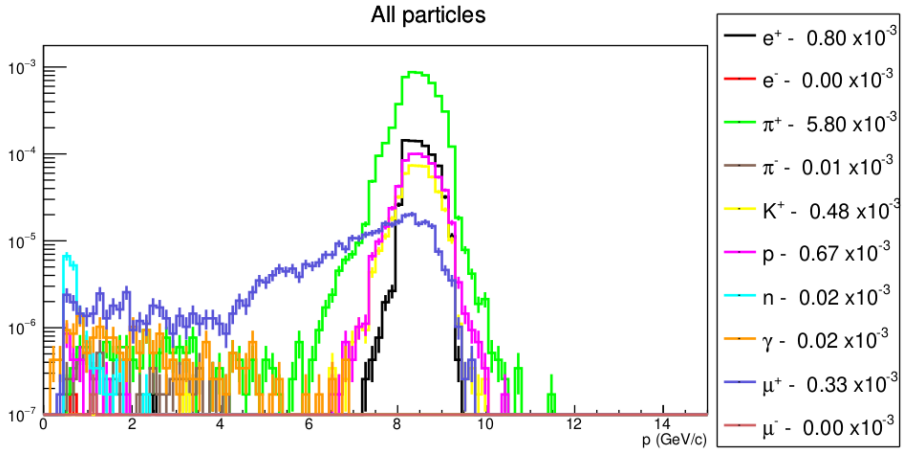

Figure 40: Geant4 distribution of particles in ppot entering in the tunnel decay with the current ENUBET experimental setup. This Thesis aims at increasing the kaons/pions (yellow/green spectrum) whilst reducing other contributions, such as e^+ (black lines).

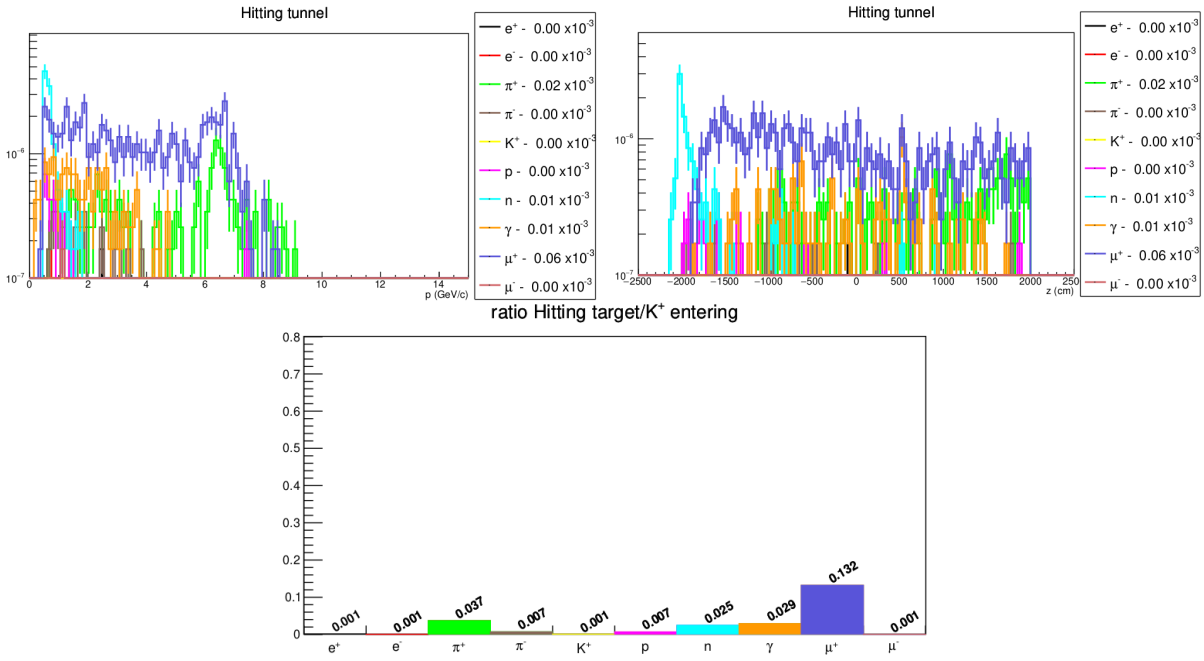

Figure 41: Top left: particle distribution in ppot that hits the calorimeter detectors inside the tunnel with respect to the momentum. Top right: the same as the former as a function of the impact point along the tagger. Bottom: ratio of particles that hit the detector with normalised to the number of kaons entering in the tunnel. All plots are Geant4 simulations results.

[39]In this Thesis work, it is denoted as "ratio" the amount of particles hitting the calorimeter per kaon entering in the tagger. As an example, positron ratio means e^+/K^+ (positrons hitting the detectors divided by kaons entering in the tagger).

This Thesis aims to optimise the beamline in Geant4, with two main objectives for ENUBET:

1. Maximise the number of kaons and pions in the tagger per proton.
2. Minimise the number of entering particles hitting the tagger, thus reducing their impact on the detectors.

Future developments

ENUBET has just finished in August 2024 to collect data from a reduced setup to determine the calorimeter response. The next steps involves incorporating these results in the simulation and pursuing detailed accelerator, engineering and radioprotection studies to eventually build the physical setup in CERN in the following years.

It is estimated that a total of 10^4 ν_e^{CC} events at the far detector (500 ton mass, 6x6 m^2 transverse dimensions) with a 400 GeV proton beam can be collected in 2-3 years of data collection. ENUBET, capable of covering neutrino energies in the GeV scale, promises to significantly reduce cross section related systematics, fulfilling for instance the needs of DUNE and Hyper-K. This achievement can be complemented by a reduction in systematics with nuSTORM [101]. Further details on the implementation of the ENUBET results in future long-baseline collaborations can be found in [102].

The development of an instrumented hadron dump, to monitor forward muons, is part of the PIMENT project (PIcosecond MEga for ENubeT [103]). A prototype is scheduled for testing at CERN North Area by 2024, which will enable ENUBET to extend its physics potential to ν_μ from pions.

Additionally, ENUBET is currently studying the possibility to be employed in the context of the proposed ESSνSB experiment, which focuses on the interaction of lower energy neutrinos. Thus, ENUBET final setup is expected to be adapted for different energy ranges in the GeV region.

5.2 Experimental setup

In ENUBET, when the proton beam hits the target, a cascade of particles is produced and then guided and filtered until they reach the decay tunnel. The goal is to reduce as much as possible the amount of entering particles colliding with the tagger detectors after the filtering process, so an accurate neutrino beam can be achieved, later on detected by a 500-ton neutrino detector with similar dimensions to protoDUNE-SP or protoDUNE-DP at CERN [104]. Understanding how these filters work is crucial for optimising the system, as discussed in Chapter 6. This section provides a detailed explanation of ENUBET's experimental setup by systematically describing each component shown in Figure **42**.

The ENUBET beamline is implemented in G4Beamline, GEANT4, and FLUKA simulations.

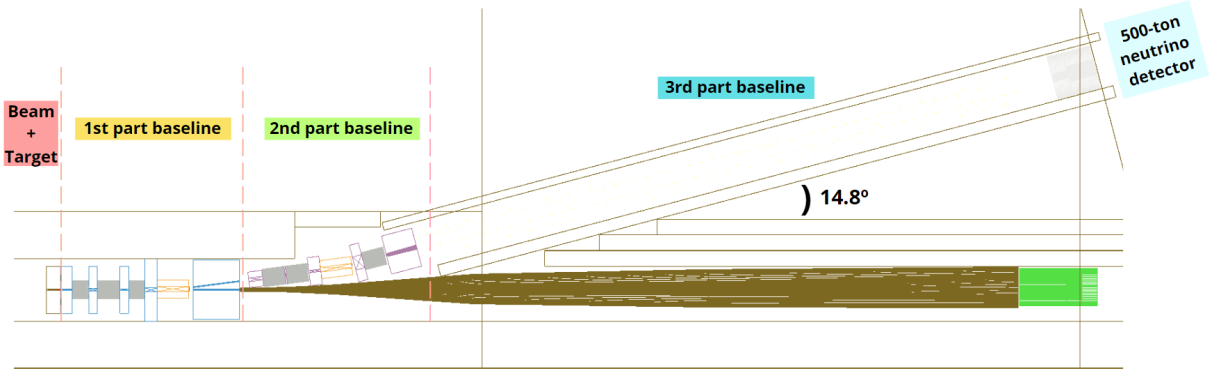

Figure 42: Experimental setup of ENUBET tlr6v6 visualised in Geant4.

Beam and target

In current experiments like T2K or NOνA, a fast-extraction beam of primary protons is typically used for the neutrino source. However, for ENUBET, a slow resonant extraction of protons is envisaged in order to cope with pile up in the tagger. The CERN SuperSynchrotron (SPS) supplies a proton beam at 400 GeV with a spill duration of 4.8 seconds and an intensity of 4.5×10^{13} protons per spill. Detailed studies on the beam production process can be found in [105].

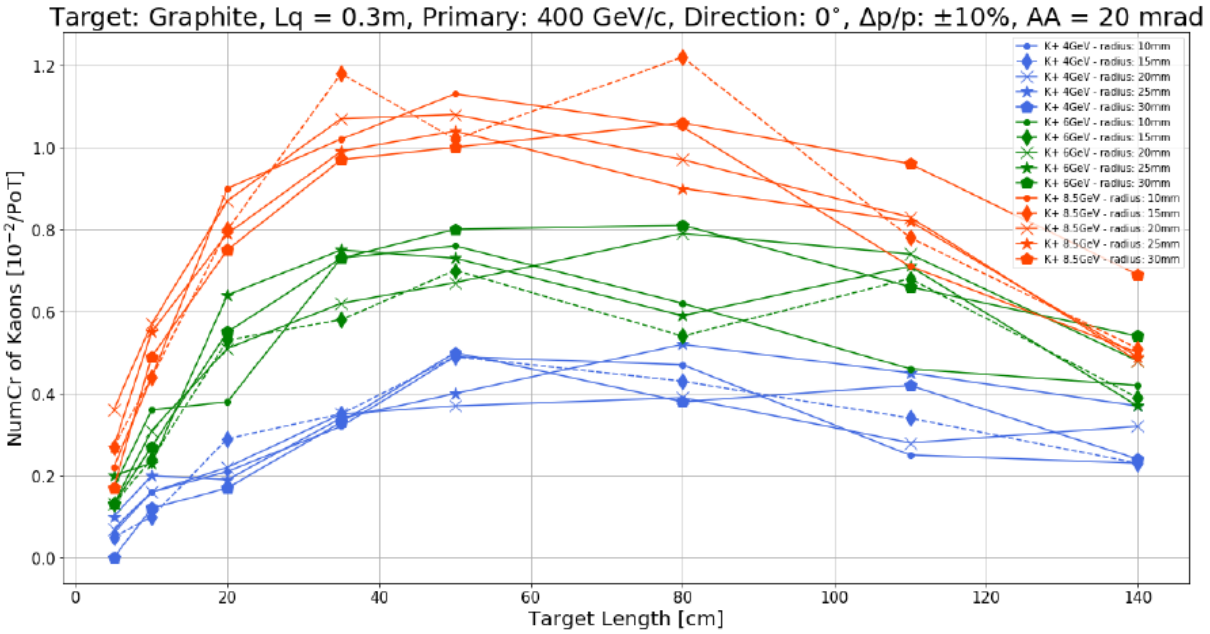

Figure 43: Kaon yielding for a 400 GeV/c proton beam as a function of the graphite target length for different radius (marker shapes) and different kaon momentum (colors). Data is collected within a relative momentum uncertainty of 10% and ±20 mrad angular acceptance in 30 cm after the target. Error bars are not plotted to ease the reading [100].

Regarding the target material, graphite, beryllium, and Inconel-718[40] have been investigated for their suitability in ENUBET. Graphite has shown superior kaon yield compared to the others, aligning with its selection for high-power pion-enriched beams. To optimise the target dimensions, prototypes have been modeled as cylinders with varying lengths (1-140 mm) and radii (10-30 mm). FLUKA simulations (see Figure **43**) indicate that a length of 70 cm and a radius of 30 mm maximise kaon yield at 8.5 GeV within an angular acceptance of ±20 mrad.

First part of baseline

Figure **44** illustrates the initial segment of the ENUBET beamline. Following the collisions with the target, the particles transverse a tungsten plate (W plate), primarly designed to suppress the amount of positrons reaching the decay tunnel walls. Next, the particles pass through a triplet of quadrupoles (Q1, Q2, and Q3), where they are focused differently based on their velocity[41] v.

Between the quadrupoles, copper shields (Sh1, Sh2, Sh3, and Sh4) are positioned to absorb undesired products. Beyond Sh4, the particles are deflected by a dipole (D1), with the bending angle determined by the particle momentum-to-charge ratio, p/Z. Following this, a copper block (Cu block) allows two paths: one for positively charged particles with a momentum near 8.5 GeV, and another for non-charged particles and high-energy protons (primarily non-interacting protons from the primary beam), towards the proton dump.

Second part of baseline

After bending in D1, the beam proceeds through a quadrupole doublet (Q4 and Q5) to converge into the dipole D2. The trajectory is then curved toward the decay tunnel with a total bending of 14.8° with respect to the primary proton line. Along this path, it passes through quadrupole Q6 and a tungsten block ("W block") designed to filter out undesired particles, primarily pions, positrons and muons originating from interactions and early decays of K^+ and π^+ in the upstream part of the beamline. The aperture within the W block is sufficient to allow particles around 8.5 GeV to pass through.

Tungsten shields (Sh5, Sh6, Sh7, and Sh8) are also placed between these components to absorb off-momentum particles, as observed in Figure **45**.

Third part of baseline

Finally, the 40-meter decay tunnel (tagger) is reached, where kaons and pions decay, emitting corresponding neutrinos (see Figure **46**). At the end of the tunnel, a hadron dump is positioned to absorb all particles that can decay afterwards in neutrinos (primarily kaons,

[40] Alloy composed majorly by nickel and chromium.

[41] Quadrupoles exert Lorentz forces on particles, expressed as $\vec{F} = q(\vec{E} + \vec{v} \times \vec{B})$, where q and $\vec{v}$ denote the charge and velocity of the particle, and $\vec{E}$ and $\vec{B}$ are the electric and magnetic fields within the quadrupole.

muons and pions), thus ensuring more control over the neutrino beam.

Within the tunnel walls, iron-scintillator sampling calorimeters are embedded and longitudinally segmented into modules, facilitating the identification of charged leptons and the measurement of their energies. The kaon beam, centered at 8.5 GeV, produces charged leptons with large emission angles, often hitting the tunnel walls. The collection of the decay products from K^+, particularly e^+ and μ^+, is essential in monitoring the neutrino beam, as shown previously in Figure **36**. Detailed insights into particle identification using calorimeters in ENUBET are discussed in [96].

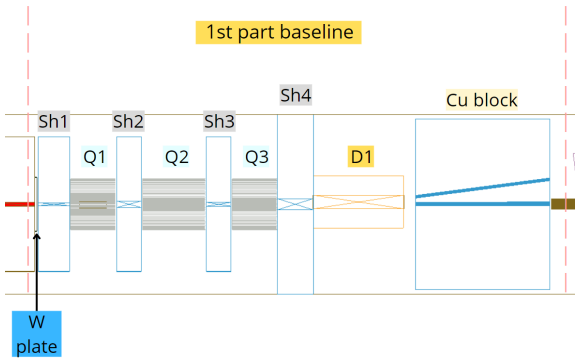

Figure 44: First part of ENUBET tlr6v6 beamline.

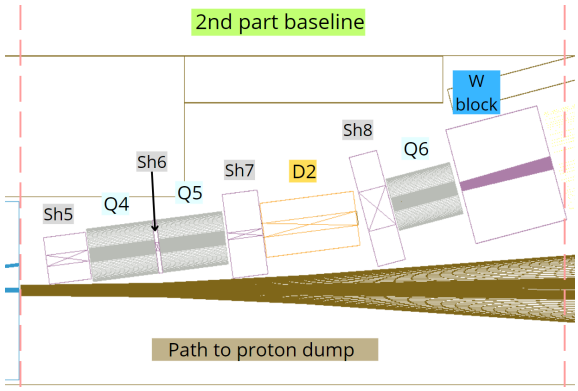

Figure 45: Second part of ENUBET tlr6v6 baseline.

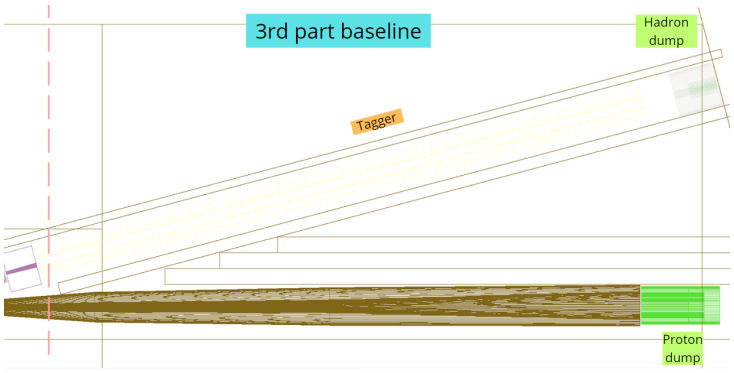

Figure 46: Third part of ENUBET tlr6v6 baseline.

6 Signal and noise optimisation by tunning the beamline parameters

After discussing the relevance of ENUBET in future neutrino experiments in Chapter 5, this section focuses in the optimisation of the current experimental ENUBET beamline (tlr6v6) using Geant4 to increase the rate of kaons and pions in the tagger while minimising background interference from other particles.

To achieve this objective, modifications have been made to the geometry of existing components. However, the addition of new elements to the setup is beyond the scope of this thesis. Therefore, the process begins with the evaluation of individual adjustments to identify key parameters that contribute to improved outcomes. These adjustments are then combined to assess their cumulative impact and develop a finalized upgraded configuration. A comprehensive evaluation is ensured by conducting a complete beam simulation using the proposed setup to gauge overall performance.

Furthermore, preliminary work is presented on ENUBET's potential to generate a low-energy neutrino beam by focusing mesons at lower energies. The efficacy of tlr6v6 in selecting lower-energy mesons, resulting in less energetic neutrinos, is analysed in this context.

6.1 Beamline optimization

To enhance beam purity[42] and intensity effectively, our initial approach involves identifying features that can potentially yield improved results compared to the current tlr6v6 setup, illustrated previously in Figures 40 and 41. In this thesis, we have identified four key parameters:

- The thickness of the first tungsten plate.
- The radius of Q1.
- The aperture of the copper block collimator.
- The thickness of the last tungsten shield.

We evaluate the impact of each parameter on kaon production and purity individually, followed by an analysis of their combined effects. Results from different configurations are presented to optimise these parameters. Subsequently, the most promising setup is selected for a comprehensive beam simulation to compare outcomes with both tlr6v6 and the proposed configurations, ensuring a thorough evaluation process. The selected statistics employed for these simulations are 1.17×10^9 pot.

[42]By purity it is understood in the context of this project as the minimisation of the external antimuons and positrons hitting the calorimeter in the tagger since they will falsely count as neutrino events.

6.1.1 Individual adjustments

Improvements have been observed with specific adjustments:

1. Increase in the yield of kaons by enlarging the radius of Q1 and the aperture of the copper block collimator.
2. Purity enhancement, particularly for e^+ and μ^+, by extending the thickness of the first tungsten plate and the last tungsten shield.

Geant4 visualisations accompany each configuration to provide a visual understanding of the modifications.

Radius Q1

Q1 generates a magnetic field as the first collimator of charged particles. Increasing the radius of its aperture can possibly increase the kaon rates (thereby preventing absorption by the outer Q1 shield), as depicted in Figure 47.

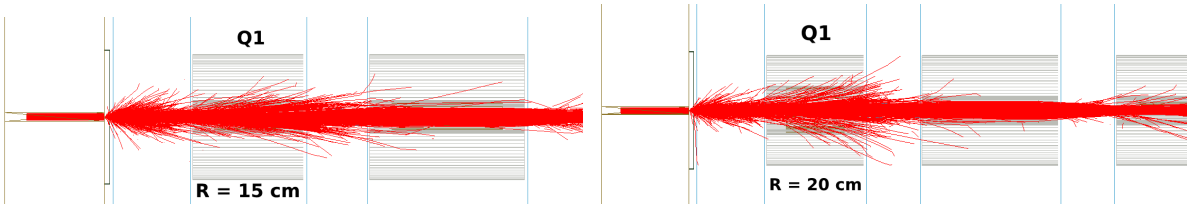

Figure 47: Geant4 top view of 10000 K^+ trajectories at 8.5 GeV from the target (red lines). In each picture, the radius of the quadrupole Q1 ("R") is changed, originally 15 cm (left) and 20 cm (right).

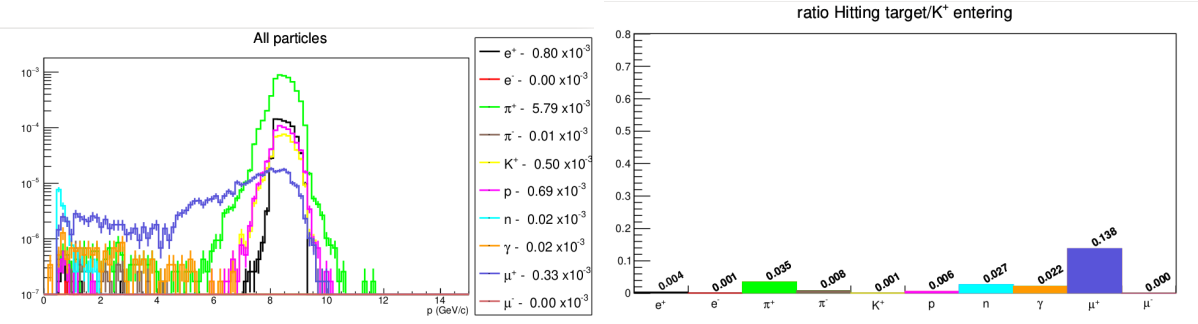

Figure 48: Geant4 tlr6v6 simulation with 20 cm of Q1 radius. On the left, the particle spectra in ppot entering the tagger. On the right, the ratio of particles hitting the tagger detectors with respect to the number of K^+ entering.

To assess the effects, a simulation was conducted with a 20 cm aperture radius instead of the original 15 cm. The results, illustrated in Figure 48, indicate a slight increase in the number of kaons from 0.48×10^{-3} ppot to 0.50×10^{-3} ppot. One possible explanation is statistical fluctuation, suggesting to check the effects with a higher number of pot.

However, particle ratio also rises, with particular concern for μ^+(from 0.132 to 0.138) and e^+ (from 0.001 to 0.004, which is undesirable).

Aperture collimator

Following the bending induced by dipole D1, the beam is collimated within a copper block. Particles with momenta deviating from 8.5 GeV are likely to be absorbed in this component, facilitating momentum selection. In tlr6v6, the aperture is minimal to prevent downstream contamination outside the region of interest. However, as illustrated in Figure 49, increasing the aperture ratio impacts on less kaons absorbed in the collimator.

To assess this effect, the aperture radius was increased from 30 mm to 45 mm, as shown in Figure 50. As anticipated, the number of K^+ notably rises from 0.48×10^{-3} ppot to 1.02×10^{-3} ppot, along with an increase in π^+ from 5.80×10^{-3} ppot to 12.22×10^{-3} ppot. However, particle ratios remain unchanged, except for positrons, which triples compared to the original value. This increase occurs because widening the collimator aperture broadens the momentum spectra of particles reaching the tagger, allowing looser momentum selection. Monte Carlo statistical fluctuation can be also affecting slightly the difference between results.

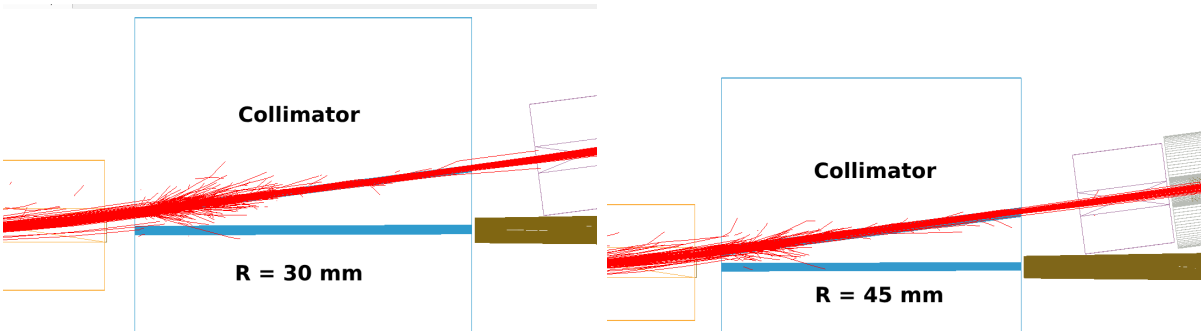

Figure 49: Geant4 top view of 10000 K^+ trajectories at 8.5 GeV from the target (red lines). In each picture, the radius of the collimator block ("R") is changed, originally 30 mm (left) and 45 mm (right).

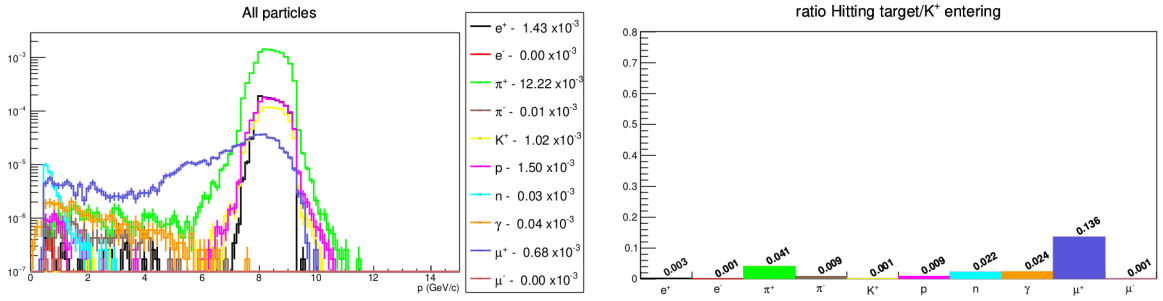

Figure 50: Geant4 tlr6v6 simulation results considering 45 mm of radius aperture in the copper block collimator. On the left, the particle spectra in ppot entering the tagger. On the right, the ratio of particles hitting the tagger detectors with respect to the number of K^+ entering.

Thickness of the first tungsten plate

Cascades must traverse a tungsten plate designed to absorb undesired particles. Of particular importance is the reduction of positrons, as their entry into the tagger increases the likelihood of false positives when selecting e^+ associated to ν_e. Since there are no further components downstream for positron absorption, the tungsten plate plays a crucial role in their reduction.

Originally set at a thickness of 50 mm, simulations involving 10,000 positrons at 8.5 GeV reveal that a small fraction manages to pass through. However, increasing the thickness to 70 mm ensures complete absorption of these positrons, as illustrated in Figure 51.

Simulation results from Figure 52 show that the number of positrons entering the tagger decreases from 0.80×10^{-3} ppot to 0.68×10^{-3} ppot, while contamination from other particles also reduces. However, this adjustment results in a slight decrease in the number of K^+ particles in the tagger, from 0.48×10^{-3} ppot to 0.47×10^{-3} ppot.

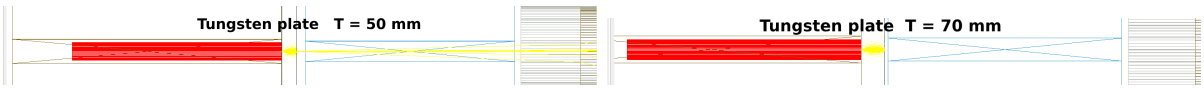

Figure 51: Geant4 top view of 10000 e^+ trajectories at 8.5 GeV from the target (yellow lines). In each picture, the thickness ("T") of the first tungsten plate is changed, originally 50 mm (left) and 70 mm (right).

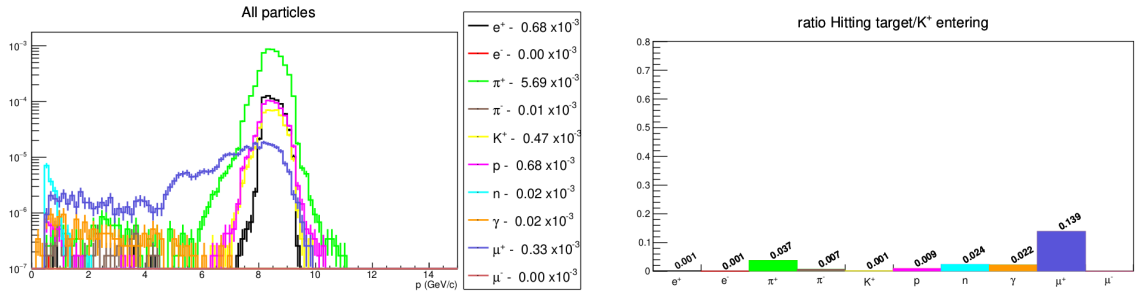

Figure 52: Geant4 tlr6v6 simulation results considering 70 mm of tungsten plate thickness. On the left, the particle spectra in ppot entering the tagger. On the right, the ratio of particles hitting the tagger detectors with respect to the number of K^+ entering.

Thickness of the last tungsten shield

Prior to entering the tagger, particles must pass through a tungsten collimator intended to prevent contamination in the tunnel. To enhance beam purity, increasing the thickness of this shield is recommended, as indicated in Figure 53, where a longer block appears to absorb more undesired particles.

Figure 54 confirms these expectations. While maintaining the same number of K^+ par-

ticles entering the tagger, the ratio of μ^+ particles significantly decreases from 0.132 to 0.104. However, the positron ratio increases fourfold, with less energetic positrons collected in the detectors compared to the original configuration.

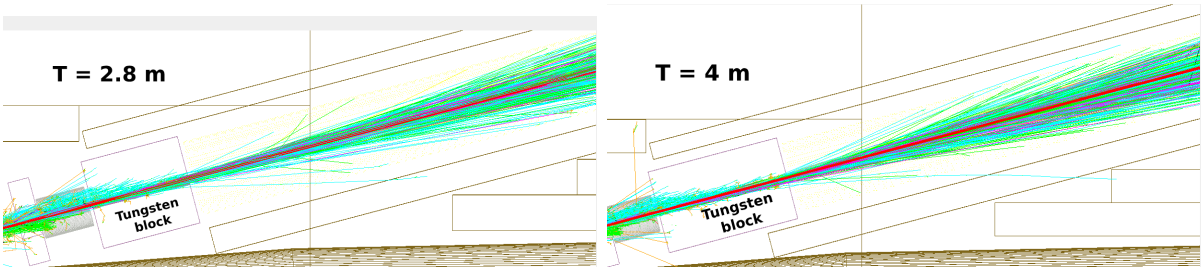

Figure 53: Geant4 top view of 10000 K^+ trajectories at 8.5 GeV from the target, displaying different particles arriving at the tagger by colors. In each picture, the thickness of the last tungsten shield is changed, originally 2.8 m (left) and 4 m (right).

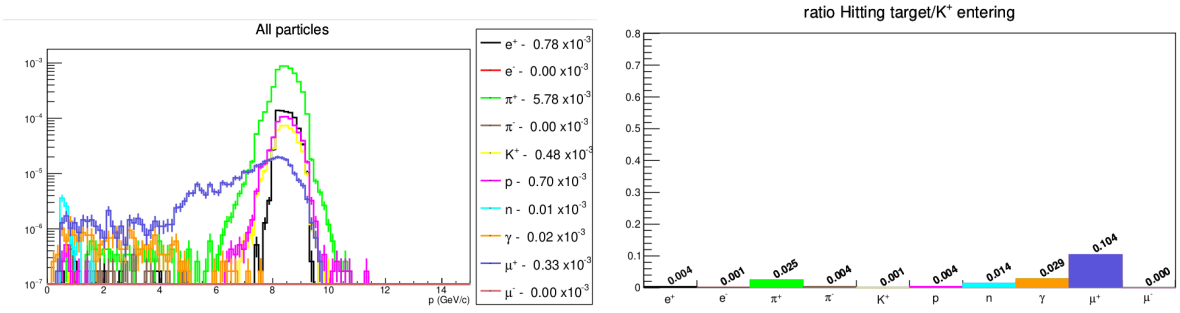

Figure 54: Geant4 tlr6v6 simulation results considering 4 m thickness in the final tungsten shield. On the left, the particle spectra in ppot entering the tagger. On the right, the ratio of particles hitting the tagger detectors with respect to the number of K^+ entering.

6.1.2 Combinations of parameters changes

After individually adjusting parameters and identifying elements crucial for enhancing kaon yield and beam purity, two key modifications emerge: increasing the collimator aperture to capture more K^+ in the tagger, and extending the thickness of the last tungsten shield to primarily reduce the ratio of μ^+. Meanwhile, enlarging the radius of Q1 and the thickness of the tungsten plate appears to slightly increase the number of K^+ while absorbing more e^+. These effects are summarised as follows:

- Increasing the thickness of the tungsten plate: decreases the positrons entering in the tagger at the expenses of a larger muon ratio.
- Enlarging the Q1 radius: more kaons reach the tagger while particle ratio slightly rises.
- Increasing the collimator radius: noticeably increases the number of kaons in the tagger despite the increment in the particle ratio hitting the calorimeter.

- Enlarging the thickness of the tungsten shield: prevents spurious background to hit the detectors, however it leads to an increase in the positron ratio.

This section explores the collective effects of different combinations of these modifications, as listed in Table 4. Combinations 1-3 aim to observe the effects by gradually incorporating modifications, while combinations 4 and 5 focus on the optimisation of the thickness of the last tungsten collimator. All Geant4 simulation results are presented in Figures 55 and 56 and a comparison between numerical values is found in Table 5.

Combination	Collimator R (mm)	TP T (mm)	Q1 R (cm)	TS T (m)
Original	30	50	15	2.8
1	60	50	15	8
2	60	50	20	8
3	60	80	20	8
4	60	80	20	6
5	60	80	20	5

Table 4: Combinations explored in Geant4, where "Collimator R", "TP T", "Q1 R" and "TS T" refer respectively to the collimator radius, tungsten plate thickness, Q1 radius and tungsten collimator thickness. The original tlr6v6 configuration parameters is also shown for comparison.

Combination 1

The first combination examines the collective effects of the most influential elements: a collimator radius of 60 mm and a last shield thickness of 8 m. The aim of using such large value for the last shield is to investigate whether particle ratios can be minimised.

Compared to the original configuration, this combination results in a significant increase in the number of kaons and pions, from 0.48×10^{-3} ppot to 1.34×10^{-3} ppot for K^+, and from 5.80×10^{-3} ppot to 17.57×10^{-3} ppot for π^+. While μ^+ ratio is reduced from 0.133 to 0.090, the rest of particle ratios are notably increased. Of particular concern is the increase in e^+ (six times the original value).

Therefore, while this combination successfully increases the number of kaons by almost threefold, fulfilling a primary objective of this Thesis work, attention must be given to reducing the presence of non-kaon and non-pion particles, especially e^+.

Combination 2

In this setup, the radius of Q1 is increased to 20 cm in addition to the modifications made previously. As suggested in Section 6.1.1, a significant contribution is not expected, but a slight increase in the number of K^+ entering in the tagger is anticipated.

The results confirm an increase to 1.38×10^{-3} ppot for K^+ and 0.10×10^{-3} ppot for π^+. Particle ratios barely changed, with only a slight increment to 0.007 for e^+.

Combination 3

To mitigate the flux of e^+ particles into the tagger, this combination enlarges the thickness of the first tungsten plate from 50 mm to 80 mm in an attempt to achieve a significant reduction.

Despite the observed reduction of e^+ in the tagger by 25%, the ratio of the ones hitting the tunnel walls over the kaons entering the tunnel remains unchanged. One possible explanation could be the simultaneous reduction in K^+ particles, which decreases to 1.26×10^{-3} ppot. Therefore, this adjustment does not yield significant improvements in the purity.

Combination 4

Observing the increased ratio of particles hitting the calorimeter resulting from the previous modifications, this configuration aims to mitigate it by reducing the thickness of the last tungsten shield to 6 m.

The Geant4 simulations indicate a notable reduction in spurious events detected, albeit with an increase in the μ^+ ratio.

Combination 5

Through simulation, it was observed that, concerning particles hitting the calorimeter, reducing the shield thickness decreased the amount of e^+ while increasing μ^+, which is favorable for K_{e3} positron monitoring. Conversely, increasing the shield length produced more e^+ and less μ^+, suitable for muon monitoring. Therefore, a balanced thickness of 5 m was chosen.

For the other parameters:

- Increasing the collimator aperture notably increased e^+ in the tagger, which is undesirable.

- Further increasing the Q1 radius resulted in a higher particle ratio hitting the calorimeter, with only a minimal increase in K^+, making it not beneficial.

With respect the previous combination, the ratios in the tagger are lowered (especially for positrons, going from 0.005 to 0.003), despite a slight reduction in the ppot number of kaons and pions entering the tagger. Therefore this configuration is proposed as the optimal one between the ones listed in Table 4.

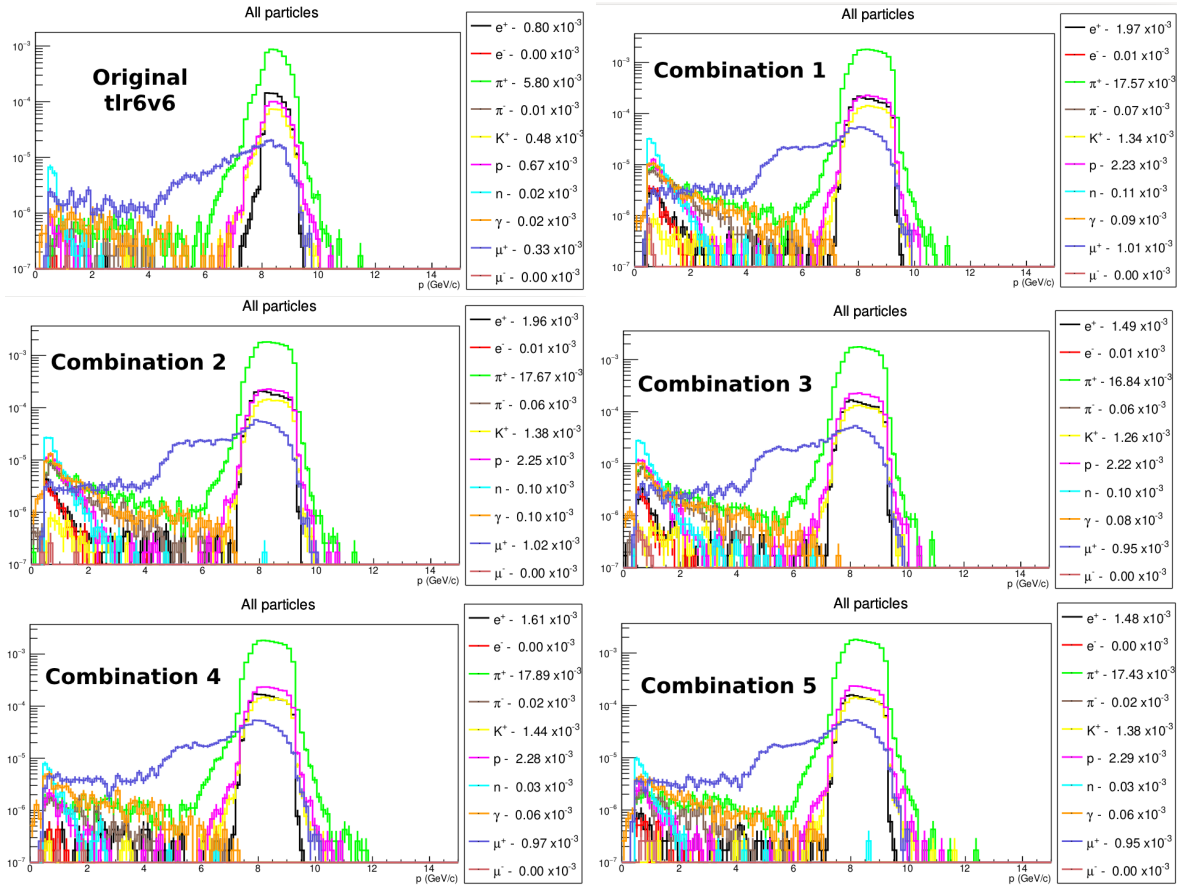

Figure 55: Geant4 tlr6v6 simulation results particle momentum spectra in ppot entering the tagger, comparing between the original and the modified configurations, listed in Table 4.

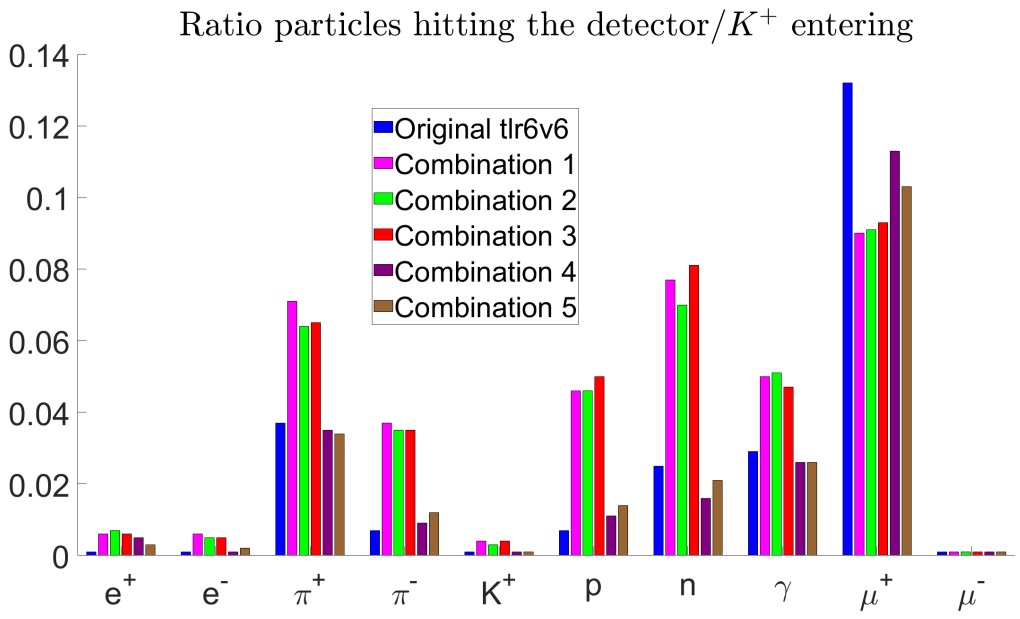

Figure 56: Geant4 simulation results on ratio of particles hitting the calorimeters per kaon entering in the tagger for the different combinations listed in Table 4.

Configuration	K^+ ($\times 10^{-3}$ ppot)	π^+ ($\times 10^{-3}$ ppot)	e^+/K^+	μ^+/K^+	π^+/K^+
Original tlr6v6	0.48	5.80	0.001	0.132	0.037
Combination 1	1.34	17.57	0.006	0.090	0.071
Combination 2	1.38	17.67	0.007	0.091	0.064
Combination 3	1.26	16.84	0.006	0.093	0.065
Combination 4	1.44	17.89	0.005	0.113	0.035
Combination 5	1.38	17.43	0.003	0.103	0.034

Table 5: Simulation results concerning the amount of kaons and pions entering in the tagger in ppot and the ratio of kaons, antimuons and pions hitting the calorimeter per kaon in the tunnel. It can be compared the original tlr6v6 configuration with the 5 combinations listed in Table 4. For all these simulations it has been used 1.18×10^7 pot.

6.1.3 Complete beam simulation performance results

After testing various configurations, Table 50 displays the geometric changes proposed in this Thesis to achieve better results compared to the original tlr6v6 configuration.

Combination	Collimator R (mm)	TP T (mm)	Q1 R (cm)	TS T (m)
Original tlr6v6	30	50	15	2.8
5	60	80	20	5

Table 6: Tunning parameter values for the original configuration and this Thesis' proposal, where "Collimator R", "TP T", "Q1 R" and "TS T" refer respectively to the collimator radius, tungsten plate thickness, Q1 radius and tungsten collimator thickness.

However, the previous simulations have been run with 1.17×10^7 pot, which are referred in this Thesis as "reduced simulations". This subsection aims at assessing the impact of possible statistical fluctuations in the previous results, by considering a larger sample (10^9 pot, denoted as "complete simulations") for both the original tlr6v6 and the included modifications from combination 5. The graphical results are displayed in Figures 57 and 58 with numerical values provided in Table 7. In Appendix B.1 there are more details concerning the associated beam time using the former statistics.

Considering the original tlr6v6 configuration, there are noticeable differences with respect to the reduced simulation:

- Particle momentum spectra entering in the tagger: the uncertainties are lowered, easing the reading of particles in the low momentum region. However, the absolute values barely changed, hinting that the statistics employed during the whole work are accurate enough for determining the particle momentum spectra entering in the

tagger.

- Particle ratio hitting the calorimeter: it can be noted that the positrons ratio has triplicated, suggesting that one should increase this parameter when interpreting the results from the reduced simulations.

Concerning the combination 5 output, both absolute values from the momentum spectra particle entering the tagger and the ratio of particles hitting the tagger are almost unchanged compared to the simulation with lower statistics. Notably, the e^+ ratio slightly changed from 0.003 to 0.004, suggesting indeed statistical fluctuation effects.

Therefore, the comparison between the original tlr6v6 configuration and the proposed combination 5 is summarised as follows:

- Kaon yield: The new configuration achieves a kaon yield of 1.37×10^{-3} ppot, compared to the original 0.48×10^{-3} ppot, marking an increase of almost a factor 3.

- Positron yield: The e^+ in the tagger increments from 0.79×10^{-3} ppot to 1.49×10^{-3} ppot, with a consequent increase from 0.001 to 0.004 in he ratio of positrons hitting the tagger.

- Muon ratio: Combination 5 reduces the hitting ratio from 0.138 to 0.102 while triplicating the number per pot of μ^+ entering the tagger. This suggests that the original setup had a significant number of external antimuons interfering with the detectors, whereas Combination 5 effectively reduces this interference, leading to more accurate neutrino beam monitoring.

- Pion yield: The proposed configuration yields 17.42×10^{-3} ppot, compared to the original 5.78×10^{-3} ppot. The ratio of π^+ hitting the target decreases slightly, indicating a lower fraction of π^+ hitting the calorimeter.

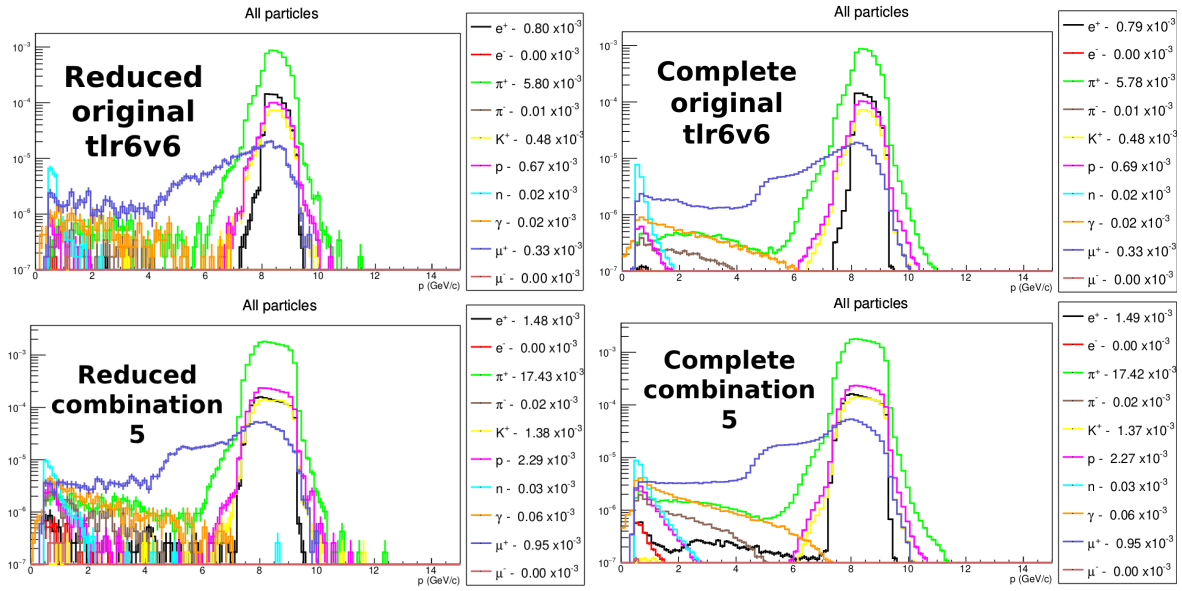

Figure 57: Particle momentum spectra in ppot entering the tagger for the original tlr6v6 configuration and combination 5 for a reduced number of statistics (1.17×10^7 pot) and the denoted "complete" simulations (10^9 pot).

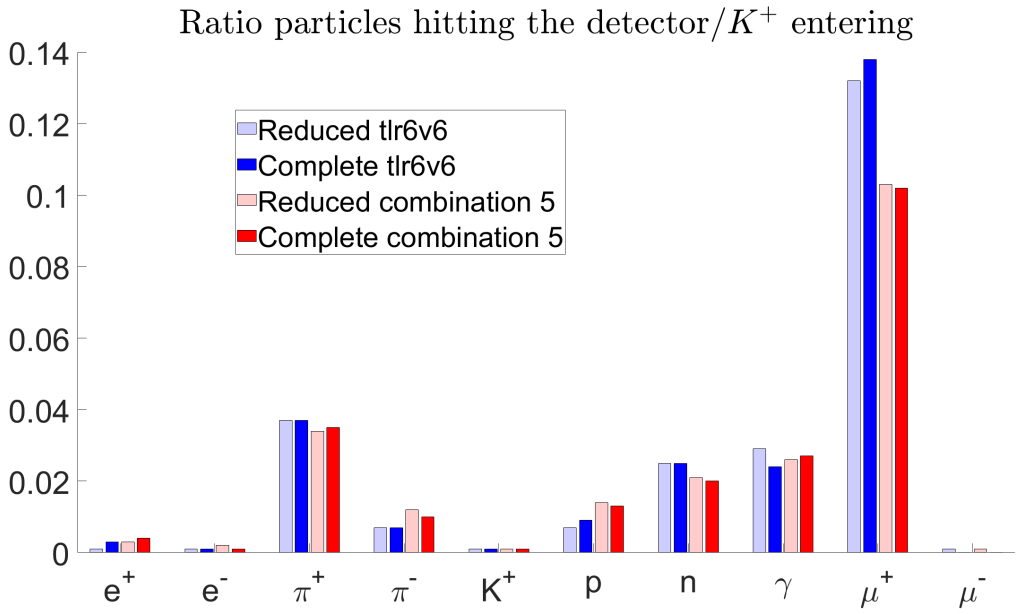

Figure 58: Ratio of particles hitting the calorimeters per kaon entering in the tagger for the original tlr6v6 configuration and combination 5 for a reduced number of statistics (1.17×10^7 pot) and the denoted "complete" simulations (10^9 pot).

6.2 Low energy beam production

As shown previously in Figure 39, with a selection of 8.5 GeV meson momenta, neutrinos are produced in the meson decay with energies around 7 GeV (K^+) and 3 GeV (π^+). We have then tried to check the performance when focusing a lower energy meson beam that

Configuration	K^+ ($\times 10^{-3}$ ppot)	π^+ ($\times 10^{-3}$ ppot)	e^+/K^+	μ^+/K^+	π^+/K^+
Reduced tlr6v6	0.48	5.80	0.001	0.132	0.037
Complete tlr6v6	0.48	5.78	0.003	0.138	0.037
Reduced comb. 5	1.38	17.43	0.003	0.103	0.034
Complete comb. 5	1.37	17.42	0.004	0.102	0.035

Table 7: Simulation results concerning the amount of kaons and pions entering in the tagger in ppot and the ratio of kaons, antimuons and pions hitting the calorimeter per kaon in the tunnel. It can be compared the original tlr6v6 configuration with the proposed combination 5 for reduced (1.18×10^7 pot) and complete (10^9 pot) statistics.

produces neutrinos in the Hyper-Kamiokande region of interest.

To assess the impact of lowering the meson momentum selection, the configuration used to test the performance at different momentum filtering scenarios will include the two most important modifications from the aforementioned combinations:

- 60 mm of collimator aperture radius (originally 30 mm).

- 4 m of thickness in the last tungsten shield (2.8 m in tlr6v6 configuration).

The neutrino flux and rates, in arbitrary units (a.u.), for selecting 8.5 GeV mesons are shown in Figure 59. π^+ generate a larger population than K^+, surpassing them by a factor of 16 in the tagger while having similar decay times (26 ns for π^+ and 12 ns for K^+). This is due to the emission angle and the difference in the branching ratios.

While the majority of neutrinos are produced in the tagger, there is a significant neutrino flux at smaller energies throughout the setup, which could affect purity in producing a lower-energy neutrino beam.

To accomplish this lower energy beam, a lower meson momentum selection is necessary. This involves modifying the existing magnetic field intensities from dipoles and quadrupoles (see Appendix B.2). As a preliminary analysis, we consider situations with meson momenta of 3.5 GeV and 2.0 GeV.

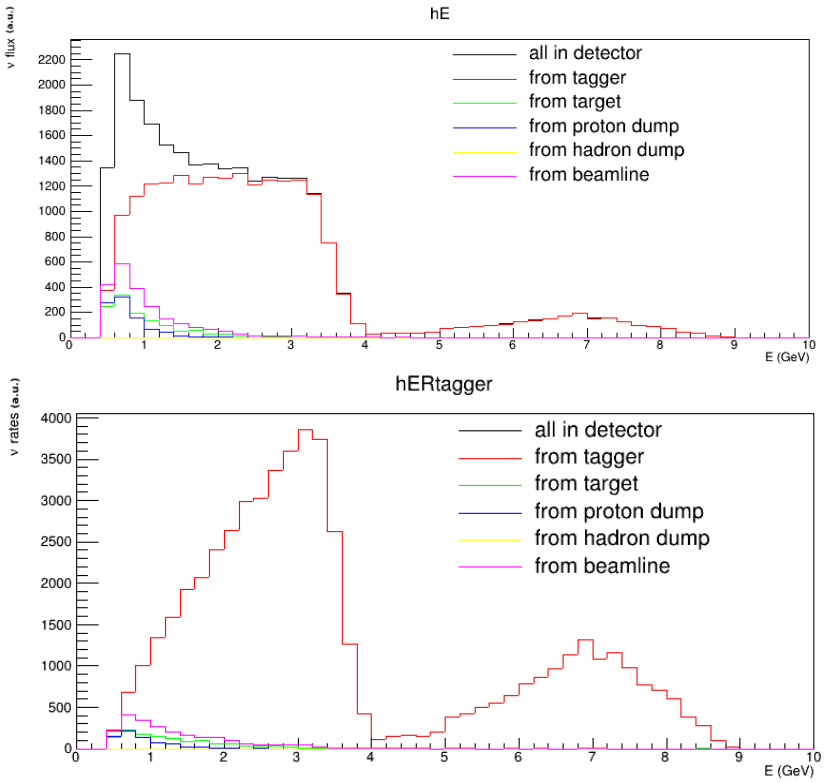

Figure 59: Geant4 tlr6v6 neutrino beam flux (top) and rates (bottom) detection in arbitrary units (a.u.) considering 4 m thickness in the final tungsten shield and 60 mm of collimator radius aperture. Meson momentum selection is 8.5 GeV. The rates are obtained by weighting the neutrino energy.

Neutrino beam results for meson momentum of 3.5 GeV

The results obtained using a meson momentum selection of 3.5 GeV are displayed in Figure 60. Neutrinos predominantly fall within the range of [0.5, 1.5] GeV, with a peak rate of 1800 a.u., reduced by a factor of 0.48 compared to the 8.5 GeV case. Nearly all neutrinos are generated from π^+ decay, as K^+ neutrinos are less. As expected, there is a larger relative contamination in the region of interest compared to the 8.5 GeV case.

To further understand these observations, the spectra of particles entering the tagger and the particle ratios are presented in Figure 61. The number of kaons detected in the tagger is 0.17×10^{-3} ppot, smaller by a factor 9 if compared to the value obtained with a meson momentum selection of 8.5 GeV in the same beamline configuration, which was 1.48×10^{-3} ppot. The number of pions is reduced by a factor 6. This can be caused by the decrease in the γ factor resulting from the lower momentum selection which increases the decay probability for the same path, thus resulting in fewer mesons reaching the tagger.

Furthermore, the particle ratios are significantly higher due to the reduced presence of K^+ and the increased presence of μ^+ and e^+ at low energies compared to the original 8.5 GeV situation.

Further improvements are expected with a full tunning of the beamline.

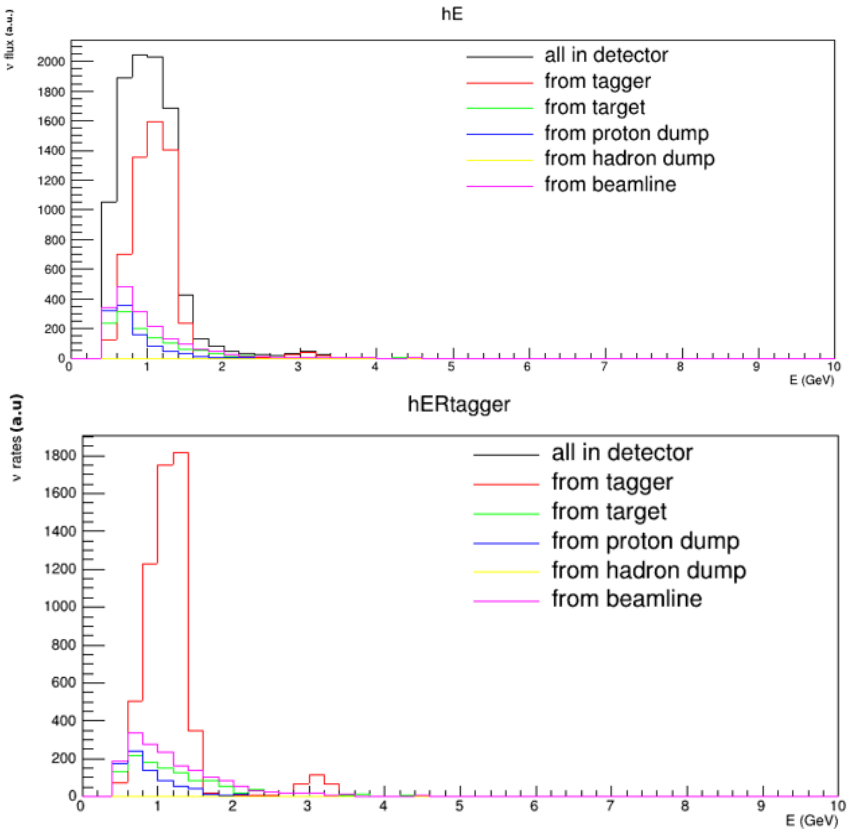

Figure 60: Geant4 tlr6v6 neutrino beam flux (top) and rates (bottom) detection in arbitrary units (a.u.) considering 4 m thickness in the final tungsten shield and 60 mm of collimator radius aperture. Meson momentum selection is 3.5 GeV.

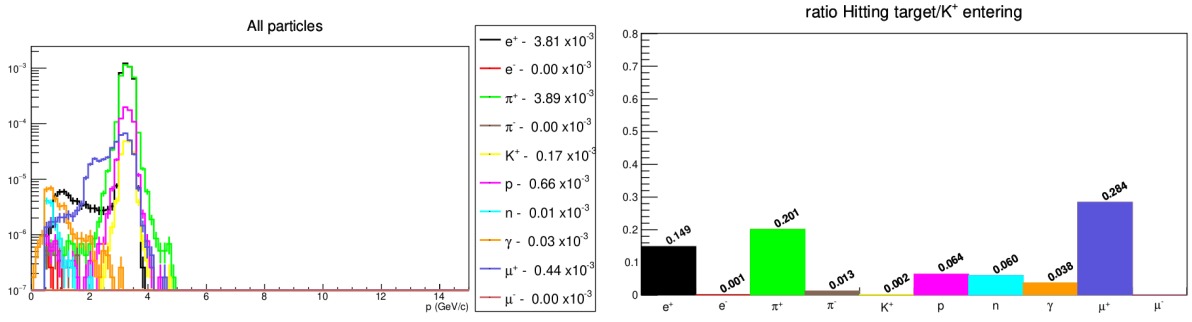

Figure 61: Geant4 tlr6v6 simulation results in 3.5 GeV meson selection considering 4 m thickness in the final tungsten shield and 60 mm of collimator aperture radius. On the left, the particle spectra in ppot entering the tagger. On the right, the ratio of particles hitting the tagger detectors with respect to the number of K^+ entering.

Neutrino beam results for meson momentum of 2.0 GeV

As shown in Figure 62, selecting meson momenta of 2.0 GeV results in a neutrino beam energy of approximately 0.75 GeV. The peak rate is slightly lower compared to the 3.5 GeV case, reaching 1600 a.u..

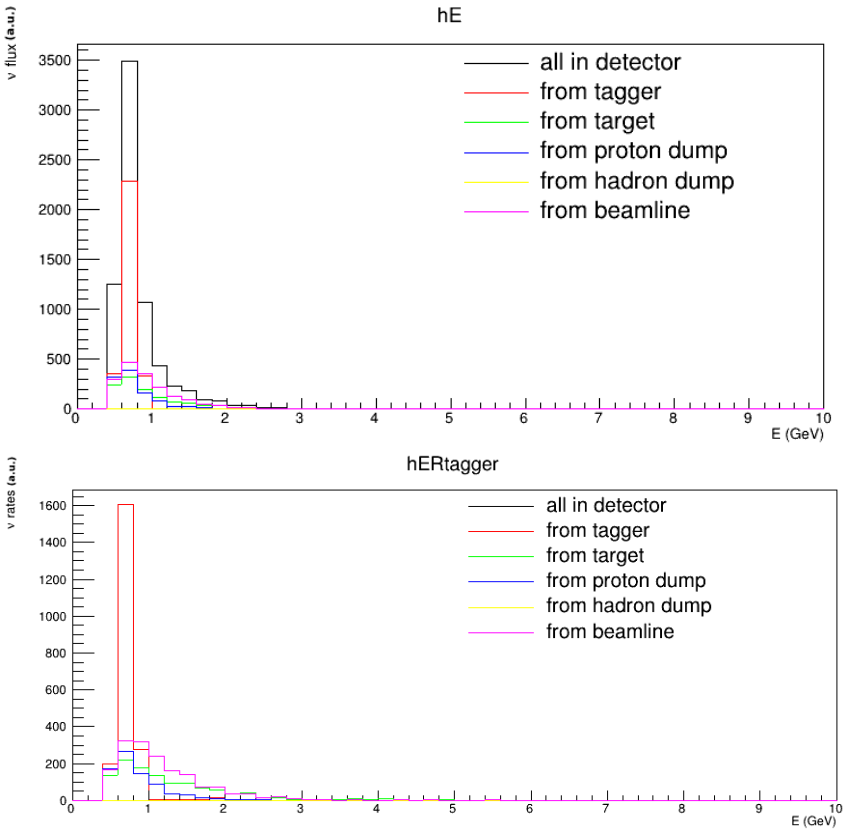

Figure 62: Geant4 tlr6v6 neutrino beam flux (top) and rates (bottom) detection in arbitrary units (a.u.) considering 4 m thickness in the final tungsten shield and 60 mm of collimator radius aperture. Meson momentum selection is 2.0 GeV.

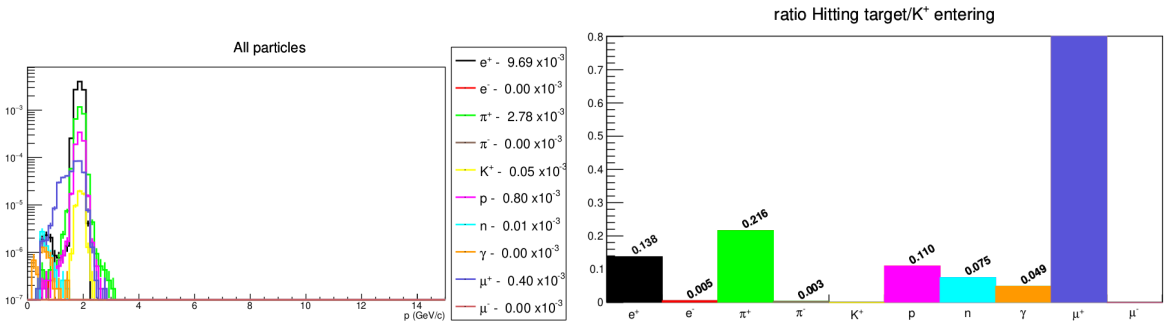

Figure 63: Geant4 tlr6v6 simulation results in 2.0 GeV meson selection considering 4 m thickness in the final tungsten shield and 60 mm of collimator aperture radius. On the left, the particle spectra in ppot entering the tagger. On the right, the ratio of particles hitting the tagger detectors with respect to the number of K^+ entering.

Examining the particle spectra and particle ratios obtained for this setup in Figure 63, the amount of kaons entering in the tagger is drastically reduced, 0.05×10^{-3} ppot. This is consistent with the practical absence of neutrinos from K^+ decay. Additionally, pions are reduced from 3.89×10^{-3} ppot to 2.78×10^{-3} ppot.

Moreover, the μ^+ ratio is excesively high, indicating a strong likelihood of obtaining fake neutrino events when using coincidence measurements in the hadron dump.

Conclusions

We have shown the performance of the tlr6v6 enubet beamline (with an increased collimator radius and tungsten shield thickness up to 60 mm and 4 m respectively), which is optimised for selecting mesons with 8.5 GeV in the tagger, at lower energies. The results are promising, especially at 3.5 Gev. The ν produced out of the tagger are significant but not prohibitive to further explore lower momentum meson scenarios.

A significant reduction in K^+ and π^+ in the tagger is evident, suggesting that decreasing the beamline's length may be a potential solution. This could involve decreasing the number of quadrupoles or shortening the thickness of the existing elements to increase the non-decay probability of these charged mesons until reaching the tunnel decay.

In the 1 GeV neutrino energy range, only π^+ contributes to their production, with very few K^+ decays achieved. This is very interesting to consider given the current efforts to include instrumentation in ENUBET's forward region to monitor as well these neutrinos. Furthermore, there is a high presence of external e^+ and μ^+ in the tagger compared to the original configuration. It will be helpful to investigate the effects of shields between the different components in the setup, as they may further enhance the interaction probability of the mesons throughout the beamline.

Part V

Summary of the work and future expectations in neutrino physics research

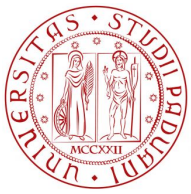

UNIVERSITÀ DEGLI STUDI DI PADOVA

7 Summary and future perspective in neutrino physics

The discovery of the neutrino marked a significant breakthrough for the Standard Model, opening various research fields within Physics Beyond the Standard Model, such as CP violation and flavor oscillation. The current generation of long-baseline experiments aims to lay the groundwork for future projects like Hyper-K and DUNE, which are expected to make substantial contributions in these areas. This thesis aims to contribute to their development by analysing the performance of current Monte Carlo generators in the T2K near detector ND280 for CC0π processes and refining the ENUBET beam to produce more neutrinos while reducing systematic uncertainties related to the neutrino flux.

In Part II, in collaboration with Seville University, the theory behind neutrino-nucleus interactions without pions in the final state is extensively described. Beginning with the simple case of neutrino-nucleon elastic scattering in Chapter 2, the procedure to compute the cross section from the corresponding Feynman diagram within the framework of relativistic quantum mechanics is explained. This includes the introduction of hadronic and leptonic tensors (or the nuclear response functions included in $\mathscr{F}_\chi$) and nucleon form factors. In the case of a free nucleon, nuclear effects are not considered, resulting in theoretical predictions that differ from light-nuclei experimental data. However, this framework lays the foundation for understanding neutrino-nucleus scattering.

Chapter 3 delves into the theory behind CC0π events, including in the regime of quasielastic scattering, MEC-2p2h, and pion absorption. It also provides a comprehensive description of theoretical approaches used to model the nuclear effects leading to these processes. Starting with the RFG model, it introduces concepts such as Fermi motion and removal energy to account for the constraints within the nuclear medium. The LFG model is presented as a more sophisticated approach to consider the nucleon momentum distribution inside the nucleus. In the context of SuperScaling, SuSAv2-QE employs scaling functions from the RMF theory that reproduces the (e, e') experimental scaling data and refines the cross section by implementing a blend of RMF and RPWIA while maintaining the RFG framework. Finally, the SF model is detailed, which uses a spectral function to account for the nuclear effects of the medium.

In Part III, in collaboration with CERN, NEUT and GENIE neutrino Monte Carlo generators were used to obtain the CC0π cross section under the models of LFG, SF, and SuSAv2. The goal was to assess the agreement with the ND280 experimental data from T2K for both neutrino and antineutrino incident fluxes. Additionally, the nuclear dynamics simulations employed for the DUNE experiment were included in the analysis. The p-value analysis indicated a rejection of the predicted results for all four models, particularly in the forward region where the Monte Carlo cross section is generally overestimated. This suggests that nuclear effects are not yet effectively reproduced by the models.

While LFG is highly tuned, RPA or FSI might not be accurate enough to reproduce the ND280 data for small scattering angles. SF, however, relies on PWIA, which might be too simplistic to describe neutrino-nucleus scattering adequately, thereby justifying the poor agreement in the forward region. SuSAv2-QE also displayed poor performance, although planned theoretical work aims to refine this approach further.

Additionally, the analysis identified an overestimation of χ^2 from the first and last p bins in each angular region, attributed to poor efficiency as noted in technical documents. However, some intermediate energy bins also significantly increased the χ^2 value, suggesting that further research on these bins is necessary.

In Part IV, in collaboration with Padova University, various component geometries of the ENUBET experimental setup were modified using Geant4 to study their influence on the beam produced in the decay tunnel. The proposed configuration aims to increase the number of kaons and pions in the tunnel by enlarging the radius of the first quadrupole and the aperture of the collimator. Contamination is reduced by extending the length of the tungsten plate after the target and the tungsten block before the decay tunnel.

Simulations showed that compared to the original setup, the number of kaons and pions in the tunnel almost tripled, while the muon contamination ratio decreased, despite a moderate in the positron ratio. Depending on whether an electron or muon neutrino beam (or a mix) is desired, the parameters can be adjusted to minimise the external contamination of muons or positrons.

Additionally, a preliminary study was conducted to evaluate low-energy neutrino beams by selecting 3.5 GeV and 2.0 GeV mesons in the tunnel. The Geant4 results indicated that as meson momentum decreases, fewer mesons were achieved with the proposed configuration. This is expected since lower momentum increases the decay probability before reaching the tunnel. Conversely, undesired particles such as positrons and muons have a stronger impact in the tunnel, leading to high contamination levels in these scenarios. Results are promising, but further improvements can be accomplished by shortening the beamline. Further research is needed to reduce the contamination ratio hitting the detectors.

Finally, in the context of refining experimental tools for studying neutrino-nucleus cross sections, the results presented in this Thesis aim to contribute to both T2K and ENUBET. The evaluation of current Monte Carlo generators aids in identifying future improvements, while the enhanced beam proposal serves to achieve a more efficient setup, increasing statistics and reducing relative error in predictions. With the upcoming ND280 upgrade and ENUBET's efforts to improve instrumentation, both collaborations are focused on reducing uncertainties. These steps are crucial for the successful implementation of Hyper-K and DUNE in the near future.

Part VI

Appendices

A Mathematical formalism in neutrino-nucleon cross section

A.1 Theoretical basis of Relativistic Quantum Mechanics [106]

Dirac Equation

In the analysis of neutrino-nucleon elastic charged current scattering, a fundamental understanding is needed in the theoretical framework of Relativistic Quantum Mechanics, specifically the Dirac Equation. Formulated by Paul Dirac in the early 1930s, this equation serves as the starting point for the mathematical development involved in this study. Dirac imposed crucial conditions for this equation:

1. It must be a first-order relativistic equation concerning time t.
2. The norm must be positively defined, implying the Hamiltonian operator's hermiticity in the time parameter.
3. Covariance, ensuring invariance under Lorentz transformations.
4. Consistency with the relation $E^2 = M^2 + |\vec{p}|^2$, where E, M and $\vec{p}$ denote the energy, mass and momentum of a particle respectively.

Satisfying these conditions, Dirac proposed the following equation:

$$i\partial_t \Psi = (\vec{\alpha}\vec{p} + \beta M)\Psi \equiv \hat{H}\Psi. \tag{A.1}$$

Here, $\vec{\alpha}$ and β are 4x4 matrices adhering to specific properties, ensuring the aforementioned requirements. However, the equation can be simplified using gamma matrices(γ_μ) and the slash notation ($\not{A} = \gamma_\mu A^\mu$), leading to the transformed Dirac Equation:

$$\gamma_0 = \beta, \quad \gamma_i = \alpha_i \quad \text{for: } i = 1, 2, 3. \tag{A.2}$$

$$(i\not{\partial} - M)\Psi = (\not{P} - M)\Psi = 0. \tag{A.3}$$

Ψ represents the Dirac wave function, while $\bar{\Psi}$ is the Dirac adjoint, defined as $\bar{\Psi} = \Psi^\dagger \gamma^0$. This foundational framework lays the groundwork for the subsequent mathematical developments in our study of neutrino-nucleon interactions.

Free particle solutions from Dirac Equation

The Dirac Equation, Eq. (A.3), yields solutions for the wavefunction Ψ associated with both positive (+) and negative (-) energy states:

$$\Psi^+(X^\mu) = \sqrt{\frac{M}{EV}} u(p,s) e^{-iP_\mu X^\mu}, \tag{A.4}$$

$$\Psi^-(X^\mu) = \sqrt{\frac{M}{EV}} v(p,s) e^{iP_\mu X^\mu}. \tag{A.5}$$

Here, $u(p,s)$ and $v(p,s)$ represent the Dirac spinors, obtained by solving the respective equations:

$$(\not{P} - M)u(p,s) = 0, \tag{A.6}$$

$$(\not{P} + M)v(p,s) = 0. \tag{A.7}$$

In the Dirac representation, these spinors take the form:

$$u(p,s) = \mathcal{N}\begin{pmatrix} \chi_s \\ \frac{\vec{\sigma}\cdot\vec{p}}{E+M}\chi_s \end{pmatrix}, \tag{A.8}$$

$$v(p,s) = \mathcal{N}\begin{pmatrix} \frac{\vec{\sigma}\cdot\vec{p}}{E+M}\chi_s \\ \chi_s \end{pmatrix}, \tag{A.9}$$

with $\mathcal{N}$ a constant determined by the normalization condition in Eq. (A.10) and $\chi_s = \begin{pmatrix} 1 \\ 0 \end{pmatrix}$ represents the positive spin projection.

$$\bar{u}_\alpha(p_\alpha, s_\alpha)u_\beta(p_\beta, s_\beta) = \delta_{\alpha\beta} \rightarrow \mathcal{N} = \sqrt{\frac{E+M}{2M}}. \tag{A.10}$$

One particular identity that will be highly useful for computing the squared invariant amplitude $|M_{fi}|^2$ in Appendix A.4 is:

$$\sum_{\pm s} u_\alpha(p,s)\bar{u}_\beta(p,s) = \left(\frac{\not{P} + M}{2M}\right)\Bigg|_{\alpha\beta}. \tag{A.11}$$

To sum up, these Dirac wavefunction properties provide a foundational understanding of free particle behavior within the context of the Dirac Equation, setting the stage for further applications in the study of neutrino-nucleon interactions.

Clifford Algebra and Gamma Matrices

The Gamma matrices play a crucial role in the mathematical foundation of the Dirac space, forming what is known as Clifford Algebra. This algebra encompasses the 16 linearly independent 4x4 matrices in the Dirac space, categorized into various types based on their properties. These types include:

$$\Gamma^S = \mathbb{1} \quad \text{Scalar (1)},$$
$$\Gamma^V_\mu = \gamma_\mu \quad \text{Vector (4)},$$
$$\Gamma^{\mu\nu}_T = \sigma^{\nu\mu} = \frac{i}{2}[\gamma^\mu, \gamma^\nu] \quad \text{Tensor (6)},$$
$$\Gamma^P = \gamma_5 = \gamma^5 \quad \text{Pseudoscalar (1)},$$
$$\Gamma^A_\mu = \gamma_5\gamma_\mu \quad \text{Pseudovector or Axial (4)},$$

where the number after the name refer to the number of matrices from that type that conform the Dirac space. These matrices are fundamental when dealing with bilinear

covariants, such as $\bar{\Psi}\Gamma\Psi$, a key aspect in the calculation of the invariant amplitude $|M_{fi}|^2$ involved in leptonic and hadronic currents: Eqs.(2.9),(2.10).

The definition of γ^5 and its properties with respect to other gamma matrices are also noteworthy in this context. γ^5 is defined in Eq. (A.12). It anticommutes with all the other gamma matrices, and it commutes with the tensor matrix $\sigma_{\mu\nu}$. These properties are instrumental in the intricate calculations performed for computing lepton and hadron tensors, contributing to the overall analysis performed for neutrino-nucleon elastic scattering.

$$\gamma^5 = i\gamma^0\gamma^1\gamma^2\gamma^3, \tag{A.12}$$

$$\{\gamma^\mu, \gamma^\nu\} = 2g^{\mu\nu}\mathbb{1}, \tag{A.13}$$

$$(\gamma^i)^{-1} = (\gamma^i)^\dagger = -\gamma^i, \quad (\gamma^0)^{-1} = (\gamma^0)^{-1} = (\gamma^0)^\dagger = \gamma^0, \tag{A.14}$$

$$\{\gamma^\mu, \gamma^5\} = 0, \quad [\gamma_5, \sigma_{\mu\nu}] = 0. \tag{A.15}$$

Trace Theorems

The Trace Theorems is a powerful tool in calculations involving gamma matrices (γ), i.e. during the derivation of the invariant amplitude $|M_{fi}|^2$. These relations facilitate the manipulation of traces. Key aspects of the Trace Theorems include:

- Traces involving an odd number of γ matrices result in null values.
- The trace of the identity matrix $\mathbb{1}$ is 4.
- Traces of products of γ matrices follow specific rules, such as $\mathrm{Tr}(\not{a}\not{b}) = 4ab$ and $\mathrm{Tr}(\not{a}\not{b}\not{c}\not{d}) = 4[abcd + adbc - acbd]$.
- The traces of γ_5 and $\gamma_5\not{a}\not{b}$ are zero, and $\mathrm{Tr}(\gamma_5\not{a}\not{b}\not{c}\not{d})$ involves the Levi-Civita operator $\epsilon_{\alpha\beta\gamma\delta}$: $\mathrm{Tr}(\gamma_5\not{a}\not{b}\not{c}\not{d}) = 4i\epsilon_{\alpha\beta\gamma\delta}a^\alpha b^\beta c^\gamma d^\delta$.

The levi-civita operator $\epsilon_{\alpha\beta\gamma\delta}$ is +1(-1) for an even(odd) permutation of the subscripts. Moreover, it satisfies:

$$\epsilon_{\mu\nu\alpha\beta}\epsilon^{\mu\nu\gamma\sigma} = -2(\delta^\alpha_\lambda\delta^\beta_\sigma - \delta^\alpha_\sigma\delta^\beta_\lambda) \tag{A.16}$$

A.2 Incident flux considerations

The calculation of the incident flux $|\vec{J}_{inc}|$ plays a relevant role in determining the infinitesimal cross section, as outlined in Eq. (2.17). In our approach, a collinear scattering assumption is made, signifying that the initial particles share the same velocity direction, since the nucleon being initially at rest. Expressing this incident flux requires considerations of the velocities of the neutrino ($\vec{v}_i$) and nucleon ($\vec{V}_i$). Since in our framework it is

fulfilled that $\vec{v} = \vec{P}/E$, the resulting expression involves their velocities, energies (ε_i, E_i), and momenta ($\vec{k}_i$, $\vec{P}_i$):

$$|\vec{J}_{inc}|V\varepsilon_i E_i = V\epsilon_i E_i \frac{|\vec{v}_i - \vec{V}_i|}{V} = V\varepsilon_i E_i \frac{\sqrt{v_i^2 + V_i^2 - 2\vec{v}_i \cdot \vec{V}_i}}{V} \approx$$
$$\approx \sqrt{E_i^2 p_i^2 + \varepsilon_i^2 P_i^2 - 2\varepsilon_i E_i \vec{p}_i \vec{P}_i}. \tag{A.17}$$

In the laboratory system, where the nucleon is initially at rest ($\vec{P}_i = \vec{0}$), the nucleon's total energy is its rest mass energy ($E_i^2 = M^2$). For the ultrarelativistic neutrino approximation, the total energy contribution primarily comes from momentum ($\varepsilon_i \approx |\vec{k}_i|$). Using these considerations, the final expression for the incident flux emerges as:

$$|\vec{J}_{inc}|V\varepsilon_i E_i \approx M|\vec{k}_i|. \tag{A.18}$$

A.3 Mathematical derivation double differential cross section

The mathematical derivation of the double differential cross section involves several steps, starting from the infinitesimal cross section expression, Eq. (2.29), and arriving at the final form, Eq. (2.30). The key steps in this process are outlined in this section.

Focusing on lepton kinematics, we express $d^3\vec{k}_l$ in spherical coordinates using Eq. (A.19). We relate the former with the outgoing lepton energy ε_l by using the relation (A.20).

$$d^3\vec{k}_l = |\vec{k}_l|^2 d|\vec{k}_l| d\Omega = |\vec{k}_l|\varepsilon_l d\varepsilon_l d\Omega \tag{A.19}$$

$$E^2 = |\vec{p}|^2 + m^2 \rightarrow EdE = |\vec{p}|d|\vec{p}| \rightarrow d|\vec{p}| = \frac{E}{|\vec{p}|}dE. \tag{A.20}$$

Regarding the final nucleon kinematic parameters, we integrate over the corresponding four-vector P_f first by relating $d^3\vec{P}$ with the integral (see Eq. (A.21), where we introduce the possible nucleon energies parameter P_0) and then performing the calculus taking advantage of the Dirac Delta function. In doing so, we need to employ energy relations, i.e. P_0 with E_f in Eq. (A.22) and utilizing the Dirac Delta property shown in Eq. (A.23), where x_i denotes the poles of the function $f(x)$ in the interval $[a, b]$.

$$\int_0^\infty dP_0 \delta(P_f^2 - M^2) d^3\vec{P} = \int_0^\infty dP_0 \delta[(P_0 - E)(P_0 + E)] d^3\vec{P} = \frac{d^3\vec{P}}{2E}, \tag{A.21}$$

$$P_f^2 - M^2 = P_0^2 - |\vec{P}|^2 - M^2 = P_0^2 - E_f^2 = (P_0 + E_f)(P_0 - E_f), \tag{A.22}$$

$$\delta(f(x)) = \sum_i \frac{\delta(x - x_i)}{|\frac{df}{dx}|_{x_i}} \rightarrow \int_a^b dx \delta(f(x)) = \sum_i \frac{1}{|\frac{df}{dx}|_{x_i}} \rightarrow \int_0^\infty dP_0 \delta(f(P_0)) = \frac{1}{|\frac{d}{dP_0}(f(P_0))|_{P_0 = E_f}} = \frac{1}{2E_f}, \tag{A.23}$$

Introducing a Heaviside distribution $\Theta(P_0)$, allows us to unify the integration domain with respect to momentum, resulting in an integral over the total four-momentum P_f. This operation can be solved efficiently due to the Dirac Delta found within the integral,

leading formally to the conservation of energy $\delta(\omega - \frac{Q^2}{2M})$ after applying the specified steps (A.25) and (A.26).

$$\frac{d^2\sigma}{d\varepsilon_l d\Omega} = \int_{-\infty}^{\infty} d^4P_f \frac{G_F^2}{4\pi^2}\frac{M}{\varepsilon_\nu \varepsilon_l E_f}|\vec{k}_l|\varepsilon_l 2E_f \delta(P_p^2 - M^2)\delta^4(P_p - P_n + p_l - p_\nu)\Theta(P_0)\eta_{\alpha\beta}W^{\alpha\beta} =$$

$$\frac{G_F^2 M}{2\pi^2\varepsilon_\nu}|\vec{k}_l|\delta((K_l - P_i - K_\nu)^2 - M^2)\Theta(\varepsilon_\nu + M - \varepsilon_l)\eta_{\alpha\beta}W^{\alpha\beta} =$$

$$\frac{G_F^2}{4\pi^2\varepsilon_\nu}|\vec{k}_l|\delta(\omega - \frac{Q^2}{2M})\eta_{\alpha\beta}W^{\alpha\beta}, \tag{A.24}$$

$$(Q - P_i)^2 - M^2 = Q^2 - \cancel{P_i^2} - 2QP_i - \cancel{M^2} = -|Q^2| + 2M\omega, \tag{A.25}$$

$$\delta((K_l - P_i - K_\nu)^2 - M^2) = \delta(2M\omega - |Q^2|) = \frac{1}{2M}\delta(\omega - \frac{|Q^2|}{2M}). \tag{A.26}$$

Finally, we arrive at the same expression for the double differential cross-section as the one displayed in the text, Eq. (2.30).

A.4 $|M_{fi}|^2$ calculus

In this section, the calculation of the squared modulus of the invariant amplitude, denoted as $|M_{fi}|^2$, is detailed [107]. This quantity is essential for the computation of the infinitesimal cross section, as seen in Eq. (2.17). In the Standard Model, neutrino spin polarization is clearly defined since they are left-handed (or right-handed for antineutrinos), but the initial nucleon spin polarization is not specified. Therefore, there is a need to average over the initial nucleon spin states (denoted as λ_1, λ_2) and to sum over all final spin states.

To streamline the notation, the symbol Γ_α is introduced, representing $\gamma_\alpha(1 \mp \gamma_5)$. Distinct indices, α and β, are employed for differentiation during multiplication. The calculation is initiated with the definition of $|M_{fi}|^2$, explicitly expressed in terms of the leptonic ($\eta_{\alpha\beta}$) and hadronic ($W^{\alpha\beta}$) tensors.

$$|M_{fi}|^2 = \sum_{s_l, S_f} |(\bar{u}_l \Gamma_\alpha u_v)(\bar{U}_f \Gamma^\alpha U_i)|^2 =$$

$$\left(\sum_{s_l} \bar{u}_l \Gamma_\alpha u_l \bar{\Gamma}_\beta \left(u_\nu \bar{u}_\nu\right)\right)\left(\sum_{S_f} \bar{U}_f \Gamma^\alpha U_f \bar{\Gamma}^\beta \left(U_i \bar{U}_i\right)\right) =$$

$$\left(\sum_{s_l} (\bar{u}_l u_l)\left(\Gamma_\alpha \frac{\not{p}_\nu + m_\nu}{2m_\nu}\bar{\Gamma}_\beta\right)\right)\left(\sum_{S_f} (\bar{U}_f u_f)\left(\Gamma_\alpha \frac{\not{P}_i + M}{2M}\bar{\Gamma}_\beta\right)_{\lambda_1\lambda_2}\right) =$$

$$\mathrm{Tr}\left[\frac{\not{p}_l + m_l}{2m_l}\Gamma_\alpha \frac{\not{p}_\nu + m_\nu}{2m_\nu}\bar{\Gamma}_\beta\right]\mathrm{Tr}\left[\frac{1}{2}\frac{\not{P}_f + M}{2M}\Gamma^\alpha \frac{\not{P}_i + M}{2M}\bar{\Gamma}^\beta\right] =$$

$$\frac{1}{32 m_l m_\nu M^2}\mathrm{Tr}[(\not{p}_l + m_l)\gamma_\alpha(1-\gamma_5)(\not{p}_\nu + m_\nu)\gamma_\beta(1-\gamma_5)]\mathrm{Tr}[(\not{P}_p + M)\Gamma^\alpha(\not{P}_n + M)\bar{\Gamma}^\beta],$$

$$|M_{fi}|^2 \equiv 2\frac{\eta_{\alpha\beta}W^{\alpha\beta}}{m_\nu m_l}, \tag{A.27}$$

where a factor 2 has been introduced to simplify calculus. This allows both tensors to be defined with a term $\frac{1}{8}$. Originally, this factor appears naturally for the hadronic tensor,

but since there is no average over the initial spin states of the neutrino, there is a need to divide by a factor 2 the leptonic tensor.

Due to the properties of Dirac spinors, where the orthogonality of products ensures that only non-diagonal elements of the matrices yield non-zero results, it is justified the introduction of traces.

In Eq. (A.27), the leptonic ($\eta_{\alpha\beta}$) and hadronic ($W^{\alpha\beta}$) tensors are defined, involving traces of gamma matrices specific to each current. The meticulous approach involves the careful calculation of each tensor independently, being high relevant the usage of Trace Theorems. This step-by-step procedure sets the stage for the final contraction of both tensors, providing a comprehensive and accurate expression for the squared modulus of the invariant amplitude.

A.4.1 Leptonic tensor $\eta_{\alpha\beta}$

The expression for the leptonic tensor $\eta_{\alpha\beta}$, as outlined in Eq. (A.27), undergoes a meticulous calculation to account for non-zero contributions based on the Trace Theorems.

$$\eta_{\alpha\beta} = \frac{1}{8}\{\mathrm{Tr}[\not{p}_l\gamma_\alpha(1\mp\gamma_5)\not{p}_\nu\gamma_\beta(1\mp\gamma_5)] + m_l m_\nu \mathrm{Tr}[\gamma_\alpha(1\mp\gamma_5)\gamma_\beta(1\mp\gamma_5)]\} \tag{A.28}$$

Focusing on the neutrino situation with the $-$ sign in the axial part, the resulting expression takes the form:

$$\begin{aligned}\mathrm{Tr}[\not{p}_l\gamma_\alpha(1-\gamma_5)\not{p}_\nu\gamma_\beta(1-\gamma_5)] = \mathrm{Tr}[\not{p}_l\gamma_\alpha\not{p}_\nu\gamma_\beta] - \mathrm{Tr}[\not{p}_l\gamma_\alpha\gamma_5\not{p}_\nu\gamma_\beta] - \mathrm{Tr}[\not{p}_l\gamma_\alpha\not{p}_\nu\gamma_\beta\gamma_5] + \mathrm{Tr}[\not{p}_l\gamma_\alpha\not{p}_\nu\gamma_\beta] = \\ 2(\mathrm{Tr}[\not{p}_l\gamma_\alpha\not{p}_\nu\gamma_\beta] - \mathrm{Tr}[\gamma_5\not{p}_l\gamma_\alpha\not{p}_\nu\gamma_\beta]) = \\ 8(p^l_\alpha p^\nu_\beta + p^l_\beta p^\nu_\alpha - p_l p_\nu g_{\alpha\beta} + i\epsilon_{\alpha\beta\lambda_1\lambda_2}p_l^{\lambda_1}p_\nu^{\lambda_2}),\end{aligned} \tag{A.29}$$

$$\begin{aligned}\mathrm{Tr}[\gamma_\alpha(1-\gamma_5)\gamma_\beta(1-\gamma_5)] = Tr[\gamma_\alpha\gamma_\beta] - \mathrm{Tr}[\gamma_\alpha\gamma_5\gamma_\beta] - \mathrm{Tr}[\gamma_\alpha\gamma_\beta\gamma_5] + \mathrm{Tr}[\gamma_\alpha\gamma_5\gamma_\beta\gamma_5] = \\ \mathrm{Tr}[\gamma_\alpha\gamma_\beta] + \mathrm{Tr}[\gamma_\alpha\gamma_\beta\gamma_5] - [\mathrm{Tr}\gamma_\alpha\gamma_\beta\gamma_5] - \mathrm{Tr}[\gamma_\alpha\gamma_\beta] = 0.\end{aligned} \tag{A.30}$$

Therefore it results in:

$$\eta_{\alpha\beta} = p^l_\alpha p^\nu_\beta + p^l_\beta p^\nu_\alpha - p_l p_\nu g_{\alpha\beta} + i\epsilon_{\alpha\beta\lambda_1\lambda_2}p_l^{\lambda_1}p_\nu^{\lambda_2}. \tag{A.31}$$

The symmetric real part and antisymmetric imaginary part, with respect to the interchange of indexes α and β, are noteworthy features characterised from the properties of the Levi-Civita tensor.

A.4.2 Hadronic tensor $W^{\alpha\beta}$

The decomposition of the hadronic tensor $W^{\alpha\beta}$ into vector ($W^{\alpha\beta}_{VV}$), axial ($W^{\alpha\beta}_{AA}$) and vector-axial ($W^{\alpha\beta}_{VA}$) components is initiated with the definition:

$$W^{\alpha\beta} = \frac{1}{8M^2}\mathrm{Tr}[(\not{P}_f + M)\Gamma^\alpha(\not{P}_i + M)\bar{\Gamma}^\beta] = \frac{1}{8M^2}(W^{\alpha\beta}_{VV} + W^{\alpha\beta}_{AA} + W^{\alpha\beta}_{VA}), \tag{A.32}$$

This strategic decomposition allows for a more focused and systematic analysis of each component. As the subsequent steps unfold, the careful treatment of the inner hadron structure contribution Γ^α ensures an accurate evaluation of the individual components, facilitating an in-depth understanding of the hadronic tensor's characteristics.

Vector term $W_{VV}^{\alpha\beta}$

The vector term $W_{VV}^{\alpha\beta}$ of the hadronic tensor is expressed as a combination of various traces, each contributing to the overall structure. Through careful calculation, the following components are obtained:

$$W_{VV}^{\alpha\beta} = \mathrm{Tr}[(\not{P}_f + M)(F_1^V\gamma^\alpha + i\frac{F_2^V}{2M}\sigma^{\alpha\lambda}Q_\lambda)(\not{P}_i + M)(F_1^V\gamma^\beta - i\frac{F_2^V}{2M}\sigma^{\beta\lambda}Q_\lambda)] = \mathscr{C}_{V1}^{\alpha\beta}(F_1^V)^2 + \mathscr{C}_{V2}^{\alpha\beta}\frac{(F_2^V)^2}{4M^2} + \frac{\mathscr{C}_{V12}^{\alpha\beta}}{2M}F_1^V F_2^V, \tag{A.33}$$

where the coefficients are given by:

$$\mathscr{C}_{V1}^{\alpha\beta} \equiv \mathrm{Tr}[(\not{P}_f + M)\gamma^\alpha(\not{P}_i + M)\gamma^\beta] = \mathrm{Tr}[\not{P}_f\gamma^\alpha\not{P}_i\gamma^\beta] + M^2\mathrm{Tr}[\gamma^\alpha\gamma^\beta] =$$
$$4[P_f^\alpha P_i^\beta + P_f^\beta P_i^\alpha + g^{\alpha\beta}(M^2 - P_f\cdot P_i)] = 4[Q^\alpha P_i^\beta + Q^\alpha P_f^\beta + 2P_i^\alpha P_i^\beta - \frac{|Q^2|}{2}g^{\alpha\beta}], \tag{A.34}$$

$$\mathscr{C}_{V2}^{\alpha\beta} = \mathrm{Tr}[(\not{P}_f + M)\sigma^{\alpha\lambda_1}Q_{\lambda_1}(\not{P}_i + M)\sigma^{\beta\lambda_2}Q_{\lambda_2}] = \mathrm{Tr}[\not{P}_f\sigma^{\alpha\lambda_1}Q_{\lambda_1}\not{P}_i\sigma^{\beta\lambda_2}Q_{\lambda_2}] + M^2\mathrm{Tr}[\sigma^{\alpha\lambda_1}Q_{\lambda_1}\sigma^{\beta\lambda_2}Q_{\lambda_2}] =$$
$$-4[P_f^\alpha(P_i^\beta|Q^2| - Q^\beta P_i\cdot q) + P_f\cdot q(P_i\cdot q g^{\alpha\beta} - Q^\alpha P_i^\beta) + P_f\cdot P_i(Q^\alpha Q^\beta - |Q^2|g^{\alpha\beta}) +$$
$$P_f^\beta(P_i^\alpha|Q^2| - Q^\alpha P_i\cdot q) + P_f\cdot q(P_i\cdot|Q^2|g^{\alpha\beta} - P_i^\alpha Q^\beta) + M^2(Q^\alpha Q^\beta - |Q^2|g^{\alpha\beta})] =$$
$$-4[2M^2|Q^2|g^{\alpha\beta} - 2P_i^\alpha P_i^\beta|Q^2| + Q^\alpha Q^\beta(2M^2 - \frac{|Q^2|}{2}) - |Q^2|(P_i^\alpha Q^\beta + Q^\alpha P_i^\beta)], \tag{A.35}$$

$$\mathscr{C}_{V12}^{\alpha\beta} = -i\mathrm{Tr}[(\not{P}_f + M)\gamma^\alpha(\not{P}_i + M)\sigma^{\beta\lambda}Q_\lambda] + i\mathrm{Tr}[(\not{P}_f + M)\sigma^{\alpha\lambda}Q_\lambda(\not{P}_i + M)\gamma^\beta] =$$
$$4M(P_iQ^\alpha - P_i\cdot q g^{\alpha\beta} + P_f\cdot q g^{\alpha\beta} - P_f^\beta Q^\alpha - P_f^\alpha Q^\beta + P_f\cdot q g^{\alpha\beta} + P_i\cdot q g^{\alpha\beta} - P_i^\alpha Q^\beta) =$$
$$-8M(|Q^2|g^{\alpha\beta} + Q^\alpha Q^\beta). \tag{A.36}$$

The derivation involves utilizing trace operations on matrices and careful consideration of the contributing terms. In the simplification process, the definition of $|Q^2|$ and energy-momentum conservation is invoked to express P_f in terms of Q and P_i. The relations are as follows:

$$Q = P_f - P_i \longrightarrow P_f = Q + P_i, \tag{A.37}$$

$$P_f\cdot P_i = \frac{|Q^2|}{2} + M^2, \tag{A.38}$$

$$P_f\cdot Q = -\frac{|Q^2|}{2}. \tag{A.39}$$

Axial term $W_{AA}^{\alpha\beta}$

$$W_{AA}^{\alpha\beta} = \mathrm{Tr}[(\not{P}_f + M)(G_A\gamma^\alpha\gamma^5 + \frac{G_P}{2M}Q^\alpha\gamma^5)(\not{P}_i + M)(G_A\gamma^\beta\gamma^5 + \frac{G_P}{2M}q^\beta\gamma^5)] = \mathscr{C}_{A1}^{\alpha\beta}G_A^2 + \mathscr{C}_{A2}^{\alpha\beta}\frac{G_P^2}{4M^2} + \mathscr{C}_{A12}^{\alpha\beta}\frac{G_PG_A}{2M}, \tag{A.40}$$

with:

$$\mathscr{C}_{A1}^{\alpha\beta} = \mathrm{Tr}[(\not{P}_f + M)\gamma^\alpha\gamma^5(\not{P}_i + M)\gamma^\beta\gamma^5] =$$
$$4(P_f^\alpha P_i^\beta - P_f \cdot P_i g^{\alpha\beta} + P_f^\beta P_i^\alpha - M^2 g^{\alpha\beta}) = 4[2P_i^\alpha P_i^\beta + (Q^\alpha P_i^\beta + P_i^\alpha Q^\beta) - g^{\alpha\beta}(2M^2 - \frac{|Q^2|}{2})], \tag{A.41}$$

$$\mathscr{C}_{A2}^{\alpha\beta} = \mathrm{Tr}[(\not{P}_f + M)Q^\alpha\gamma^5(\not{P}_i + M)Q^\beta\gamma^5] = 4Q^\alpha Q^\beta(M^2 - P_f \cdot P_i) = 2|Q^2|Q^\alpha Q^\beta, \tag{A.42}$$

$$\mathscr{C}_{A12}^{\alpha\beta} = \mathrm{Tr}[(\not{P}_f + M)G_A\gamma^\alpha\gamma^5(\not{P}_i + M)\frac{G_P}{2M}Q^\beta\gamma^5] + \mathrm{Tr}[(\not{P}_f + M)\frac{G_P}{2M}Q^\alpha\gamma^5(\not{P}_i + M)G_A\gamma^\beta\gamma^5] =$$
$$4M(-P_i^\alpha Q^\beta + P_f^\alpha Q^\beta + Q^\alpha P_f^\beta - Q^\alpha P_i^\beta) = 8MQ^\alpha Q^\beta. \tag{A.43}$$

Vector-Axial term $W_{VA}^{\alpha\beta}$

$$W_{AV}^{\alpha\beta} = \mathscr{C}_{V1A1}^{\alpha\beta}F_1^V G_A + \mathscr{C}_{V1A2}^{\alpha\beta}\frac{F_1^V G_P}{2M} + \mathscr{C}_{V2A1}^{\alpha\beta}\frac{F_2^V G_A}{2M} + i\mathscr{C}_{V2A2}^{\alpha\beta}\frac{F_2^V G_P}{4M^2}, \tag{A.44}$$

with:

$$\mathscr{C}_{V1A1}^{\alpha\beta} = \mathrm{Tr}[(\not{P}_f + M)\gamma^\alpha(\not{P}_i + M)\gamma^\beta\gamma^5] + \mathrm{Tr}[(\not{P}_f + M)\gamma^\alpha\gamma^5(\not{P}_i + M)\gamma^\beta] =$$
$$4i(\epsilon^{\lambda_1\alpha\lambda_2\beta}P_{\lambda_1}^f P_{\lambda_2}^i + \epsilon^{\lambda_1\alpha\lambda_2\beta}P_{\lambda_1}^f P_{\lambda_2}^i) = 8i\epsilon^{\lambda_1\alpha\lambda_2\beta}P_{\lambda_1}^f P_{\lambda_2}^i, \tag{A.45}$$

$$\mathscr{C}_{V1A2}^{\alpha\beta} = \mathrm{Tr}[(\not{P}_f + M)\gamma^\alpha(\not{P}_i + M)Q^\beta\gamma^5] + \mathrm{Tr}[(\not{P}_f + M)Q^\alpha\gamma^5(\not{P}_i + M)\gamma^\beta] = 0, \tag{A.46}$$

$$\mathscr{C}_{V2A1}^{\alpha\beta} = i\mathrm{Tr}[(\not{P}_f + M)\sigma^{\beta\lambda}Q_\lambda(\not{P}_i + M)\gamma^\beta\gamma^5] - i\mathrm{Tr}[(\not{P}_f + M)\gamma^\alpha\gamma^5(\not{P}_i + M)\sigma^{\beta\lambda}Q_\lambda] =$$
$$-8Mi[\epsilon^{\alpha\beta\lambda_1\lambda_2}P_{\lambda_1}^f Q_{\lambda_2} + \epsilon^{\alpha\beta\lambda_1\lambda_2}P_{\lambda_1}^i q_{\lambda_2}] = -16Mi\epsilon^{\alpha\beta\lambda_1\lambda_2}P_{\lambda_1}^i P_{\lambda_2}^i, \tag{A.47}$$

$$\mathscr{C}_{V2A2}^{\alpha\beta} = \mathrm{Tr}[(\not{P}_f + M)\sigma^{\alpha\lambda}q_\lambda(\not{P}_i + M)Q^\beta\gamma^5] - \mathrm{Tr}[(\not{P}_f + M)Q^\alpha\gamma^5(\not{P}_i + M)\sigma^{\beta\lambda}Q_\lambda] =$$
$$\frac{i}{2}Q_\lambda Q^\beta\mathrm{Tr}[\not{P}_f[\gamma^\alpha,\gamma^\lambda]\not{P}_i\gamma^5] - \frac{i}{2}Q^\alpha Q_\lambda\mathrm{Tr}[\not{P}_f[\gamma^\alpha,\gamma^\lambda]\not{P}_i\gamma^5] =$$
$$4(\epsilon^{\lambda_1\lambda_2\beta\lambda}P_{\lambda_1}^f P_{\lambda_2}^i Q^\alpha Q_\lambda - \epsilon^{\lambda_1\lambda_2\alpha\lambda}P_{\lambda_1}^f P_{\lambda_2}^i Q^\beta Q_\lambda). \tag{A.48}$$

Notice that $\mathscr{C}_{V1A2}^{\alpha\beta}$ is null due to the properties applied from Trace Theorems.

Final $W^{\alpha\beta}$ expression

After adding up the contributions from $W_{VV}^{\alpha\beta}$, $W_{AA}^{\alpha\beta}$ and $W_{VA}^{\alpha\beta}$, we obtain:

$$W^{\alpha\beta} = -W_1 g^{\alpha\beta} + W_2\frac{P_i^\alpha P_i^\beta}{M^2} + iW_3\frac{\epsilon^{\alpha\beta\lambda_1\lambda_2}P_{\lambda_1}^i q_{\lambda_2}}{2M^2} + W_4\frac{Q^\alpha Q^\beta}{M^2} + W_5\frac{P_i^\alpha Q^\beta + Q^\alpha P_i^\beta}{2M^2}, \tag{A.49}$$

where these W_i functions encompass:

$$W_1 = \frac{|Q^2|}{4M^2}[(F_1^V + F_1^V)^2 + G_A^2] + G_A^2, \tag{A.50}$$

$$W_2 = (F_1^V)^2 + \frac{|Q^2|}{4M^2}(F_2^V)^2 + (G_A)^2, \tag{A.51}$$

$$W_3 = 2G_A(F_1^V + F_2^V), \tag{A.52}$$

$$W_4 = \frac{(F_2^V)^2}{(4M)^2}(|Q^2| - 4M^2) - G_A G_P + \frac{|Q^2|}{(4M)^2}(G_P)^2, \tag{A.53}$$

$$W_5 = W_2. \tag{A.54}$$

As observed with the leptonic tensor $\eta_{\alpha\beta}$, under a change in order of the indexes α, β the real part is symmetric whilst the imaginary contribution is antisymmetric due to the Levi-Civita tensor.

A.4.3 Tensor contraction $\eta_{\alpha\beta}W^{\alpha\beta}$

To perform the contraction between the leptonic and hadronic tensors, we remark that the cross-product between symmetric-antisymmetric parts (referring to a change in order of α, β) will result in null contribution. Therefore, to have non-zero contribution, we need to multiply symmetric-symmetric or antisymmetric-antisymmetric terms.

Regarding symmetric-symmetric contribution multiplication, we obtain:

$$\eta_{\alpha\beta}g^{\alpha\beta} = (p_\alpha^l p_\beta^\nu + p_\beta^l p_\alpha^\nu - p_l \cdot p_\nu g_{\alpha\beta})g^{\alpha\beta} = -2p_l \cdot p_\nu = -2(\varepsilon_l\varepsilon_\nu - |\vec{k}_l||\vec{k}_\nu|\cos\theta) \approx -4\varepsilon_l\varepsilon_\nu \sin^2\frac{\theta}{2}, \tag{A.55}$$

$$\eta_{\alpha\beta}P_i^\alpha P_i^\beta = (p_\alpha^l p_\beta^\nu + p_\beta^l p_\alpha^\nu - p_l \cdot p_\nu g_{\alpha\beta})P_i^\alpha P_i^\beta = 2(p_l \cdot P_i)(p_\nu \cdot P_i) - (p_l \cdot p_\nu)P_i^2 \approx 2M^2\varepsilon_l\varepsilon_\nu \cos^2\frac{\theta}{2}, \tag{A.56}$$

$$\begin{gathered}\eta_{\alpha\beta}Q^\alpha Q^\beta = (p_\alpha^l p_\beta^\nu + p_\beta^l p_\alpha^\nu - p_l \cdot p_\nu g_{\alpha\beta})Q^\alpha Q^\beta = 2(p_l \cdot Q)(p_\nu \cdot Q) - (p_l \cdot p_\nu)Q^2 = \\ 2(p_l \cdot (p_\nu - p_l))(p_\nu \cdot (p_\nu - p_l)) - (p_l \cdot p_\nu)(p_l^2 + p_\nu^2 - 2p_l \cdot p_\nu) = \\ (p_l \cdot p_\nu)(p_\nu^2 + p_l^2) - 2p_l^2 p_\nu^2 \approx 0,\end{gathered} \tag{A.57}$$

$$\begin{gathered}\eta_{\alpha\beta}(P_i^\alpha Q^\beta + Q^\alpha P_i^\beta) = (p_\alpha^l p_\beta^\nu + p_\beta^l p_\alpha^\nu - p_l \cdot p_\nu g_{\alpha\beta})(P_i^\alpha Q^\beta + Q^\alpha P_i^\beta) = \\ 2[(p_l \cdot P_i)(p_\nu \cdot Q) + (p_\nu \cdot P_i)(p_l \cdot Q) - 2(p_l \cdot p_\nu)(P_i \cdot Q)] = 2M(\varepsilon_l m_\nu^2 - \varepsilon_\nu m_l^2) \approx 0.\end{gathered} \tag{A.58}$$

Concerning antisymmetric-antisymmetric term product, we get:

$$\begin{gathered}\eta_{\alpha\beta}\epsilon_{\alpha\beta\lambda_3\lambda_4}P_{\lambda_3}^i Q_{\lambda_4} = (i\epsilon_{\alpha\beta\lambda_1\lambda_2}p_l^{\lambda_1}p_\nu^{\lambda_2})\epsilon^{\alpha\beta\lambda_3\lambda_4}P_{\lambda_3}^i Q_{\lambda_4} = -2i((p_l \cdot P_i)(p_\nu \cdot Q) - (p_l \cdot Q)(p_\nu \cdot P_i)) = \\ -2i(\varepsilon_l M(p_\nu^2 - p_\nu \cdot p_l) - M\varepsilon_\nu(p_l^2 - p_l \cdot p_\nu)) \approx 4iM(\varepsilon_\nu + \varepsilon_l)\varepsilon_l\varepsilon_\nu \sin^2\frac{\theta}{2}.\end{gathered} \tag{A.59}$$

It can be proven that for the antineutrino case, the calculus is analogous, with the difference that we will get a $-$ sign for W_3 instead of $+$ (neutrino situation). With this in mind, the tensor contraction results in:

$$\eta_{\alpha\beta}W^{\alpha\beta} = 2\varepsilon_l\varepsilon_\nu\left(\left(2W_1 \pm W_3\frac{\varepsilon_l + \varepsilon_\nu}{M}\right)\sin^2\frac{\theta}{2} + W_2\cos^2\frac{\theta}{2}\right). \tag{A.60}$$

We remind that ultrarrelativistic approximation has been used in both neutrino and lepton due to its neglection of mass $m_{\nu,l} \to 0$ compared contribution coming from the rest of terms.

A.4.4 Final results

Being our original objective to compute $|M_{fi}|^2$, we finally get:

$$|M_{fi}|^2 \equiv \frac{\eta_{\alpha\beta}W^{\alpha\beta}}{m_\nu m_l M^2} = \frac{2\varepsilon_l\varepsilon_\nu}{m_l m_\nu M^2}\left(\left(2W_1 \pm W_3\frac{\varepsilon_l + \varepsilon_\nu}{M}\right)\sin^2\frac{\theta}{2} + W_2\cos^2\frac{\theta}{2}\right). \tag{A.61}$$

For completeness, we display here what would be the overall expression if we are not neglecting the lepton mass m_l. Whole calculus can be found in [52].

$$|M_{fi}|^2 = \frac{2\varepsilon_l\varepsilon_\nu}{m_l m_\nu M^2}\left\{2W_1\sin^2\frac{\theta}{2} + W_2\varepsilon_l\cos^2\frac{\theta}{2} \pm W_3\frac{\varepsilon_\nu+\varepsilon_l}{M}\varepsilon_l\sin^2\frac{\theta}{2} + \right.$$
$$\frac{m_l^2}{\varepsilon_l(\varepsilon_l+|\vec{k}_l|)}\left[W_1\cos\theta - \frac{W_2}{2}\cos\theta \pm \frac{W_3}{2}\left(\frac{\varepsilon_\nu+\varepsilon_l}{M}\cos\theta - \frac{\varepsilon_l+|\vec{k}_l|}{M}\right) + \right.$$
$$\left.\left.\frac{W_4}{2}\left(\frac{m_l^2}{M^2}\cos\theta + \frac{2\varepsilon_l(\varepsilon_l+|\vec{k}_l|)}{M^2}\sin^2\frac{\theta}{2}\right) - W_5\frac{\varepsilon_l+|\vec{k}_l|}{2M}\right]\right\}. \tag{A.62}$$

B ENUBET beamline optimisation

B.1 Geant4 simulation results statistics

In the Geant4 implementation of the ENUBET experiment, cascades resulting from the interaction of the proton beam with the target are simulated using FLUKA. This generates a large number of particles in various kinematic conditions. Subsequently, Geant4 simulates the trajectory of these particles to characterise their distribution at different points along the beamline. Of particular interest in this thesis are the entrance and inner wall of the tagger.

The 400 GeV/c proton beam has an intensity of up to 4.5×10^{13} protons per spill, with each spill lasting 4.8 seconds. FLUKA simulates a total of 10^9 pot (corresponding to 0.107 ms), resulting in approximately 1.7×10^{11} simulated particle trajectories. However, running a full simulation to compute the trajectory evolution of each of these products in the beamline is computationally intensive and time-consuming, requiring several days of computation.

For the figures presented in Chapters 5 and 6, a reduced number of simulated events, 2×10^9, was utilised[43]. This decreases the total simulation time to approximately 2.5 hours per run. Despite the lower number of events, the dataset still contains approximately events from 1.18×10^7 pot, ensuring minimal statistical fluctuations while significantly reducing execution time for effective comparison of results from different configurations.

B.2 Role of magnetic fields in momentum particle selection

The objective of producing a lower-energy neutrino beam, as discussed in Section 6.2, involves reducing the momentum selection from the dipoles by decreasing the magnitude of the magnetic field. Since the only force acting on a charged particle is the Lorentz Force, which acts inwards, it results in circular motion. This can be expressed as follows:

$$\vec{F_L} = m\vec{a}_n \longrightarrow vqB = m\frac{v^2}{R}, \longrightarrow R = \frac{qB}{p}, \tag{B.1}$$

where:

- $p = mv$ is the momentum.
- R is the radius of curvature.
- $q = +e$ since only positively charged particles (K^+, π^+) are of interest.
- B is the magnitude of the magnetic field.

[43] This would correspond to simulate approximately 1.3 μs beam time.

Therefore, to ensure that lower-energy particles are equally deviated (i.e., same R), the following relationship holds:

$$R_{8.5} = R_X, \longrightarrow \frac{qB_{8.5}}{p_{8.5}} = \frac{qB_X}{p_X}, \longrightarrow B_X = B_{8.5}\frac{p_X}{p_{8.5}}, \tag{B.2}$$

where the subscripts 8.5 and X refer to scenarios involving momenta of 8.5 GeV and X (the momentum value to be selected), respectively. For the cases of interest in this chapter, momenta of 3.5 GeV and 2.0 GeV are considered.

$$B_{3.5} = B_{8.5}\frac{3.5}{8.5} = 0.4118B_{8.5}, \quad B_{2.0} = B_{8.5}\frac{2.0}{8.5} = 0.2353B_{8.5}. \tag{B.3}$$

Regarding quadrupoles, it can be initially assumed that the same logic applies to determine an appropriate value for the magnetic field, considering the collimation of lower momentum particles. For a charged particle moving along the axis, magnetic fields act in two axes, resulting in Lorentz Forces in the vertical and horizontal directions, as illustrated in Figure **64**. By applying Newton's Second Law, we can derive the following motion equations:

$$m\vec{a} = \vec{F_L} = q\vec{v} \times \vec{B}. \tag{B.4}$$

Assuming motion in three dimensions and a magnetic field in the XZ plane, we can approximate the magnetic field as locally homogeneous in the region near the axis, meaning that B_x and B_z are constant, $B_x = B_z \equiv B$. Developing the cross product, the equations of motion are:

$$ma_x = qv_yB, \quad ma_y = qB(v_z - v_x), \quad ma_z = -qBv_y. \tag{B.5}$$

Introducing the momentum definition $p = mv$, we get:

$$a_x = \frac{qB}{p}vv_y, \quad a_y = \frac{qB}{p}v(v_z - v_x), \quad a_z = -\frac{qB}{p}vv_y. \tag{B.6}$$

As observed, considering lower momentum particles complicates the calculation of the magnetic field needed to achieve the same trajectory, as it now involves v and its components. However, computing the exact value of B under these circumstances is beyond the scope of this thesis. Therefore, it is considered that, to some extent, the ratio B/p is the major contributing factor. Hence, the magnetic field of the quadrupole is adjusted in the same manner as the dipoles based on the results obtained in Section 6.2.

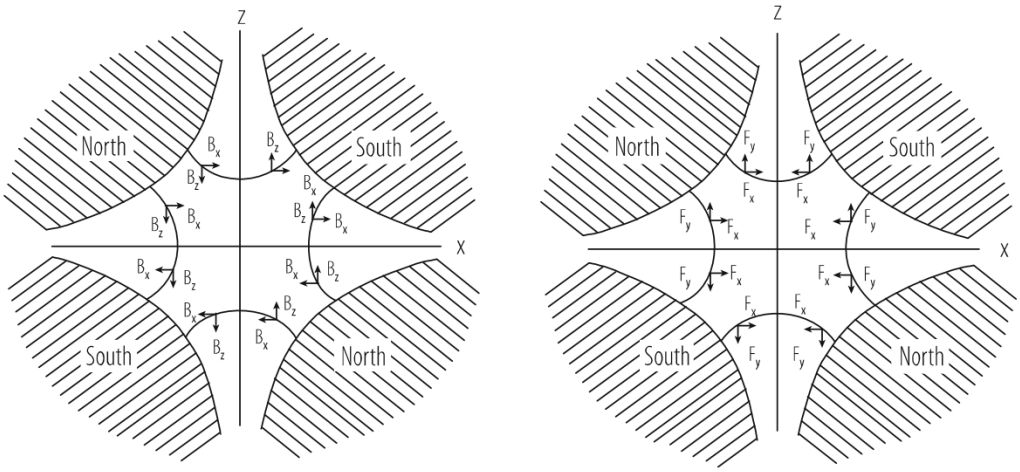

Figure 64: Scheme of magnetic vector field lines and forces acting on charged particles moving inwards in quadrupole magnets [108].

C Monte Carlo generators in neutrino-nucleus interactions

Monte Carlo generators are widely used to simulate complex physical processes using statistical methods. In the context of neutrino-nucleus interactions, these generators are crucial for studying the kinematic outcomes mainly in neutrino production and neutrino oscillation. For a given incident neutrino flux, Monte Carlo generators can predict results based on random samplings through models that incorporate nuclear effects.

This section provides additional details on Monte Carlo generators, focusing on secondary aspects to the main analysis from Part III. However, these supplementary insights lead to a better understanding of the generators employed, especially NEUT and GENIE.

C.1 Comparison between T2K fluxes as input of the Monte Carlo generators

In subsection 4.1, it was presented the 2016 T2K neutrino and antineutrino fluxes that are used as an input in NEUT and GENIE for producing this Thesis results. However, in the T2K website [90] newer data is published, 2020, incorporating an improved simulation with thinner bins. Figure **65** displays both versions for a better comparison. Unfortunately, NEUT is not functional with the new flux yet, so in this Thesis 2016 fluxes have been used.

Since the shape of the flux barely changes from 2016 to 2020 results, the main difference relies on the size of the systematic error associated with the flux. However, in the χ^2 calculation it has not been taken into consideration the flux uncertainty, therefore the employment of the new prediction would not affect significantly in our analysis.

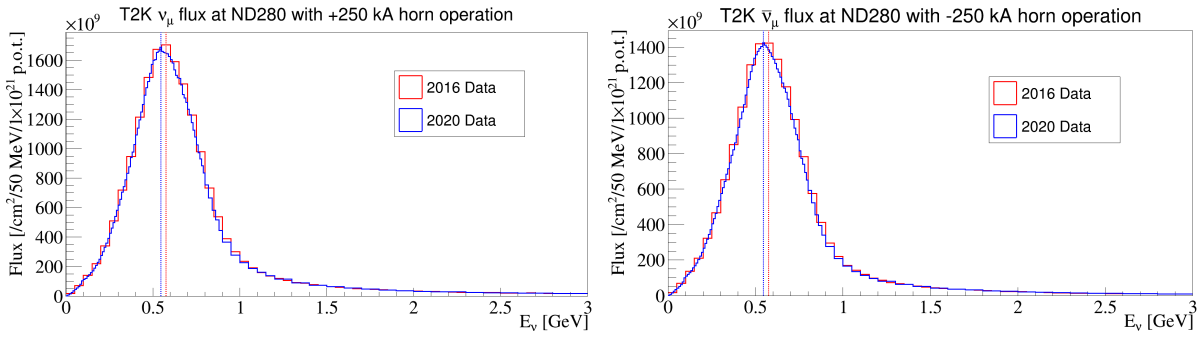

Figure 65: Muon neutrino (top) and antineutrino (bottom) fluxes predicted as a function of the neutrino energy in the T2K near detector published in 2016 (red) and 2020 (blue) with an off-axis set at 2.5^o . The peak of the spectra is remarked with a vertical dashed line, being close to 0.6 GeV, where the oscillation effects are maximum in the path to the far detector.

C.2 Nuclear effects

In this subsection, we list the nuclear effects accounted for in the Monte Carlo generators to provide an overview of the physical phenomena implemented in these tools:

- **Fermi motion**: nucleons are not static within the nucleus; therefore, their momentum distribution must be considered. Figures **23** and **26** from Chapter 3.2 show how this distribution varies depending on the nuclear model employed.
- **Nuclear removal energy**: nucleons are originally bound, requiring part of the incident energy to free them. In Chapter 3.2, this parameter is denoted as E_{shift}. While in the Relativistic Fermi Gas (RFG) model, it is considered a constant; in other models, such as SuSAv2, it depends on the momentum transfer q (see Figure **24**).
- **Final State Interaction (FSI)**: after neutrino scattering, the resulting nucleon can interact multiple times within the nucleus before escaping. These interactions, known as FSI, are modeled through an intranuclear cascade, which determines whether the nucleon interacts and selects the process, such as pion production or elastic scattering. FSI are considered to cease once the nucleon exits a defined interaction range, typically the nucleus.
- **Multi-nucleon interactions**: inside the nucleus, nucleons can interact via strong interactions through virtual mesons exchange (e.g., pions). Neutrino scattering can thus result in the interaction of two bound nucleons, leading to 2p2h (MEC) final states. Figure **16** illustrates the possible Feynman diagrams for these processes.
- **Additional correlations**: spin polarization effects within the nucleus, known as long-range correlations, are significant. Random Phase Approximation (RPA) models these interactions through a potential (e.g., Landau-Migdal potential [109]) to account for these corrections.
- **Pauli blocking**: nucleons, being fermions, are subject to the Pauli exclusion principle, which prevents two fermions from occupying the same quantum state. This results in limited energy levels within the nucleus. In the context of nucleus scattering, this is known as Pauli blocking and it is reflected in the term $\Theta(|\vec{p}_{n,f}| - k_F)$ from Eq. (3.4), indicating that the ejected nucleon cannot have a momentum lower than the Fermi momentum, as the Fermi sphere is already occupied by initial nucleons. As shown in Figure **66**, Pauli blocking plays a significant role at lower transferred energies, as insufficient energy is available to eject the nucleon out of the Fermi sphere.

To sum up, these nuclear effects significantly modify the cross section compared to the free nucleon case, increasing the dimensionality of the problem. This is due to the reduced

kinematic constraints in both the initial and final states, and the altered hadronic final state, as different FSI modes can lead to the same observed final state.

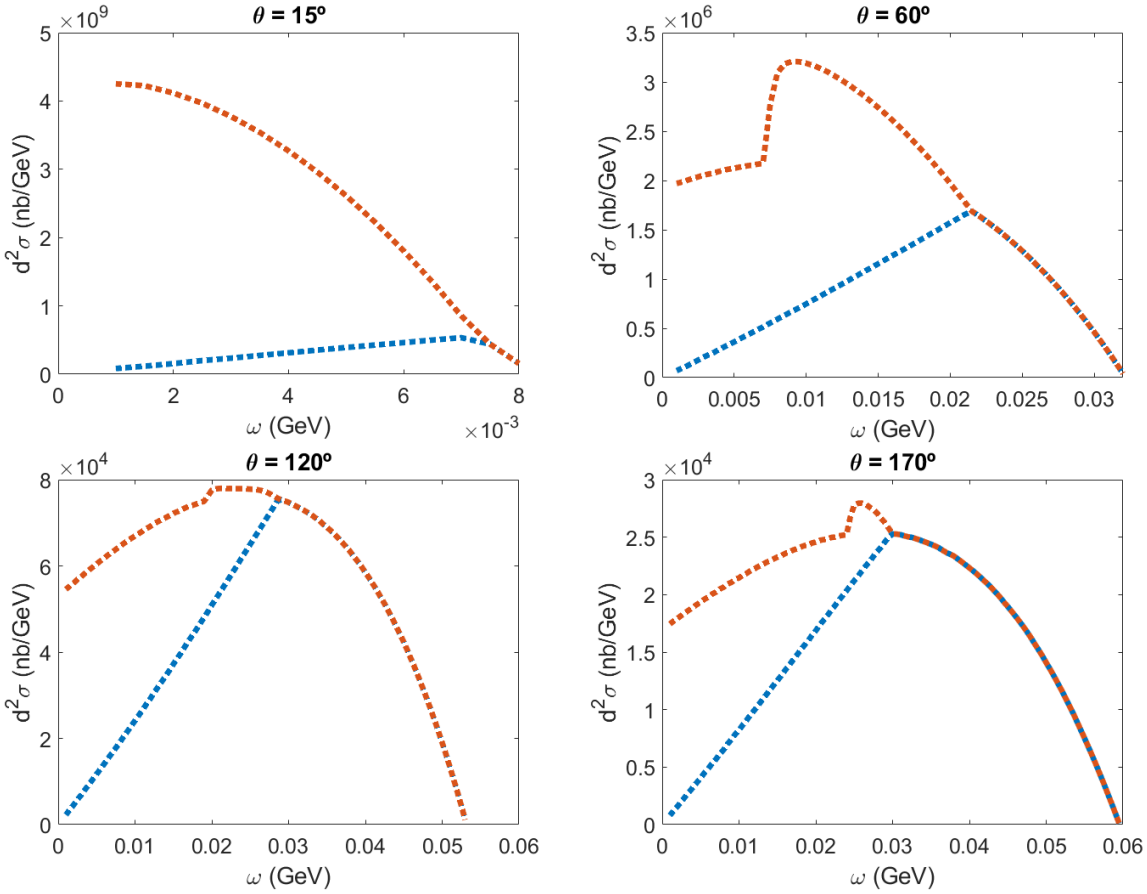

Figure 66: Double differential cross section in $e^- - {}^{40}$Ca scattering under the RFG model for 120 MeV incident energy. Different angles are shown to illustrate the differences between Pauli blocking being on (blue) and off (red). In the forward region, less transferred energy (ω) is needed to eject the nucleon from the Fermi sphere. Figure extracted from one of the author's project works during the Master's program.

C.3 NEUT and GENIE

In recent years, various Monte Carlo generators have been developed in the study of neutrino-nucleus interactions. The main idea is to implement different nuclear models to observe the goodness of these descriptions with respect the experimental data. Given the resource limitations in these generators, theoretical inputs are essential for calculations, such as the hadronic tensor or nuclear effects parameters (Fermi momentum, removal energy, etc.). Ultimately, these Monte Carlo generators aim to accurately compute the kinematics of all final state particles.

This Thesis employs NEUT [82] and GENIE [83], some of the most widely used generators in this field. For experimental analyses, these generators properly achieve the four-momentum characterisation of the final state particles for all interaction channels.

While NEUT focuses more on the experimental needs of Super-K, T2K, and Hyper-K, GENIE aims to provide a universal framework, with a development team independent of the experiments. This is the main reason why NEUT is proprietary software, whereas GENIE is open source. Regarding physics implementations, differences between NEUT and GENIE are primarily found in the FSI cascade and multi-nucleon interactions. More details can be found in [110].

Other generators, such as NuWro [111], AChiLES [112], and GiBUU [113], focus more on theoretical aspects and have fewer developers working on them. Despite this, they are noteworthy for implementing new techniques, such as in FSI, even though they are not as prominent as NEUT or GENIE currently.

D Tools for the T2K statistical analysis

Evaluating the performance of current neutrino generators has involved conducting the corresponding statistical analysis. This section outlines the methodology used in this process, including weighting the cross section to adjust Monte Carlo predictions to the bin size of the experimental data, as well as a review of χ^2 and p-value calculations.

D.1 Weighted cross section

In section 4.2, the Monte Carlo generator models for nuclear dynamics used in the T2K data analysis are explained.

The experimental results are provided as a txt file containing the weighted cross section for various subdivisions of p momentum within each $\cos\theta$ region. In contrast, the output from Monte Carlo generators is a ROOT file containing information on all particles after the scattering, including their kinematics. Therefore, it is necessary to manually adjust the cross section obtained from Monte Carlo simulations to adhere to the same structure. Here, it is commented how this process has been performed.

For a given $\cos\theta$ region and p bin range:

- Identify the amount of muons generated from the desired process (CCQE, MEC, or pion absorption) whose momentum and $\cos\theta$ fall within the selected interval.
- Multiply the total count by a scaling factor $\mathscr{F}$ to relate the number of events to the cross section, where $\mathscr{F} = 9 \times 10^{-45} \frac{\mathrm{cm}^{-2}}{\mathrm{Nucleon} \times \mathrm{MeV}}$.
- Divide by the width of the intervals corresponding to the selected range of $\cos\theta$ and p:

$$\overline{\frac{d^2\sigma}{d\cos\theta dp}} = \frac{\frac{d^2\sigma}{d\cos\theta dp}}{\Delta p \Delta\cos\theta}$$

This process provides us with the Monte Carlo generator result for a single p bin, consistent with the structure of the provided experimental data. Therefore, to generate a plot, this procedure needs to be repeated for each momentum p bin within the selected angular region.

D.2 χ^2, dof and p-values

To assess the agreement of the Monte Carlo generators to T2K experimental data, understanding the parameters χ^2, degrees of freedom (dof), and p-values is crucial. This appendix aims to clarify these concepts to facilitate the statistical analysis of the prediction.

Firstly, the χ^2 parameter measures how well a model reproduces experimental data. A lower absolute value indicates a better correspondence. It is calculated using the observed data values, their uncertainties (typically from the covariance matrix), and the predicted values from the model.

In the T2K website [114], uncertainties are encapsulated in the covariance matrix C. This square matrix quantifies correlations between different data points within an angular dataset. It accounts for various sources of error such as systematic effects and flux uncertainties in the T2K experiment.

In the context of this Thesis, for a given $\cos\theta$ region that contains N momentum p bins, χ^2 is evaluated as follows:

$$\chi^2 = \sum_i^N \sum_j^N \left[\overline{\left.\frac{d^2\sigma}{d\cos\theta dp}\right|_{\text{model}}} - \overline{\left.\frac{d^2\sigma}{d\cos\theta dp}\right|_{\text{data}}} \right]_i \times [C^{-1}]^{i,j} \times \left[\overline{\left.\frac{d^2\sigma}{d\cos\theta dp}\right|_{\text{model}}} - \overline{\left.\frac{d^2\sigma}{d\cos\theta dp}\right|_{\text{data}}} \right]_j , \tag{D.1}$$

with $\overline{\frac{d^2\sigma}{d\cos\theta dp}}$ denoting the weighted double differential cross section, the subindexes model and data refer to the Monte Carlo predictions and the experimental data respectively, and C^{-1} is the inverse of the covariance matrix.

Degrees of freedom (dof) in statistical terms refer to the number of independent observations in a sample that can vary freely. It is defined as:

$$\text{dof} = N - M, \tag{D.2}$$

where N and M are number of data points and the parameters estimated respectively. In our case, N, which is the number of momentum bins found for a certain angular region, is the number of degrees of freedom since no parameter is computed from these experimental bins dof$= N$.

The p-value, ranging from 0 to 1, indicates the probability that the observed data deviates from the predicted results given a certain number of degrees of freedom. A low p-value suggests a significant deviation, potentially indicating a rejection of the model, while a p-value close to 1 indicates good agreement between data and model predictions. In our analysis, p-values are computed using ROOT based on the corresponding χ^2 and degrees of freedom.

E T2K graphical results and χ^2 values

This appendix provides graphical comparisons of Monte Carlo predicted results with experimental measurements of the neutrino and antineutrino double differential cross section. Additionally, it highlights specific intermediate p bins that significantly increased the χ^2 values upon their inclusion, serving as a complementary observation to the main analysis.

E.1 Monte Carlo results vs experimental data

Figures 67 and 68 display the predicted Monte Carlo results compared with the experimental data across the nine angular regions for neutrinos and antineutrinos respectively. The legend includes the χ^2 values alongside the nuclear models implemented for Method 1 and Method 2, as well as the corresponding degrees of freedom.

To ease readability, the last p bin is omitted in the following figures. However, it is included in the calculations performed using Method 1.

E.2 Momentum bins overestimating χ^2

In the calculations of χ^2, it was displayed after each iteration the summation of χ^2, noticing that certain momentum bins significantly increased the χ^2 value compared to the rest of the bins for all four Monte Carlo models considered. As a complementary observation to the main analysis presented in Part III, this subsection highlights which specific bins exhibit this behavior.

For neutrinos:

- $\cos\theta_l \in [0.80, 0.85]$, $p \in [600, 800]$ MeV.
- $\cos\theta_l \in [0.85, 0.90]$, $p \in [600, 800]$ MeV.
- $\cos\theta_l \in [0.90, 0.94]$, $p \in [600, 800]$ MeV.
- $\cos\theta_l \in [0.94, 0.98]$, $p \in [600, 800]$ MeV.
- $\cos\theta_l \in [0.98, 1.00]$, $p \in [500, 700]$ MeV and $p \in [2000, 3000]$ MeV.

For antineutrinos:

- $\cos\theta_l \in [0.85, 0.90]$, $p \in [400, 500]$ MeV.
- $\cos\theta_l \in [0.94, 0.98]$, $p \in [600, 800]$ MeV.
- $\cos\theta_l \in [0.98, 1.00]$, $p \in [500, 700]$ MeV and $p \in [2000, 3000]$ MeV.

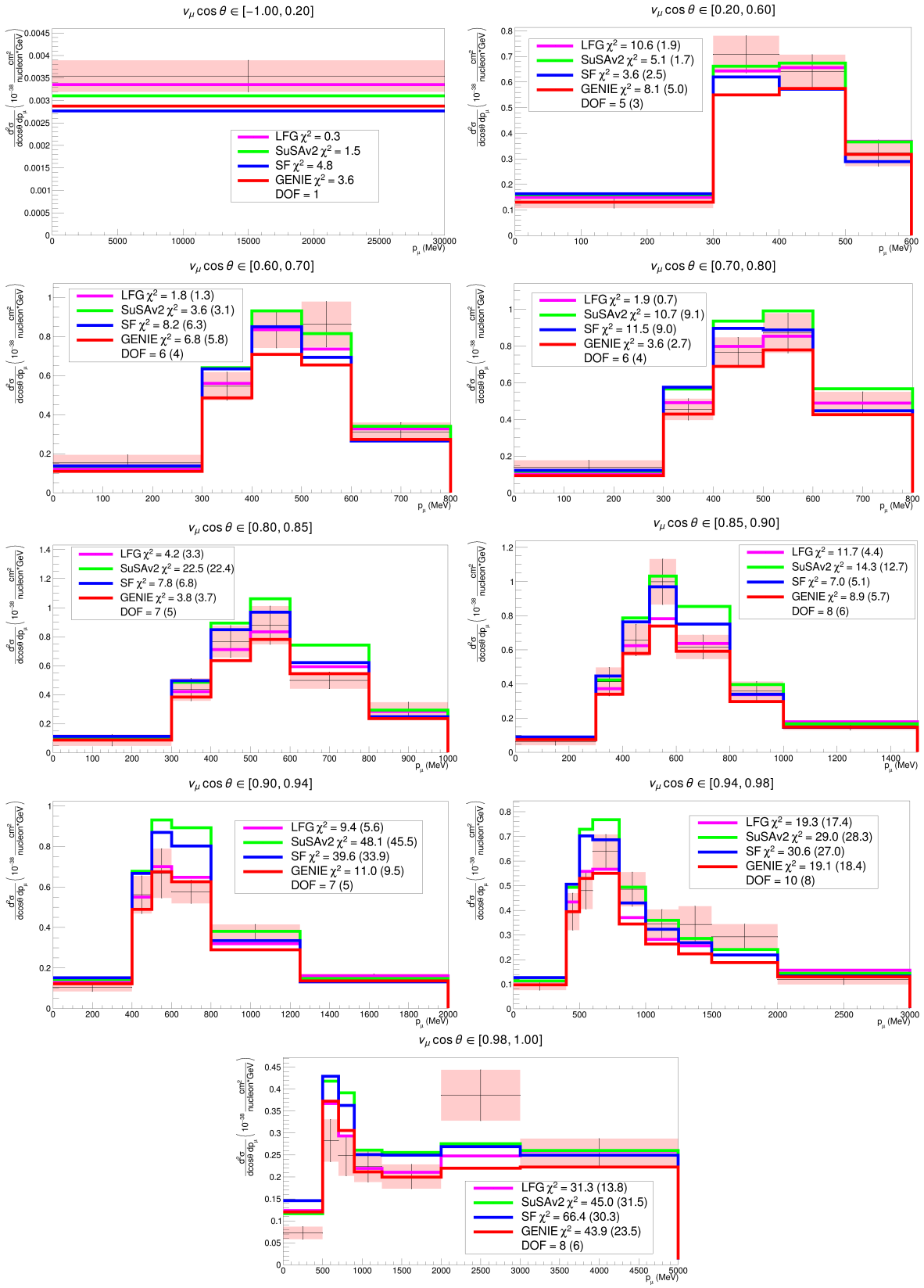

Figure 67: Neutrino double differential cross section comparing Monte Carlo generated results from SF, LFG, SuSAv2, and DUNE with experimental measurements (black dots with pink shading to denote associated uncertainty). The legend shows the χ^2 values of each prediction using Method 1, with Method 2 values in brackets. Degrees of freedom are also indicated.

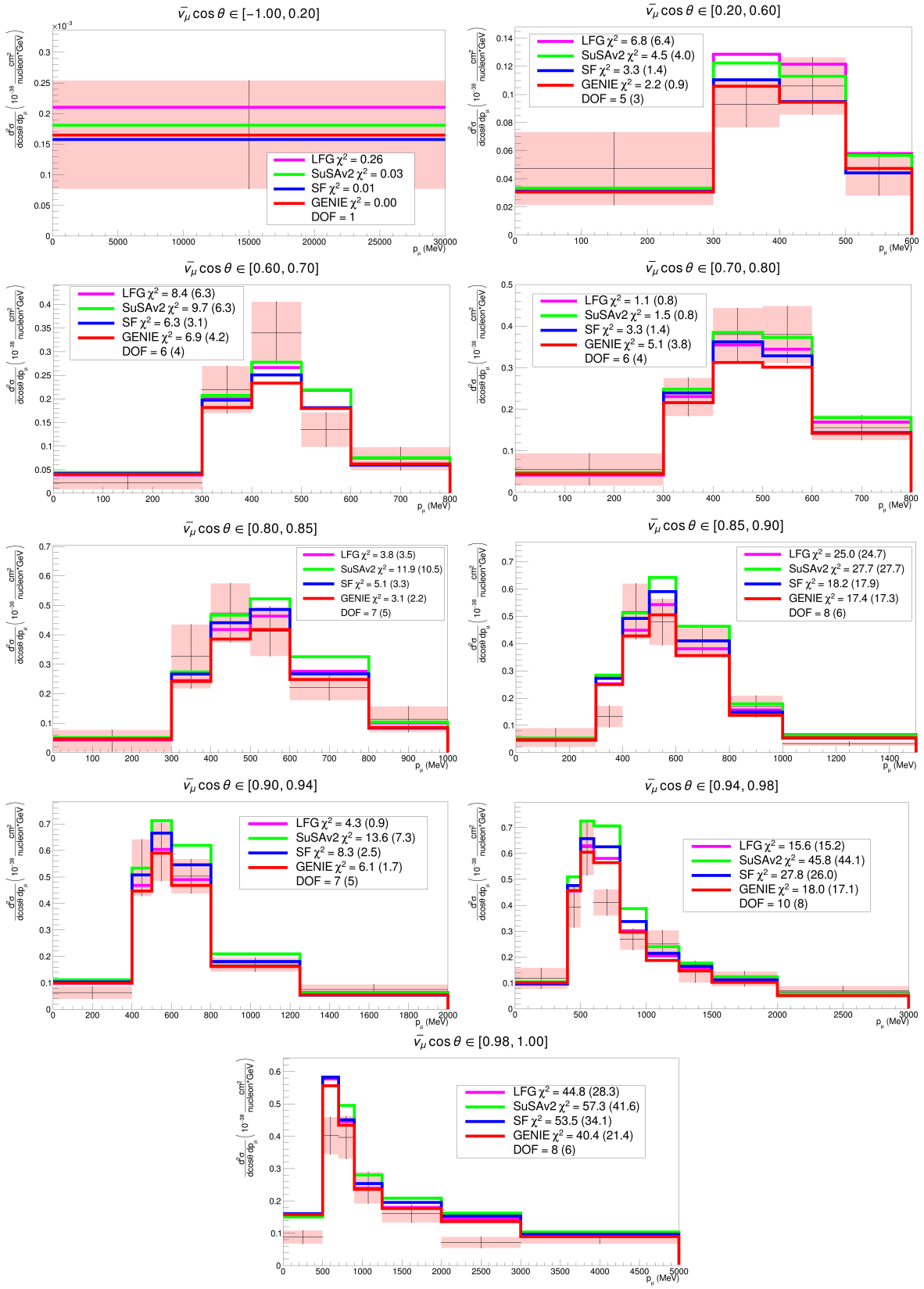

Figure 68: Antineutrino double differential cross section comparing Monte Carlo generated results from SF, LFG, SuSAv2, and DUNE with experimental measurements (black dots with pink shading to denote associated uncertainty). The legend shows the χ^2 values of each prediction using Method 1, with Method 2 values in brackets. Degrees of freedom are also indicated.

Looking at the relative error in each bin displayed in the Figure **31**, the aforementioned p bins correspond to regions where the fractional error is minimal. Therefore, an analysis considering $\Delta\chi^2$ versus the excluded p momentum bin for each of the aforementioned angular regions is recommended to draw further conclusions about the impact of these bins on the performance of the Monte Carlo generators employed in this Thesis.

References

[1] David Griffiths, *Introduction to Elementary Particles*. WILEY-VCH, 1987, Second Edition, ISBN: 9783527618460, [Online]. Available: {https://onlinelibrary.wiley.com/doi/book/10.1002/9783527618460}.

[2] L. Meitner, "Über die entstehung der β-strahl-spektren radioaktiver substanzen," *Zeitschrift FüR Physik.*, vol. 9, pp. 131–144, 1922, DOI: 10.1007/Bf01326962.

[3] L. Meitner, "Über die β-strahl-spektra und ihren zusammenhang mit der γ-strahlung," *Zeitschrift FüR Physik.*, vol. 11, pp. 35–54, 1922, DOI: 10.1007/Bf01328399.

[4] C. D. Ellis and W. A. Wooster, "The average energy of disintegration of radium e," *Proceedings of the Royal Society London A*, vol. 117, p. 168, 1927, DOI: https://doi.org/10.1098/rspa.1927.0168.

[5] [Online]. Available: https://www.cyberphysics.co.uk/topics/particle/feynman.htm.

[6] C. Cowan *et al.*, "Detection of the free neutrino: A confirmation," *Science*, vol. 11, pp. 103–104, 3212 1956, DOI: 10.1126/Science.124.3212.103.

[7] F.Gatti and P. C.-O. Ranitzsch, *Recent m_ν constraints and tritium experiments*, Nu Telescope, 2015, [Online]. Available: https://www.roma1.infn.it/~rescigno/slides2015/NeutrinoMass_ReinesCowan.pdf.

[8] G. Danby, J.-M. Gaillard, K. Goulianos, *et al.*, "Observation of high-energy neutrino reactions and the existence of two kinds of neutrinos," *Phys. Rev. Lett.*, vol. 9, pp. 36–44, 1 1962, DOI: 10.1103/PhysRevLett.9.36.

[9] K. Kodama, N. Ushida, C. Andreopoulos, *et al.*, "Observation of tau neutrino interactions," *Physics Letters B*, vol. 504, no. 3, pp. 218–224, 2001, ISSN: 0370-2693, DOI: https://doi.org/10.1016/S0370-2693(01)00307-0.

[10] E. Akhmedov, P. Lipari, and M. Lusignoli, "Matter effects in atmospheric neutrino oscillations," *Physics Letters B*, vol. 300, no. 1, pp. 128–136, 1993, ISSN: 0370-2693, DOI: https://doi.org/10.1016/0370-2693(93)90759-B.

[11] Q. Liu and A. Smirnov, "Neutrino mass spectrum with $\nu_\mu \to \nu_s$ oscillations of atmospheric neutrinos," *Nuclear Physics B*, vol. 524, no. 3, pp. 505–523, 1998, ISSN: 0550-3213, DOI: https://doi.org/10.1016/S0550-3213(98)00269-7.

[12] B. Dasgupta and J. Kopp, "Sterile neutrinos," *Physics Reports*, vol. 928, pp. 1–63, 2021, Sterile neutrinos, ISSN: 0370-1573, DOI: https://doi.org/10.1016/j.physrep.2021.06.002.

[13] A. Giuliani and A. Poves, "Neutrinoless double-beta decay," 2012, Article ID 857016, DOI: https://doi.org/10.1155/2012/857016.

[14] M. Tanabashi, K. Hagiwara, K. Hikasa, *et al.*, "Review of particle physics," *Phys. Rev. D*, vol. 98, p. 030 001, 3 2018, DOI: 10.1103/PhysRevD.98.030001.

[15] L. Alvarez-Ruso, M. Sajjad Athar, M. Barbaro, *et al.*, "Nustec1 1neutrino scattering theory experiment collaboration http://nustec.fnal.gov. white paper: Status and challenges of neutrino–nucleus scattering," *Progress in Particle and Nuclear Physics*, vol. 100, pp. 1–68, 2018, ISSN: 0146-6410, DOI: https://doi.org/10.1016/j.ppnp.2018.01.006.

[16] T. Katori and M. Martini, "Neutrino-nucleus cross sections for oscillation experiments," 2016, [Online]. Available: https://iopscience.iop.org/article/10.1088/1361-6471/aa8bf7.

[17] M. Drewes, "The phenomenology of right handed neutrinos," *International Journal of Modern Physics E*, vol. 22, no. 08, p. 1 330 019, 2013, DOI: 10.1142/S0218301313300191.

[18] X. Qian and P. Vogel, "Neutrino mass hierarchy," *Progress in Particle and Nuclear Physics*, vol. 83, pp. 1–30, 2015, ISSN: 0146-6410, DOI: https://doi.org/10.1016/j.ppnp.2015.05.002.

[19] F. Simpson, R. Jimenez, C. Pena-Garay, and L. Verde, "Strong bayesian evidence for the normal neutrino hierarchy," *Journal of Cosmology and Astroparticle Physics*, vol. 2017, no. 06, p. 029, 2017, DOI: 10.1088/1475-7516/2017/06/029.

[20] R. Jimenez, C. Pena-Garay, K. Short, F. Simpson, and L. Verde, "Neutrino masses and mass hierarchy: Evidence for the normal hierarchy," *Journal of Cosmology and Astroparticle Physics*, vol. 2022, no. 09, p. 006, 2022, DOI: 10.1088/1475-7516/2022/09/006.

[21] H. A. Bethe and R. E. Marshak, "The physics of stellar interiors and stellar evolution," *Reports on Progress in Physics*, vol. 6, no. 1, p. 1, 1939, DOI: 10.1088/0034-4885/6/1/301.

[22] J. N. Bahcall and R. D. Jr., "Solar neutrinos: A scientific puzzle," *Science*, vol. 191, pp. 264–267, 4224 1976, DOI: 10.1126/science.191.4224.264.

[23] S. Turck-Chièze and S. Couvidat, "Solar neutrinos, helioseismology and the solar internal dynamics," *Reports on Progress in Physics*, vol. 74, no. 8, p. 086 901, 2011, DOI: 10.1088/0034-4885/74/8/086901.

[24] B. Pontecorvo, "Mesonium and anti-mesonium," *Sov. Phys. JETP*, vol. 6, p. 429, 1957.

[25] Y. Fukuda *et al.*, "Evidence for Oscillation of Atmospheric Neutrinos," *Phys. Rev. Lett.*, vol. 81, p. 1562, 1998, Super-Kamiokande Collaboration, DOI: https://doi.org/10.1103/PhysRevLett.81.1562.

[26] T. Kajita, "Discovery of atmospheric neutrino oscillations," *Ann. Phys. (Berlin)*, vol. 528, p. 459, 2016, Nobel Lecture, DOI: https://doi.org/10.1002/andp.201600086.

[27] C. Giganti *et al.*, "Neutrino oscillations: the rise of the PMNS paradigm," *Progress in Particle and Nuclear Physics*, vol. 98, p. 54, 2018, DOI: https://doi.org/10.1016/j.ppnp.2017.10.001.

[28] *Short and long baseline neutrino experiments*, VII School of Non-Accelerator Astroparticle Physics, 2004, [Online]. Available: https://indico.ictp.it/event/a0355/session/6/contribution/4/material/0/0.pdf.

[29] G. J. Feldman, "History of long-baseline accelerator neutrino experiments," 2019, [Online]. Available: https://arxiv.org/abs/1901.09431.

[30] B. Szczerbinska, "Long Baseline Neutrino Experiment," *Acta Physica Polonica B*, 7 2010, [Online]. Available: https://s3.cern.ch/inspire-prod-files-5/587a435511f4e6951b77c8eb64159e2a.

[31] S. Cao, "Long Baseline Neutrino Oscillation Results (T2K and NOvA)," *arXiv*, 2023, T2K collaboration, [Online]. Available: https://arxiv.org/pdf/2310.09855.pdf.

[32] D. Attié, M. Batkiewicz-Kwasniak, J. Boix, *et al.*, "Performances of a resistive micromegas module for the time projection chambers of the t2k near detector upgrade," *Nuclear Instruments and Methods in Physics Research Section A: Accelerators, Spectrometers, Detectors and Associated Equipment*, vol. 957, p. 163 286, 2020, ISSN: 0168-9002, DOI: https://doi.org/10.1016/j.nima.2019.163286.

[33] A. Korzenev, C. Betancourt, A. Blondel, *et al.*, "Plastic scintillator detector with the readout based on an array of large-area sipms for the nd280/t2k upgrade and ship experiments," DOI: 10.7566/JPSCP.27.011005.

[34] S. Dolan, V. Q. Nguyen, A. Blanchet, *et al.*, "Sensitivity of the upgraded t2k near detector to constrain neutrino and antineutrino interactions with no mesons in the final state by exploiting nucleon-lepton correlations," *Phys. Rev. D*, vol. 105, p. 032 010, 3 2022, DOI: 10.1103/PhysRevD.105.032010.

[35] M. J. Frank, "Latest Three-Flavor Neutrino Oscillation Results from NOvA," *PoS*, vol. EPS-HEP2023, p. 152, 2023, DOI: 10.22323/1.449.0152.

[36] S. Fukasawa, M. Ghosh, and O. Yasuda, "Complementarity between hyperkamiokande and dune in determining neutrino oscillation parameters," *Nuclear Physics B*, vol. 918, pp. 337–357, 2017, ISSN: 0550-3213, DOI: https://doi.org/10.1016/j.nuclphysb.2017.02.008.

[37] L.-I. Munteanu, "Long-baseline neutrino oscillation sensitivities with hyper-kamiokande," *22nd International Workshop on Neutrinos from Accelerators*, p. 056, 2022, Cagliari, Italy, [Online]. Available: https://hal.science/hal-03632744.

[38] A. Falcone, "Deep underground neutrino experiment: Dune," *Nuclear Instruments and Methods in Physics Research Section A: Accelerators, Spectrometers, Detectors and Associated Equipment*, vol. 1041, p. 167 217, 2022, ISSN: 0168-9002, DOI: https://doi.org/10.1016/j.nima.2022.167217.

[39] A. A. Abud *et al.*, "Snowmass neutrino frontier: Dune physics summary," 2022, [Online]. Available: https://arxiv.org/abs/2203.06100.

[40] Francis Halzen and Alan D. Martin, *Quarks and leptons: An Introductory Course in Modern Particle Physics*. John Wiley and Sons, 1984, ISBN: 978-0-471-88741-6, [Online]. Available: {https://www.wiley.com/en-gb/Quarks+and+Leptones%3A+An+Introductory+Course+in+Modern+Particle+Physics-p-9780471887416}.

[41] J. Amaro *et al.*, "Using electron scattering superscaling to predict charge-changing neutrino cross sections in nuclei," *Phys. Rev. C*, vol. 71, 015501 2005, DOI: 10.1103/PhysRevC.71.015501.

[42] N. Cabibbo, "Unitary symmetry and leptonic decays," *Phys. Rev. Let.*, vol. 10, p. 531, 1963, DOI: https://doi.org/10.1103/PhysRevLett.10.531.

[43] *Hadron matrix elements. low-energy qcd phenomenology*, [Online]. Available: http://cftp.ist.utl.pt/~gernot.eichmann/2020-QCDHP/QCD-hadron-matrix-elements.pdf.

[44] C. Adamuscin *et al.*, "Two-component model for the axial form factor of the nucleon.," *Phys. Rev. C*, vol. 78, 035201 2008, DOI: https://doi.org/10.1103/PhysRevC.78.035201.

[45] W. A. Mann *et al.*, "Study of the reaction $\nu + n \to \mu^- + p$," *Phys. Rev. Lett.*, vol. 31, p. 844, 1973, DOI: https://doi.org/10.1103/PhysRevLett.31.844.

[46] S. J. Barish *et al.*, "Study of neutrino interactions in hydrogen and deuterium: Description of the experiment and study of the reaction $\nu + d \to \mu^- + p + p_s$," *Phys. Rev. D*, vol. 16, 3103 1977, DOI: https://doi.org/10.1103/PhysRevD.16.3103.

[47] N. J. Baker *et al.*, "Quasielastic neutrino scattering: A measurement of the weak nucleon axial-vector form factor," *Phys. Rev. D*, vol. 23, 2499 1981, DOI: https://doi.org/10.1103/PhysRevD.23.2499.

[48] S. Bonetti *et al.*, "Study of quasielastic reactions of neutrino and anti-neutrino in gargamelle," *Nuovo Cimento*, vol. 38, pp. 260–270, 1977, DOI: https://doi.org/10.17182/hepdata.37598.

[49] M. Pohl *et al.*, "Experimental study of the reaction $\mu + n \to \mu^- + p$," *Nuovo Cimento*, vol. 26, pp. 332–336, 1979, DOI: https://doi.org/10.1007/BF02746631.

[50] R. Gonzalez-Jimenez, N. Jachowicz, A. Nikolakopoulos, *et al.*, "Modeling neutrino-nucleus interaction at intermediate energies," *PoS*, vol. NuFact2017, p. 072, 2018, DOI: 10.22323/1.295.0072.

[51] B. I. S. van der Ventel and J. Piekarewicz, "Strange-quark contribution to the ratio of neutral- to charged-current cross sections in neutrino-nucleus scattering," *Phys. Rev. C*, vol. 73, p. 501, 2005, DOI: 10.1103/PhysRevC.73.025501.

[52] G. Megías, "Charged-current neutrino interactions with nucleons and nuclei at intermediate energies.," 2017, PhD in Neutrino Physics.

[53] I. R. Simo, J. E. Amaro, M. B. Barbaro, A. D. Pace, J. A. Caballero, and T. W. Donnelly, "Relativistic model of 2p-2h meson exchange currents in (anti)neutrino scattering," *Journal of Physics G: Nuclear and Particle Physics*, vol. 44, no. 6, p. 065 105, 2017, DOI: 10.1088/1361-6471/aa6a06.

[54] T. Leitner, O. Lalakulich, O. Buss, U. Mosel, and L. Alvarez-Ruso, "Pion production in neutrino interactions with nuclei," *AIP Conference Proceedings*, vol. 1222, no. 1, pp. 212–221, Mar. 2010, ISSN: 0094-243X, DOI: 10.1063/1.3399298.

[55] J. Nieves, J. E. Amaro, and M. Valverde, "Inclusive quasielastic charged-current neutrino-nucleus reactions," *Phys. Rev. C*, vol. 70, p. 055 503, 5 2004, DOI: 10.1103/PhysRevC.70.055503.

[56] G. D. Megias, J. E. Amaro, M. B. Barbaro, J. A. Caballero, T. W. Donnelly, and I. R. Simo, "Charged-current neutrino-nucleus reactions within the superscaling meson-exchange current approach," *Phys. Rev. D*, vol. 94, p. 093 004, 9 2016, DOI: 10.1103/PhysRevD.94.093004.

[57] J. Caballero *et al.*, "Neutrino-nucleus scattering in the susa model," *Eur. Phys. J Spec. Top.*, vol. 230, 4321–4338, 2021, DOI: https://doi.org/10.1140/epjs/s11734-021-00289-5.

[58] J. I. Friedman and H. W. Kendall, "Deep inelastic electron scattering," *Annu. Rev. Nucl. Part. Sci.*, vol. 22, 5526 1972, DOI: https://doi.org/10.1146/annurev.ns.22.120172.001223.

[59] D. Day *et al.*, "Scaling in inclusive electron-nucleus scattering," *Annu. Rev. Nucl. Part. Sci.*, vol. 40, pp. 357–409, 1990, DOI: https://doi.org/10.1146/annurev.ns.40.120190.002041.

[60] C. Maieron, T. W. Donnelly, and I. Sick, "Extended superscaling of electron scattering from nuclei," *Phys. Rev. C*, vol. 65, p. 025 502, 2 2002, DOI: 10.1103/PhysRevC.65.025502.

[61] W. M. Alberico, A. Molinari, T. W. Donnelly, E. L. Kronenberg, and J. W. Van Orden, "Scaling in electron scattering from a relativistic fermi gas," *Phys. Rev. C*, vol. 38, pp. 1801–1810, 4 1988, DOI: 10.1103/PhysRevC.38.1801.

[62] J. E. Amaro, M. B. Barbaro, J. A. Caballero, R González-Jiménez, G. D. Megias, and I. R. Simo, "Electron- versus neutrino-nucleus scattering," *Journal of Physics G: Nuclear and Particle Physics*, vol. 47, no. 12, p. 124 001, 2020, DOI: 10.1088/1361-6471/abb128.

[63] A. Thomas and W. Weise, "Models of the nucleon," pp. 203–246, 2001, DOI: https://doi.org/10.1002/352760314X.ch8.

[64] J. A. Caballero, J. E. Amaro, M. B. Barbaro, T. W. Donnelly, C. Maieron, and J. M. Udias, "Superscaling in charged current neutrino quasielastic scattering in the relativistic impulse approximation," *Phys. Rev. Lett.*, vol. 95, p. 252 502, 25 2005, DOI: 10.1103/PhysRevLett.95.252502.

[65] R. González-Jiménez, G. D. Megias, M. B. Barbaro, J. A. Caballero, and T. W. Donnelly, "Extensions of superscaling from relativistic mean field theory: The susav2 model," *Phys. Rev. C*, vol. 90, p. 035 501, 3 2014, DOI: 10.1103/PhysRevC.90.035501.

[66] J. A. Caballero, "General study of superscaling in quasielastic (e, e') and (ν, μ) reactions using the relativistic impulse approximation," *Phys. Rev. C*, vol. 74, p. 015 502, 1 2006, DOI: 10.1103/PhysRevC.74.015502.

[67] J. Jourdan, "Quasi-elastic response functions. the coulomb sum revisited," *Nuclear Physics A*, vol. 603, no. 2, pp. 117–160, 1996, ISSN: 0375-9474, DOI: https://doi.org/10.1016/0375-9474(96)00143-1.

[68] C. E. Patrick, "Theory of quasi-elastic neutrino scattering on nuclei," in *Measurement of the Antineutrino Double-Differential Charged-Current Quasi-Elastic Scattering Cross Section at MINERvA*. Cham: Springer International Publishing, 2018, pp. 15–46, ISBN: 978-3-319-69087-2, DOI: 10.1007/978-3-319-69087-2_2.

[69] L Alvarez-Ruso, Y Hayato, and J Nieves, "Progress and open questions in the physics of neutrino cross sections at intermediate energies," *New Journal of Physics*, vol. 16, no. 7, p. 075 015, 2014, DOI: 10.1088/1367-2630/16/7/075015.

[70] P. Ring, "Relativistic mean field theory in finite nuclei," *Progress in Particle and Nuclear Physics*, vol. 37, pp. 193–263, 1996, ISSN: 0146-6410, DOI: https://doi.org/10.1016/0146-6410(96)00054-3.

[71] J. Caballero, T. Donnelly, E. Moya de Guerra, and J. Udías, "Analysis of factorization in (e,ep) reactions: A survey of the relativistic plane wave impulse approximation," *Nuclear Physics A*, vol. 632, no. 3, pp. 323–362, 1998, ISSN: 0375-9474, DOI: https://doi.org/10.1016/S0375-9474(97)00817-8.

[72] O. Benhar, A. Fabrocini, S. Fantoni, and I. Sick, "Spectral function of finite nuclei and scattering of gev electrons," *Nuclear Physics A*, vol. 579, no. 3, pp. 493–517, 1994, ISSN: 0375-9474, DOI: https://doi.org/10.1016/0375-9474(94)90920-2.

[73] J. A. Caballero, M. B. Barbaro, A. N. Antonov, M. V. Ivanov, and T. W. Donnelly, "Scaling function and nucleon momentum distribution," *Phys. Rev. C*, vol. 81, p. 055 502, 5 2010, DOI: 10.1103/PhysRevC.81.055502.

[74] O. Benhar, A. Fabrocini, S. Fantoni, G. A. Miller, V. R. Pandharipande, and I. Sick, "Scattering of gev electrons by nuclear matter," *Phys. Rev. C*, vol. 44, pp. 2328–2342, 6 1991, DOI: 10.1103/PhysRevC.44.2328.

[75] O. Benhar and D. Meloni, "Total neutrino and antineutrino nuclear cross sections around 1 gev," *Nuclear Physics A*, vol. 789, no. 1, pp. 379–402, 2007, ISSN: 0375-9474, DOI: https://doi.org/10.1016/j.nuclphysa.2007.02.015.

[76] K. Abe *et al.*, "Constraint on the matter–antimatter symmetry-violating phase in neutrino oscillations," *Nature*, vol. 580, 2020, The T2K Collaboration, DOI: https://doi.org/10.1038/s41586-020-2177-0.

[77] *T2k website - publications: Cross-sections*, [Online]. Available: https://t2k-experiment.org/publication_category/xsec/.

[78] K. Abe *et al.*, "First combined measurement of the muon neutrino and antineutrino charged-current cross section without pions in the final state at t2k," *Phys. Rev. D*, vol. 101, p. 112 001, 11 2020, DOI: 10.1103/PhysRevD.101.112001.

[79] K. Abe *et al.*, "Simultaneous measurement of the muon neutrino charged-current cross section on oxygen and carbon without pions in the final state at t2k," *Phys. Rev. D*, vol. 101, p. 112 004, 11 2020, DOI: 10.1103/PhysRevD.101.112004.

[80] K. Abe *et al.*, "Measurement of the charged-current electron (anti-)neutrino inclusive cross-sections at the t2k off-axis near detector nd280," *J. High Energ. Phys.*, vol. 2020, 114 2020, The T2K collaboration, DOI: https://doi.org/10.1007/JHEP10(2020)114.

[81] K. Abe *et al.*, "Measurement of the muon neutrino charged-current single π^+ production on hydrocarbon using the t2k off-axis near detector nd280," *Phys. Rev. D*, vol. 101, p. 012 007, 1 2020, DOI: 10.1103/PhysRevD.101.012007.

[82] Y. Hayato, "Neut," *Nuclear Physics B - Proceedings Supplements*, vol. 112, no. 1, pp. 171–176, 2002, ISSN: 0920-5632, DOI: https://doi.org/10.1016/S0920-5632(02)01759-0.

[83] [Online]. Available: https://github.com/GENIE-MC.

[84] J. M. Franco-Patino, A. N. Gacino-Olmedo, J. Gonzalez-Rosa, *et al.*, "Combined analysis of neutrino and antineutrino charged current inclusive interactions," *Symmetry*, vol. 16, no. 5, 2024, ISSN: 2073-8994, DOI: 10.3390/sym16050592.

[85] [Online]. Available: http://www.fluka.org/content/manuals/FM.pdf.

[86] [Online]. Available: https://cds.cern.ch/record/1119728/?ln=en.

[87] K. Abe *et al.*, "T2k neutrino flux prediction," *Phys. Rev. D*, vol. 87, p. 012 001, 1 2013, DOI: 10.1103/PhysRevD.87.012001.

[88] S. Ilieva, "Hadron production measurements for improving neutrino flux predictions with the na61/shine spectrometer," pp. 360–362, DOI: 10.1142/9789811233913_0065.

[89] K. Abe *et al.*, "Measurements of neutrino oscillation in appearance and disappearance channels by the t2k experiment with 6.6×10^{20} protons on target," *Phys. Rev. D*, vol. 91, p. 072 010, 7 2015, DOI: 10.1103/PhysRevD.91.072010.

[90] [Online]. Available: https://t2k-experiment.org/result_category/flux/.

[91] D. Douqa and on behalf of the T2K ND280 Upgrade group, "The superfgd for the t2k near detector upgrade," *Journal of Physics: Conference Series*, vol. 1690, no. 1, p. 012 070, 2020, DOI: 10.1088/1742-6596/1690/1/012070.

[92] K. Abe *et al.*, "T2k nd280 upgrade – technical design report," 2020, [Online]. Available: https://arxiv.org/abs/1901.03750.

[93] [Online]. Available: https://www.pd.infn.it/eng/enubet/.

[94] A. Longhin, G. Ballerini, A. Berra, *et al.*, "High precision measurements of neutrino fluxes with ENUBET," *PoS*, vol. NEUTEL2017, p. 050, 2018, DOI: 10.22323/1.307.0050.

[95] A. Meregaglia, "Enubet: Enhanced neutrino beams from kaon tagging," *Journal of Instrumentation*, vol. 11, no. 12, p. C12040, 2016, DOI: 10.1088/1748-0221/11/12/C12040.

[96] F. Acerbi *et al.*, "Design and performance of the enubet monitored neutrino beam," *Eur. Phys. J. C*, vol. 83, 964 2023, DOI: https://doi.org/10.1140/epjc/s10052-023-12116-3.

[97] G. Ballerini, A. Berra, R. Boanta, *et al.*, "Testbeam performance of a shashlik calorimeter with fine-grained longitudinal segmentation," *Journal of Instrumentation*, vol. 13, no. 01, P01028, 2018, DOI: 10.1088/1748-0221/13/01/P01028.

[98] F. Acerbi, G. Ballerini, A. Berra, *et al.*, "Irradiation and performance of rgb-hd silicon photomultipliers for calorimetric applications," *Journal of Instrumentation*, vol. 14, no. 02, P02029, 2019, DOI: 10.1088/1748-0221/14/02/P02029.

[99] F. Acerbi, M. Bonesini, F. Bramati, *et al.*, "The enubet positron tagger prototype: Construction and testbeam performance," *Journal of Instrumentation*, vol. 15, no. 08, P08001, 2020, DOI: 10.1088/1748-0221/15/08/P08001.

[100] A. Longhin and F. Terranova, "Enhanced neutrino beams from kaon tagging (enubet)," 2022, [Online]. Available: https://arxiv.org/abs/2203.08319.

[101] L. A. Ruso, T. Alves, S. Boyd, *et al.*, "Neutrinos from stored muons (nustorm)," 2022, [Online]. Available: https://arxiv.org/abs/2203.07545.

[102] A. Branca, G. Brunetti, A. Longhin, M. Martini, F. Pupilli, and F. Terranova, "A new generation of neutrino cross section experiments: Challenges and opportunities," *Symmetry*, vol. 13, no. 9, 2021, ISSN: 2073-8994, DOI: 10.3390/sym13091625.

[103] T. Papaevangelou, "Développement d'un détecteur picosec-micromegas pour enubet–piment," 2022, [Online]. Available: https://anr.fr/Projet-ANR-21-CE31-0027.

[104] B. Abi, R. Acciarri, M. Acero, *et al.*, "The Single-Phase ProtoDUNE Technical Design Report. The Single-Phase ProtoDUNE Technical Design Report," Tech. Rep., 2017, 165 pages, fix references, author list and minor numbers, [Online]. Available: http://cds.cern.ch/record/2271524.

[105] N. Charitonidis, A. Longhin, M. Pari, E. G. Parozzi, and F. Terranova, "Design and diagnostics of high-precision accelerator neutrino beams," *Applied Sciences*, vol. 11, no. 4, 2021, ISSN: 2076-3417, DOI: 10.3390/app11041644.

[106] David Griffiths, *Introduction to Elementary Particles*. WILEY-VCH, 2008, Second Edition, ISBN: 978-3-527-40601-2, [Online]. Available: {https://www.wiley.com/en-es/Introduction+to+Elementary+Particles%2C+2nd%2C+Revised+Edition-p-9783527406012}.

[107] Greiner Reinhardt, *Quantum Electrodynamics*. Springer, 2009, Third Edition, ISBN: 978-3-540-87560-4, [Online]. Available: {https://link.springer.com/book/10.1007/978-3-540-87561-1}.

[108] E. Wilson and B. J. Holzer, "Beam dynamics," S. Myers and H. Schopper, Eds., pp. 15–50, 2020, DOI: 10.1007/978-3-030-34245-6_2.

[109] J. E. Sobczyk, "Nuclear effects in neutrino-nucleus interactions: The role of spectral functions," 2019, Doctoral Thesis - Universitat de València, [Online]. Available: https://ific.uv.es/nucth/Asia_tesis.pdf.

[110] J. Nowak, "Review of current neutrino simulation efforts genie, neut, nuwro," 2017, Lancaster University - IPPP/NuSTEC topical meeting on Neutrino-Nucleus scattering, [Online]. Available: https://conference.ippp.dur.ac.uk/event/583/contributions/3309/attachments/2809/3058/SimulationsEffortsNueStecIPPP_Nowak.pdf.

[111] [Online]. Available: https://nuwro.github.io/user-guide/.

[112] [Online]. Available: https://github.com/AchillesGen/Achilles.

[113] [Online]. Available: https://gibuu.hepforge.org/trac/wiki.

[114] [Online]. Available: https://t2k-experiment.org/results/.